Optofluidic Sensing with Optical Microresonators

by

Mustafa Eryürek

A Dissertation Submitted to the
Graduate School of Sciences and Engineering
in Partial Fulfillment of the Requirements for
the Degree of

Doctor of Philosophy

in

Physics

February 27, 2018

Optofluidic Sensing with Optical Microresonators

Koç University

Graduate School of Sciences and Engineering

This is to certify that I have examined this copy of a doctoral dissertation by

Mustafa Eryürek

and have found that it is complete and satisfactory in all respects,
and that any and all revisions required by the final
examining committee have been made.

Committee Members:

Prof. Dr. Alper Kiraz

Prof. Dr. Ali Serpengüzel

Prof. Dr. Zafer Ziya Öztürk

Prof. Dr. İskender Yılgör

Assist. Prof. Dr. Kenan Çiçek

Date: _____

To my dear wife, Selcan.

ABSTRACT

In this thesis, detection of various fluids using optical microresonators is described. As optical microresonators, different geometries are used such as microdisks, microrings, microspheres, and microcylinders. The sensing mechanism relies on the change of optical properties, when there is a change in the amount of a quantity of interest. Modes of the optical microresonators, also known as the whispering gallery modes (WGMs), are analyzed for the changes, and their spectral positions or quality factors are tracked, and employed as sensitive indicators of the changes. Sensing of air humidity and hydrogen gas, liquid refractometry, and contamination detection in liquid microspheres are demonstrated in the context of this thesis.

In humidity sensing work, air humidity is sensitively detected using SU-8 polymer microdisk resonators. These resonators are produced with a single-step fabrication, and they provide a repeatable and long-term-stable sensing platform. When these SU-8 microresonators are coated with Pd, they can also operate as hydrogen gas sensors. Using this idea, hydrogen gas sensing using Pd-coated SU-8 microdisk resonators is presented in the hydrogen concentrations well below its flammable limit of 4%.

Apart from gas sensing, detection in a liquid environment is also studied in two studies. In the first study, the refractive index of the liquid environment is detected using optical fiber resonators (OFRs). These OFRs are easily fabricated from standard optical fibers, and they provide refractive index sensitivity in the order of 10^{-5} RIU. Refractive index detection results, as well as the analytical calculations of the expected response of OFR sensors, are discussed. In the second study, contamination of the oil droplets is investigated for sunflower seed oil-olive oil mixtures. In addition, benzyl benzoate (BB) droplets are investigated. WGM shifts due to dissolution of the BB droplets, as well as incoming and outgoing small particles are discussed. The

experiments performed in microfluidic chips and the droplets are held in position using optical trapping. Based on the Q-factors of the droplets, the material contained inside the droplets can be predicted.

Finally, hydrogen gas sensing using polymer and Pd-coated OFRs is presented. These OFRs present even higher sensitivity than the Pd-coated SU-8 microdisk resonators. OFR sensors are easier to prepare and more flexible than the SU-8 microdisk sensors. Hydrogen concentrations down to 1000 *ppm* are successfully detected, with a potential detection limit less than 100 *ppm*. For all the sensing applications, detection results and underlying sensing mechanisms are presented, and they are compared with the state-of-the-art WGM-based sensors.

ÖZETÇE

Bu tezde sıvı ya da gaz evrede algılama yapabilmek için kullanılan optik mikroçınlaçlar işlenmiştir. Optik mikroçınlaç olarak mikrodiskler, mikrohalkalar, mikroyuvarlar ve mikrosilindirler gibi değişik geometriler kullanılmıştır. Algılama yöntemi, ortamda ölçülmek istenen bir niceliğin değişimi sonucunda değişen optik özelliklere dayanmaktadır. Bu nicelik değiştiği sırada mikroçınlaçların optik kipleri, diğer bir adıyla fısıldayan geçit kipleri (FGK'ler) incelenmiş ve elektromanyetik izge üzerindeki konumları ve nitelik katsayıları izlenmiş ve oluşan değişikliklerin duyarlı birer göstergeleri olarak kullanılmıştır. Bu tez kapsamında, havadaki nem ve hidrojen gazı algılaması yapılmış, sıvı kırılma katsayısı ölçülmüş ve sıvı mikroyuvarların içerisinde yabancı madde olup olmadığı denetlenmiştir.

Nem ölçümü çalışmasında, SU-8 mikrodisk çınlaçlar kullanılarak havadaki nemin algılanması gerçekleştirilmiştir. Kullanılan bu SU-8 mikrodisk çınlaçlar tek adımlı bir üretim ile elde edilmiştir, ve yinelenebilir, uzun süreli çalışan bir algılama olanağı sunmaktadır. Bu SU-8 mikrodisk çınlaçlar Pd ile kaplandığı zaman hidrojen gaz algılayıcısı olarak da kullanılabilmektedir. Bu düşünceden yola çıkarak, üzerine Pd kaplanmış SU-8 mikrodisk çınlaçlar ile düşük derişimlerde (hidrojenin yanma derişimi olan %4'ten çok daha düşük düzeylerde) hidrojen gazı algılaması gösterilmiştir.

Gaz örneklerden ayrı olarak, sıvı örneklerin kullanıldığı iki tane çalışma daha yapılmıştır. İlk çalışmada optik lif çınlaç (OLÇ) kullanılarak sıvı ortamın kırılma katsayısı ölçülmüştür. Bu çınlaçlar olağan optik liflerden kolaylıkla elde edilmekte ve 10^{-5}'lik kırılma katsayısı duyarlılığı göstermektedir. OLÇ algılayıcıdan beklenen tepki bulunmuş ve kırılma katsayısı algılaması deneysel sonuçları ile birlikte ortaya konmuştur. İkinci çalışmada ise yağdan elde edilen mikro-damlacıkların içerisindeki yabancı özdek algılaması deneyleri yapılmıştır. Bu çalışmaya ek olarak, benzil ben-

zoattan (BB) yapılmış damlacıklar incelenmiştir. BB damlacıkların çözünmesi ya da küçük boyutlu parçacıkların damlacıkla etkileşmesi sonucu FGK'lerinde meydana gelen değişimler açıklanmıştır. Bu deneyler, mikro-akışkan oluklar içeren yongalarda yapılmış ve damlacıklar optik cımbızlama yöntemiyle durgun tutulmuştur. Damlacıkların nitelik katsayıları izlenerek damlacık içerisinde yabancı özdek bulunup bulunmadığı anlaşılmaktadır.

Son olarak, polimer ve Pd kaplı OLÇ kullanılarak hidrojen gazı algılaması yapılmıştır. OLÇ'ler, Pd kaplı SU-8 mikrodisk çınlaçlardan daha duyarlı bir algılama ortaya koymuştur. Ayrıca OLÇ yapıları SU-8 mikrodisk yapılarından daha duyarlı olup üretilmeleri daha kolaydır. Bu çalışmada, milyonda 1000 gibi düşük derişimlerde hidrojen ölçümleri yapılmıştır, ve milyonda 100 düzeylerinin de altına inilebileceğinin olası olduğu tartışılmıştır. Elde edilen ölçümler ve bu ölçümlerin altında yatan algılama yöntemleri işlenmiş ve FGK tabanlı çalışmalarla ulaşılmış en iyi değerlerle karşılaştırma yapılmıştır.

ACKNOWLEDGMENTS

I would like to express my deepest gratitude to my advisor Professor Alper Kiraz for giving me the opportunity to work with him, his guidance, and the experiences I earned throughout my studies during the past six and a half years. I admire him for being always enthusiastic, and for his result-oriented approach towards solving problems.

I would like to thank Professors Ali Serpengüzel, İskender Yılgör, Zafer Ziya Öztürk, and Kenan Çiçek for joining my thesis committee. Specifically, I thank Prof. Serpengüzel for his help regarding the theory of whispering gallery modes and his expertise in droplet experiments. I thank Prof. Yılgör for his expertise and guidance in polymer science. I thank Prof. Öztürk for sharing his expertise in coating techniques, sensing methods, and his guidance regarding the problems about fiber coating. I thank Dr. Çiçek for his deep knowledge and endless help about the WGM theory and simulations, as well as his always joyful, mood which keeps me going enthusiastically.

I would like to express my gratitude to former and current members of Kiraz-lab who produce a productive research environment, discuss and suggest interesting ideas, and being good friends and helpful coworkers. Specifically Dr. Nevin Taşaltın, Dr. Mehdi Yavuz Yüce, Dr. Necati Vardar, Dr. Alexandr Jonáš, Dr. Mehdi Aas, Dr. Asuman Aşıkoğlu Bozkurt, Oğuz Kayıllıoğlu, Vahid Pour Reza Ghouschi, Baran Yalçın, Dr. Ahmet Can Erten, Dr. Suman Anand, Muhammad Waqas Nawaz, Ayşenur Eser, Adil Mustafa, Muhammad Zeeshan Rashid, Rana Muhammad Armaghan Ayaz, Nima Bavili, Ahmet Burak Gököz, Berk Zengin, Dr. Berna Morova, Ömer Yaman, Ateeq Ur Rehman, Gamze Gül, and Ahmet Aldemir. I would like to also thank Dr. Cihat Taşaltın, Dr. Selçuk Çakmak, Dr. Zuhal Taşdemir, Ümmü Koç, and Zafer Şen for their interest, help, and support in many different parts of my thesis.

I would like to express my appreciation to my friends Dr. İsmail Yorulmaz, Abdullah Muti, Abdullah Bilgin, Muhammad Haroon Qureshi, Syed Sultan Shah Bukhari for their constant and endless help and support, discussions related not only to research but also to life itself.

Last but not least, I would like to thank my beloved wife Selcan, to whom I dedicate this thesis. She is always supporting me, believing in me more than I do and giving me the enthusiasm, will and power to continue for more and the best.

This work was partially supported by the Scientific and Technological Research Council of Turkey (TÜBİTAK) under Grant Numbers of 110T803 and 115F446.

TABLE OF CONTENTS

LIST OF FIGURES

NOMENCLATURE

Symbols:

A_{klm}	Undetermined coefficients of Ψ
a	Radius of a microresonator
a_{eff}	Effective radius of an elliptical microresonator
B	Correlation length of surface roughnesses on a microresonator
C	Normalization constant
c	Speed of light in vacuum
c_{EG}	Ethylene glycol concentration
c_{ETH}	Ethanol concentration
c_{HYD}	Hydrogen gas concentration
d	Separation of parallel mirrors in a Fabry-Pérot resonator
$\mathbf{E}$	Electric field of light
g	Gravitational acceleration
$\mathbf{H}$	Magnetic field of light
h	Thickness of Pd layer on an OFR
k	Wavenumber of a photon
l	Polar mode number
M	Relatice refractive index
m	Azimuthal mode number
N	Refractive index of a material
n	Radial mode number
N_{eff}	Effective refractive index of a WGM
N_{in}	Refractive index inside a microresonator
N_{out}	Refractive index outside of a microresonator

O	Perimeter of an ellipse
p	Arbitrary azimuthal mode number
q	Arbitrary azimuthal mode number
R	Radial part of Ψ in spherical/cylindrical coordinates
r	Radial parameter in spherical coordinates
w	Hydrogen ratio inside palladium hydride
x	Size parameter outside the microresonator
y	Size parameter inside the microresonator
α	Absorption coefficient
γ	Angle of deviation from the perpendicular configuration
Δa	Change in the radius of a microresonator
ΔN	Change in the refractive index of a microresonator
ΔN_{out}	Change in the refractive index of the ambient environment
ΔQ	WGM Q-factor shift
$\Delta\lambda$	WGM resonance shift
$\Delta\lambda_{dehum}$	WGM resonance shift during dehumidification
$\Delta\lambda_{dehyd}$	WGM resonance shift during dehydrogenation
$\Delta\lambda_{hum}$	WGM resonance shift during humidification
$\Delta\lambda_{hyd}$	WGM resonance shift during hydrogenation
$\delta\lambda$	Full width at half maximum of a WGM resonance in terms of wavelength
$\delta\nu$	Full width at half maximum of a WGM resonance in terms of frequency
ζ	Riccati-Bessel function
η	Volume fraction of olive oil inside sunflower seed oil-olive oil mixture
Θ	Polar part of Ψ
θ	Polar angle in spherical coordinates
λ	Wavelength of a photon
λ_m	Resonance wavelength of azimuthal mode number m
ν	Frequency of a photon

ρ	Radial parameter in cylindrical coordinates
σ	Root mean square size of surface roughnesses on a microresonator
Φ	Azimuthal part of Ψ
ϕ	Azimuthal parameter in spherical/cylindrical coordinates
Ψ	Solution of Helmholtz equation
ψ	Riccati-Bessel function

Acronyms:

BB	Benzyl benzoate
CRDS	Cavity ring-down spectroscopy
DI	De-ionized
FDTD	Finite difference time domain
FSR	Free spectral range
HCF	Hollow-core fiber
HEC	Humidity expansion coefficient
Hys	Hysteresis
IPA	Isopropyl alcohol
IR	Infrared
LCORR	Liquid core optical ring resonator
LHC	Large Hadron Collider
MEEP	MIT Electromagnetic Equation Propagation
MKR	Microfiber knot resonator
NCF	No-core fiber
OFR	Optical fiber resonator
PDMS	Poly(dimethylsiloxane)
PEB	Post exposure bake
PMKR	Polymer microfiber knot resonator
PMMA	Poly(methyl methacrylate)

ppb	Parts per billion
ppm	Parts per million
RIU	Refractive index unit
RH	Relative humidity
SEM	Scanning electron microscope
SMF	Single mode fiber
SMKR	Silica microfiber knot resonator
TIR	Total internal reflection
THF	Tetrahydrofuran
TNT	Trinitrotoluene
TPP	Two-photon polymerization
WGM	Whispering gallery mode

Chapter 1

INTRODUCTION

The oldest known structure supporting whispering gallery modes (WGMs) is the garden of the temple of heaven in China, whereas the first description of WGMs has been published by Lord Rayleigh [Strutt, 1910]. In this study, he explains the solution to "The Problem of Whispering Gallery", which is observed not only in St. Paul's Cathedral in London as exemplified in his paper, but also in many others such as the Selimiye Mosque in Turkey, Masjed-e Imam in Iran, the U.S. Capitol Building, the Gol Gumbaz Mausoleum in India and the Whispering Arch in Germany. Whispering gallery problem involves two people standing next to the inner wall of the structure. Then the first person whispers near the inner wall, acting as a sound wave source. The second person is located tens of meters away from the first person, acting as a receiver. The receiver can detect the sound coming from the source, if he is close to the wall. This is a counter-intuitive result, since there is a huge distance between the source and the receiver for a whisper to be detected. The explanation is that, sound waves from the source experience successive total internal reflections (TIRs) at the inner boundary of the structure, so that they reach to the receiver without losing much of their intensity (see Figure 1.1). This idea is then transferred from acoustic regime to the optical regime by using optical microresonators [Foreman et al., 2015, Vahala, 2003, Benner et al., 1980].

Optical microresonators are employed in many applications [Ilchenko and Matsko, 2006] ranging from add-drop filters [Liou and Tseng, 2009, Gilardi et al., 2009] to lasers [He et al., 2013, Jiang et al., 2016, Michler et al., 2001]; nonlinear effects [Matsko et al., 2015, Serpengüzel et al., 1992] to sensors [Foreman et al., 2015]. This thesis focuses

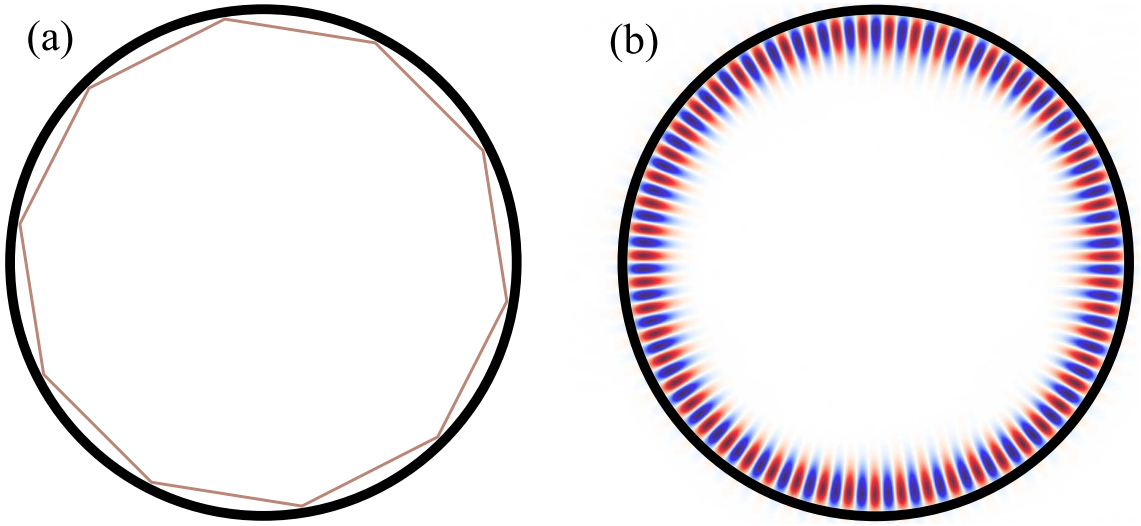

Figure 1.1: a) A sketch of an azimuthally symmetric resonator with light experiencing multiple TIRs in ray optics. b) MEEP (MIT Electromagnetic Equation Propagation) simulation indicating the waves propagating inside the resonator. Successive blue and red regions represent the peaks and dips in the electric field (**E**) of the WGM. Black circles represent the outer edge of the resonator.

on the use of optical microresonators in different geometries as sensitive detectors of various changes. Sensing is monitored either from the change in spectral positions of WGMs or the quality factor (Q-factor) of the microresonator. Sensing mechanism relying on the spectral shifts ($\Delta\lambda$) take advantage of environmental changes and subsequent spectral shifts of WGMs. In this thesis, $\Delta\lambda$-based sensing is demonstrated for applications such as air humidity, hydrogen concentration (gas-phase), ethanol or ethylene glycol (EG) concentration in water (liquid-phase). Although there are many other sensing applications with $\Delta\lambda$ [Foreman et al., 2015], Q-factor-based sensing is also employed for high-Q microresonators [Armani and Vahala, 2006, Vollmer et al., 2002]. In this thesis, the potential of contamination detection inside benzyl benzoate (BB) microsphere droplets optically trapped inside water host medium has been demonstrated using $\Delta\lambda$ [Anand et al., 2016]. These contaminants are small nanoparticles going in and out of the BB droplets during the experiment. In addition, depending on the volume fraction of olive oil inside sunflower seed oil-olive oil

mixture, Q-factor of these mixture droplets change. Since the Q-factor of sunflower seed oil droplets is less, sunflower seed oil is considered as a contaminant inside the olive oil droplet, and ΔQ-based detection is presented.

The arrangement of the thesis is as follows: In Chapter 1, WGMs are discussed, and a general introduction is given about the sensors utilizing optical microresonators. Their advantages have been explained, and state-of-the-art is discussed. Analytical solutions of the whispering gallery modes (WGMs) are described in Chapter 2. Then in Chapters 3 and 4, SU-8 microresonator-based sensing is demonstrated for air humidity and hydrogen gas detection, respectively. Liquid refractive index sensing with optical fiber resonators (OFRs) is presented in Chapter 5. Then in Chapter 6, spherical oil microdroplets optically trapped in water are investigated. In Chapter 7, hydrogen gas detection using PDMS-urea-based polymer and Pd-coated OFRs is presented. Finally, in Chapter 8, conclusions and outlook of the thesis are discussed.

1.1 Literature Review

Usage of optical microresonators possesses several properties to be used as sensors. Firstly, spectral positions and the Q-factors of WGMs of microresonators are very sensitive to geometrical parameters of the microresonator and parameters of the microresonator environment. Changes in the size of microresonators much less than λ [Eryürek et al., 2015], or refractive index changes as low as 10^{-7} [Hanumegowda et al., 2005, Li and Fan, 2010] can be detected and characterized from $\Delta\lambda$. Secondly, the small size of microresonators allows production of compact and quick-response sensors with sensitive detection. These microresonators have optical path lengths typically smaller than 1 mm, and response times below 1 s [Bhola et al., 2009]. State-of-the-art sensitivity is currently down to single virus [Dantham et al., 2012, He et al., 2011, Shao et al., 2013] or even single molecule level [Armani et al., 2007, Baaske et al., 2014, Li et al., 2014, Yoshue et al., 2011, Zhi et al., 2017]. Finally, WGMs can have very high Q-factors reaching up to 10^{10} in tiny volumes down to 3000 μm^3 [Vahala, 2003]. These properties allow enhanced interaction of light with the environ-

ment in a compact manner. Because of these reasons, there is a tremendous effort to employ optical microresonators in sensing applications [Foreman et al., 2015]. For instance, the temperature is a common quantity measured with optical microresonators [Dong et al., 2009, Li et al., 2010, Socorro et al., 2015]. During other sensing applications, temperature control has to be implemented to negate its effects [Bhola et al., 2009, Hanumegowda et al., 2005, Li and Fan, 2010, Ma et al., 2010, Wu et al., 2011]. In [Harker et al., 2013], UV detection based on the thermo-optic response of microtoroids is employed. In [Yebo et al., 2009], catalytic combustion of hydrogen and subsequent temperature increase is employed in optical microresonator hydrogen sensor.

Heavy water detection is another application that employs optical microresonator sensors [Armani and Vahala, 2006]. Rather than $\Delta\lambda$, the Q-factors of microtoroid resonators are monitored while the heavy water (D_2O) concentration in normal water (H_2O) is changed. Since the Q-factors of these microtoroids are $\sim 10^6$ in H_2O and $\sim 10^7$ in D_2O, sensitive detection of D_2O is presented down to 1 ppm using Q factor-based sensing. In the context of this thesis, similar Q-factor-based detection is employed for contamination detection in liquid optical microsphere resonators [Anand et al., 2016]. In this work, rather than a change in the environment, the material of the microresonator is changed, and subsequent Q-factor change is characterized.

Another microresonator-based sensing application is strain sensor employing SU-8 microring resonators [Bhola et al., 2005]. Two effects, optical path length change, and strain-optic effect are responsible for $\Delta\lambda$ observed when strain is applied to the UV15-7 layer where SU-8 microring is embedded. A similar idea is applied to silica, and PMMA microspheres and their force sensing capabilities are investigated [Ioppolo et al., 2008]. Because of their higher elasticity, PMMA spheres provide more sensitivity corresponding to a detection limit of $\sim 10\ \mu N$.

Accelerometer based on microresonator is also presented [Wu et al., 2009]. A microfiber knot resonator (MKR) is employed as an accelerometer for detection of vibrations with reported dynamic range and sensitivity values of $20g$ and 29 pm/g,

respectively.

Detection of gas species using WGM-based sensors is another frequently investigated topic. In the context of this thesis, sensing of air humidity [Eryürek et al., 2017b] and hydrogen gas [Eryürek et al., 2015] with optical microresonators have been presented. These results, as well as detailed literature review about humidity and hydrogen detection, can be found in Chapters 3 and 4. Other gas sensing applications involve ethanol, isopropyl alcohol (IPA), acetone, ammonia and TNT (trinitrotoluene) detection. For ethanol sensing, ZnO nanoparticle-coated SOI microring resonator with a Q-factor of 15000 is employed [Yebo et al., 2010]. With the porous structure of ZnO, detection limit less than 100 ppm is presented. Sensing of a similar chemical, IPA, has been performed using silicon nitride down to 50 ppm level [Ksendzov et al., 2004]. Using self-assembled PMMA hemispheres, refractive index-based acetone sensing is presented with a detection sensitivity of 130 nm/RIU [Ta et al., 2013]. Selective detection of ammonia is demonstrated with aluminosilicate-coated SOI microrings [Yebo et al., 2012]. With the use of the active layer, ammonia is detected with the estimated detection limit of 5 ppm, whereas the sensor shows almost no response to CO_2. Gas sensing for biochemical applications is presented using a microdisk laser diode in the shape of a half circle [Kim et al., 2017]. Various gases can be detected with a detection limit down to 1 ppm or less. Finally, a very sensitive detection application which involves TNT using Si_3N_4 microring resonators is also presented [Orghici et al., 2010]. With the coating of a triphenylene-ketal-based receptor layer on the resonator, the detection sensitivity is reported to be 7.4 pm for 1 ppb TNT.

1.2 Critical Parameters of Optical Microresonators

Optical resonators are characterized by their free spectral range (FSR) and quality factor (Q-factor). FSR is defined as the spectral distance between two consecutive azimuthal modes with the same polarization and radial mode number. FSR depends on the optical path length of the WGM, which depends on the size of the resonator

or refractive index of the resonator and the environment.

For a Fabry-Pérot resonator with a parallel mirror spacing of d, if oblique incidence is assumed, FSR is given as follows:

$$FSR = \lambda^2/2dN_{eff} \tag{1.1}$$

Analogously, for a cylindrical resonator, FSR is given by [Kavungal et al., 2018]

$$FSR = \lambda^2/2\pi aN_{eff} \tag{1.2}$$

where N_{eff} is the effective refractive index of the WGM.

For a spherical microresonator having refractive index of N_{in} and residing in an environment of refractive index N_{out}, FSR is given by [Chýlek et al., 1978]:

$$FSR = \frac{\lambda^2}{2\pi aN_{out}} \frac{tan^{-1}\sqrt{(N_{in}/N_{out})^2 - 1}}{\sqrt{(N_{in}/N_{out})^2 - 1}} \tag{1.3}$$

The first term $\frac{\lambda^2}{2\pi aN_{out}}$ is analogous to the FSR of a Fabry-Pérot resonator. The remaining second term is 1 if the relative refractive index $M = \frac{N_{in}}{N_{out}} = 1$. Then as M tends to infinity, it decreases monotonically and approaches to zero asymptotically. For practical applications, the second term is typically between 0.5 and 1.

Q-factor is defined as $\lambda/\delta\lambda$ where $\delta\lambda$ is the full width at half maximum (FWHM) of the WGM resonance, and λ is the WGM resonance wavelength. Overall Q-factor of a microresonator depends on individual Q-factors, which can be stated as follows:

$$Q^{-1} = Q_{mat}^{-1} + Q_{ss}^{-1} + Q_{rad}^{-1} \tag{1.4}$$

where

$$Q_{mat} = \frac{2\pi N_{in}}{\alpha\lambda}$$

is the Q-factor limited by the absorption of the material,

$$Q_{ss} = \frac{a\lambda^2}{\pi^2\sigma^2 B N_{out}^2}$$

is the Q-factor limited by the surface scattering [Righini et al., 2011] and,

$$Q_{rad} = xe^{2(l+\frac{1}{2})\left[cosh^{-1}(\frac{l+\frac{1}{2}}{x})-\sqrt{1-\frac{x^2}{(l+\frac{1}{2})^2}}\right]}$$

is the Q-factor limited by the radiation of WGMs out of the microresonator. Here α is the absorption coefficient, σ and B are the root mean square size and the correlation length of surface roughnesses. Also, $l \approx y = Mx$ where l is the polar mode number and $x = \frac{2\pi a N_{out}}{\lambda}$ is the size parameter.

Having high Q-factors is often desired since high-Q is an indication of good fabrication precision. Also, high-Q resonators provide very high sensitivities since they define sharp spectral positions. Since the overall Q-factor, Q, is given as in Eq. 1.4, Q is mainly determined by the smallest Q-factor. To have high Q_{mat} for instance, excitation wavelength and the material of the microresonator, as well as the environment, must be chosen such that α is small. For achieving high Q_{ss}, the surface roughness, i.e., B and σ of the microresonator must be decreased. Q_{rad}, although not immediately seen from its formula, is increased as the bending radius of the microresonator is decreased, or the relatice refractive index between the microresonator and the environment is increased. The dominant factor in Q_{rad} formula is the exponent. Since terms in the square brackets are ~ 1 for typical values of M, dominant term is $l + \frac{1}{2}$, which is $\approx y$. Hence, as a or M increases, Q_{rad} increases exponentially.

1.3 Sensing Techniques Used in this Thesis

Optical microresonator-based sensing applications in this thesis rely on the spectral shifts of WGMs of the resonator ($\Delta\lambda$) or Q-factor change (ΔQ) upon a certain disturbance in the properties of the surrounding environment or the microresonator.

$\Delta\lambda$ can occur because of two different reasons: Either refractive index of the medium of WGM changes (ΔN), or the size of the resonator changes (Δa). Therefore $\Delta\lambda$ can be formulated as follows: [Bhola et al., 2005, Bhola et al., 2009, Manzo et al., 2007, Mehrabani et al., 2013, Zhang et al., 2014]

$$\frac{\Delta\lambda}{\lambda} = \frac{\Delta a}{a} + \frac{\Delta N}{N}$$

Depending on the specific case in point, Δa and ΔN can be in the same order of magnitude or one can dominate the other. In the former case, Δa and ΔN may be causing $\Delta\lambda$ in the same [Mehrabani et al., 2013] or opposite [Ma et al., 2010] direction. In the latter case, either Δa or ΔN can be dominant. Due to mechanical stress induced on the microresonator by a disturbance in the environment results in a dominant Δa. This stress can be achieved directly on the microresonator or using another active layer. Polymer-coated microtubular resonators under humidity is an example of the former [Zhang et al., 2014], and palladium-coated SU-8 microdisk resonators under hydrogen gas is an example of the latter [Eryürek et al., 2015]. Achieving dominant ΔN can happen in two different ways: Change in the refractive index of the microresonator or the environment. An example of the former is humidity sensing with SU-8 optical microresonators. Air humidity makes hydrogen bonds with the oxygen inside SU-8 microresonator, increasing N_{eff} [Eryürek et al., 2017b]. Liquid refractive index sensing using optical fiber resonator, on the other hand, can be given as an example to the latter [Eryürek et al., 2017a]. Here, sensing is achieved through the evanescent tail of the WGM extending from the resonator into the environment. As a result, the effective refractive index (N_{eff}) of the WGM changes. For all the sensing applications in the context of this thesis, contributions of Δa and ΔN to $\Delta\lambda$ are considered, dominant effects are investigated, and presented in the corresponding chapters.

Another sensing technique used in the thesis is Q-factor-based sensing. Q-factor is a measure of the spectral sharpness of the WGM, and it depends on many parameters such as surface roughness of the microresonator, the material of the microresonator

and the environment, and the bending radius of the microresonator [Anand et al., 2016]. Q-factor can be measured from the transmission spectrum of the microresonator [Armani and Vahala, 2006] or through the lifetime measurement of the photon inside the microresonator, also known as the cavity ring-down spectroscopy (CRDS) [Arnold and Folan, 1989, Chen et al., 1993, Armani et al., 2003]. In the context of this thesis, contamination inside oil droplets held inside water host medium is determined by monitoring Q-factors of oil droplets.

Chapter 2

OPTICAL WHISPERING GALLERY MODES

For a wave Ψ, electromagnetic wave equation obtained from Maxwell's equations is given by

$$\nabla^2\Psi = \frac{\partial^2\Psi}{c^2\partial t^2}$$

Assuming oscillatory time dependence, it can be written as

$$\nabla^2\Psi + k^2\Psi = 0$$

where k is the wave number of the incoming light. This equation, also known as the Helmholtz equation, is the time-independent wave equation. Most of the time, microresonators are in the shape of a disk or a sphere. Therefore rigorous solutions to the Helmholtz equation in cylindrical and spherical coordinates will be discussed.

2.1 WGM Solutions for the Cylindrical Geometry

The Helmholtz equation in cylindrical coordinates is given by [Arfken and Weber, 2005]:

$$\frac{\partial^2\Psi}{\partial\rho^2} + \frac{1}{\rho}\frac{\partial\Psi}{\partial\rho} + \frac{1}{\rho^2}\frac{\partial^2\Psi}{\partial\phi^2} + \frac{\partial^2\Psi}{\partial z^2} + k^2 = 0$$

To apply the separation of variables technique, consider $\Psi = R(\rho)\Phi(\phi)Z(z)$. (If we are dealing with a microdisk resonator, then $Z(z)$ part of the solution should exist. On the other hand, if an infinitely-long cylinder is considered, then there is no $Z(z)$ part.)

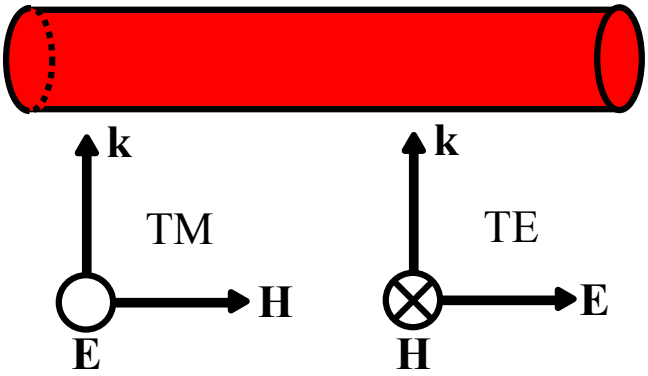

Figure 2.1: A sketch indicating the TM and TE polarizations in cylindrical coordinates. The definition of the polarization is based on the orientation of the electric field **E** with respect to the WGM plane. If **E** is in the same plane as the WGM, polarization is TM, whereas if they are perpendicular, then the polarization is TE.

The scattered field coefficients can be found from the boundary conditions [Bohren and Huffman, 1998, van de Hulst, 1981].

$$TM_m = \frac{J'_m(y)J_m(x) - MJ_m(y)J'_m(x)}{J'_m(y)H_m(x) - MJ_m(y)H'_m(x)} \tag{2.1}$$

$$TE_m = \frac{MJ'_m(y)J_m(x) - J_m(y)J'_m(x)}{MJ'_m(y)H_m(x) - J_m(y)H'_m(x)} \tag{2.2}$$

where J_m is the mth-order Bessel function of the first kind, H_m is the mth-order Hankel function of the first kind. TM_m and TE_m represent the field coefficients of WGMs with azimuthal mode number m, having TM and TE polarizations, respectively. The definition of TM and TE is given with respect to the mode plane. Therefore TM (TE) means magnetic field **H** (electric field **E**) is perpendicular to the mode plane (see Figure 2.1). The resonances occur, when the field coefficients blow up to infinity.

An exemplary calculation is depicted in Figure 2.2. Behaviors of the denominators in Equations 2.1 and 2.2 are plotted as a function of λ. To coincide with a WGM, these denominators must be at one of their minima (so that, the overall TM_m and TE_m coefficients reach their maxima). In the calculation, input parameters are chosen as follows: $N_{in} = 1.46$, $N_{out} = 1$, $m = 355$, $a = 62.5\ \mu m$ and $225 < x < 270$. As λ gets smaller and smaller, there are no WGMs up until $\lambda \approx 1.56\ \mu m$ ($n = 1$), whereas

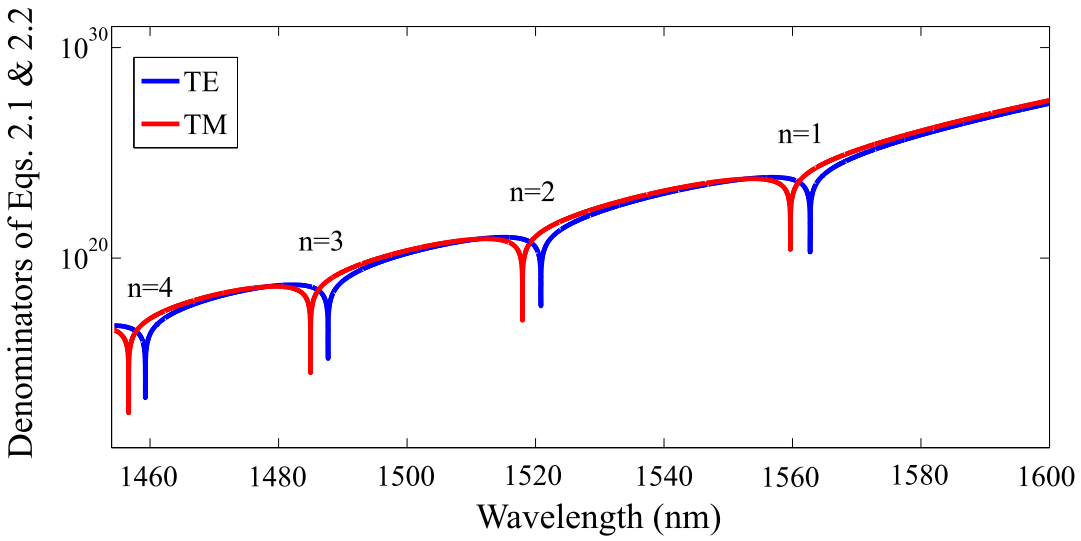

Figure 2.2: Calculation of spectral positions of WGMs for a cylindrical resonator. For TE and TM polarizations, WGMs are separately depicted. Each minimum represents a different WGM. The WGMs around 1.56 μm are the first-order radial modes, whereas the other WGMs with smaller λ are the higher-order radial modes. Parameters in the calculation are chosen for an OFR obtained from a standard optical fiber.

there are many WGMs afterwards ($n > 1$). Therefore $\lambda \approx 1.56\ \mu m$ is the cut-off wavelength. These multiple WGMs are higher-order radial modes, which have low Q-factors. Therefore in the calculations, only the first-order radial modes are taken into consideration. In Figure 2.2, spectral positions of TE and TM modes are calculated as 1.562743 μm and 1.559678 μm, respectively.

In order to calculate the FSR, only m is increased or decreased by 1, without changing the other parameters. For instance, if $m = 354$, the resonances occur at 1.567066 μm and 1.563985 μm respectively for TE and TM modes. Therefore FSR is calculated to be 4.323 nm and 4.307 nm for TE and TM modes, respectively.

Finite difference time domain (FDTD) simulations using MEEP program [MEEP, 2017, Lambert et al., 2011] on a 2D disk resonator reveals the behavior of the WGM profile in the azimuthal and radial directions [Eryürek, 2013] (see Figure 2.3). Oscillatory behavior is seen in the azimuthal direction, whereas in the radial direction

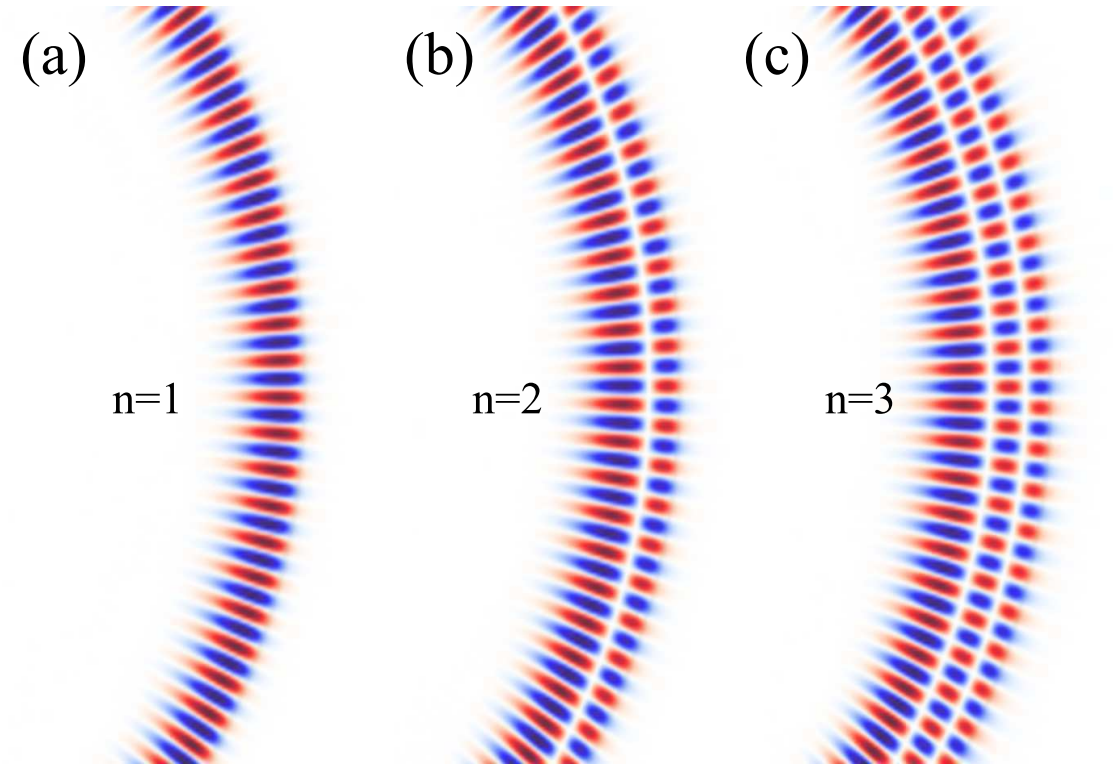

Figure 2.3: MEEP simulation results for a 2D disk. Parameters are kept constant and λ is adjusted such that a) first, b) second, and c) third-order radial modes are excited for $a = 20\ \mu m$ and $N = 1.5$ [Eryürek, 2013].

Bessel function behavior is observed. For generating these figures, simulation parameters are as follows: $a = 20\ \mu m$, $N_{in} = 1.5$, $N_{out} = 1$, and $\lambda \approx 1.55\ \mu m$. By keeping all the parameters constant and adjusting λ, $n = 1$, $n = 2$, and $n = 3$ radial modes are revealed and depicted in Figure 2.3-a, b, and c, respectively.

2.2 WGM Solutions for the Spherical Geometry

Helmholtz equation in spherical coordinates is given by [Arfken and Weber, 2005]:

$$\frac{1}{r^2}\frac{\partial}{\partial r}\left(r^2\frac{\partial \Psi}{\partial r}\right) + \frac{1}{r^2\sin\theta}\frac{\partial}{\partial \theta}\left(\sin\theta\frac{\partial \Psi}{\partial \theta}\right) + \frac{1}{r^2\sin^2\theta}\frac{\partial^2 \Psi}{\partial \phi^2} + k^2\Psi = 0$$

It is convenient to use the separation of variables method, i.e., Ψ can be written as the product of three functions; $\Psi = R(r)\Theta(\theta)\Phi(\phi)$. The ϕ-dependent term is

immediately solved to be oscillatory, i.e., $\Phi(\phi) = e^{im\phi}$ where m is the azimuthal mode number. After ϕ is eliminated; θ, and r can be separated and made to be equal to a constant as follows:

$$\frac{1}{R}\frac{d}{dr}\left(r^2\frac{dR}{dr}\right) + k^2r^2\frac{1}{\Theta\sin\theta}\frac{d}{d\theta}\left(\sin\theta\frac{d\Theta}{d\theta}\right) - \frac{m^2}{\sin^2\theta} = 0$$
$$\frac{1}{\Theta\sin\theta}\frac{d}{d\theta}\left(\sin\theta\frac{d\Theta}{d\theta}\right) - \frac{m^2}{\sin^2\theta} = l(l+1)$$

The reason for the use of constant $l(l+1)$ is to make a resemblance with the Associated Legendre equation, so that the solutions of the θ part immediately becomes Associated Legendre Polynomials. Here, the required substitution is $v = \cos\theta$. Then we have:

$$\frac{d}{dv}\left[(1-v^2)\frac{d\Theta(v)}{dv}\right] + \left[l(l+1) - \frac{m^2}{1-v^2}\right]\Theta(v) = 0$$

and the solutions are aforementioned Associated Legendre Polynomials, denoted by $\Theta(v) = P_l^m(v)$. They depend on both the azimuthal and the polar mode numbers m and l. When the angular parts Θ and Φ are multiplied together, the result is defined to be the spherical harmonics, denoted as $Y_l^m(\theta,\phi) = CP_l^m(\cos\theta)e^{im\phi}$, where C is a normalization constant.

The remaining radial part of the wave equation hence becomes

$$\frac{d}{dr}\left(r^2\frac{dR}{dr}\right) + [k^2r^2 - l(l+1)]R = 0$$

This is the Spherical Bessel Equation, whose solutions are spherical Bessel functions $j_m(kr)$. The argument of the spherical Bessel functions is dimensionless parameter kr. Therefore full solution becomes:

$$\Psi(r,\theta,\phi) = \sum_k \sum_{l=0}^{\infty} \sum_{m=-l}^{l} A_{klm} j_l(kr) Y_l^m(\theta,\phi)$$

where A_{klm} is a constant, which can be determined from the boundary conditions dictated by the geometry of the problem. For our case, the scattered fields and their

first derivatives are continuous at the resonator boundary, which results the following field coefficients for TM and TE modes, respectively:

$$TM_m = \frac{\psi'_m(y)\psi_m(x) - M\psi_m(y)\psi'_m(x)}{\psi'_m(y)\zeta_m(x) - M\psi_m(y)\zeta'_m(x)}$$
$$TE_m = \frac{M\psi'_m(y)\psi_m(x) - \psi_m(y)\psi'_m(x)}{M\psi'_m(y)\zeta_m(x) - \psi_m(y)\zeta'_m(x)}$$

where $M = N_{in}/N_{out}$ is the relative refractive index, $x = 2\pi a N_{out}/\lambda$ is the size parameter and $y = Mx$. $\psi_m(x) = xj_m(x)$ and $\zeta_m(x) = xh_m^{(2)}(x)$ are Riccati-Bessel functions, which are modified forms of spherical Bessel functions $j_m(x)$ and $h_m^{(2)}(x)$.

Chapter 3

HUMIDITY SENSOR BASED ON SU-8 MICRODISKS

3.1 Introduction

In this chapter, detection of air humidity using SU-8 microdisk resonators is described. Detection of air humidity is crucial in many applications [Kolpakov et al., 2014]. For instance, humidity control is important in domestic applications such as air conditioning, food preparation, and ovens [Chen and Lu, 2005, Lee and Lee, 2005]. In industry, it is required in textile processing, automotive, electronics, and pharmaceutical production [Lee and Lee, 2005, Tripathy et al., 2014]. Soil moisture control, greenhouse conditioning and environmental control are issues in agriculture that require humidity control [Chen and Lu, 2005, Tripathy et al., 2014]. In medicine, humidity control in respiratory equipment is crucial for preserving and improving the health of patients [Chen and Lu, 2005]. Museums require humidity control for the protection of delicate archaeological samples [Kolpakov et al., 2014]. In advanced research activities such as gas purification, photoresist production, clean room conditioning and silicon wafer processing require sensitive control of humidity [Bhola et al., 2009, Kolpakov et al., 2014, Lee and Lee, 2005]. All these applications necessitate properly calibrated, sensitive and quickly responding humidity sensors [Rittersma, 2002].

Although different humidity sensing techniques are employed [Farahani et al., 2014], optical detection of air humidity allows smaller and more flexible sensors, which are not influenced by the electromagnetic interference [Tripathy et al., 2014]. Moreover, instead of intensity-based measurements, spectroscopic measurements provide more robust sensors, since the intensity fluctuations of the light source are eliminated. Optical microresonators provide such a spectroscopic measurement tool, since their

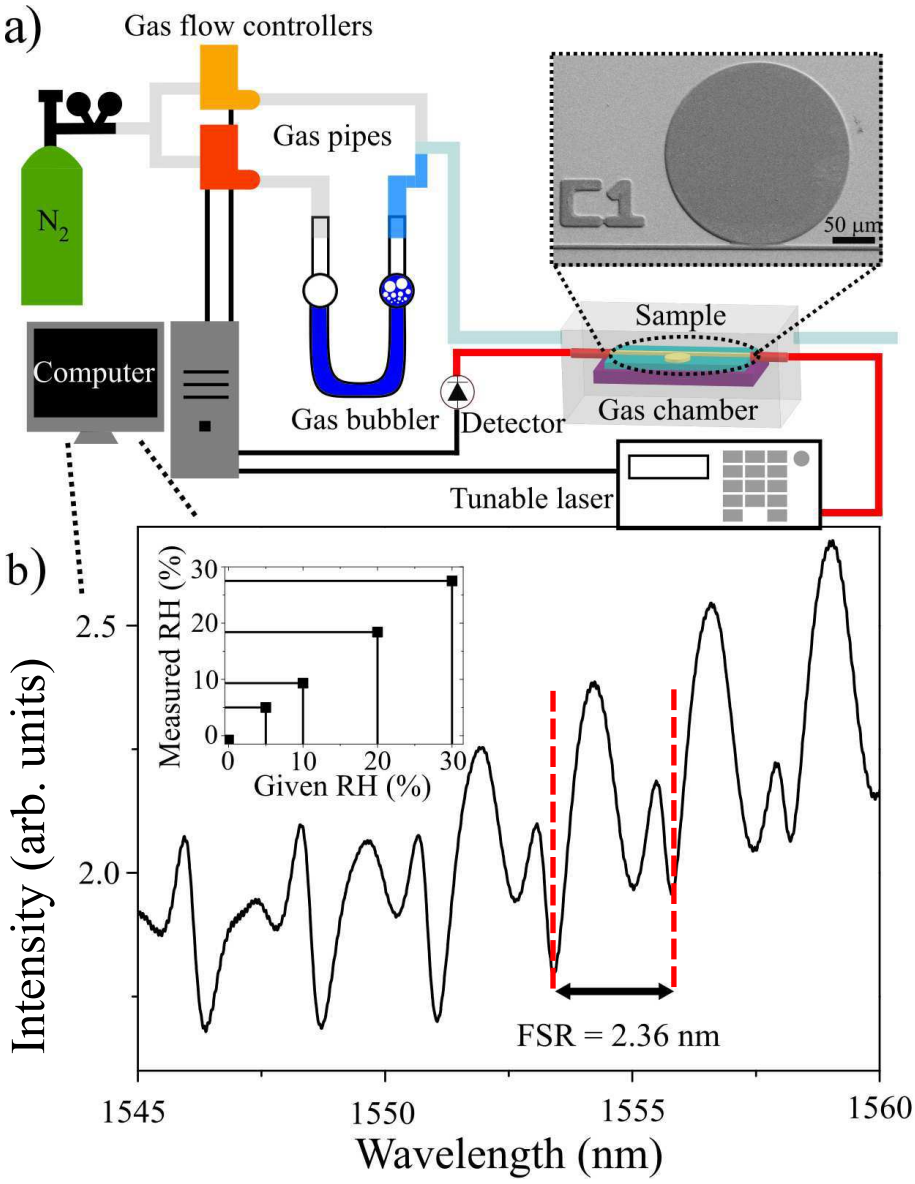

Figure 3.1: a) Experimental setup of humidity sensing measurements. N_2 gas is flown through two separate gas flow controllers. One is directly connected to the gas chamber whereas the other is connected to a bubbler filled with DI water. Using end-face coupling method, tunable laser light is coupled from optical fiber to SU-8 waveguide inside the gas chamber. In the inset, SEM image of the SU-8 humidity sensor is depicted. b) Transmission spectrum obtained from SU-8 microdisk resonator. FSR is measured to be 2.36 nm. The inset shows the comparison between the RH set by the flow controllers and RH measured from the commercial humidity sensor.

WGMs sensitively depend on the environmental parameters. Therefore, in many studies, optical microresonators are implemented in humidity sensing applications [Ma et al., 2010, Bhola et al., 2009, Mehrabani et al., 2013, Zhang et al., 2014, Wu et al., 2011].

In [Ma et al., 2010], humidity detection based on $\Delta\lambda$ of SiO_2 nanoparticle-coated silica microsphere resonator is presented. $\Delta\lambda$ is caused by adsorption of water vapor inside the SiO_2 nanocoating, and subsequent ΔN. Reported sensitivity is $\sim 4\ pm/\%\ RH$, where RH stands for the relative humidity. Since the interaction is due to the evanescent tail of the WGM extending into the nanocoating region, higher order radial modes extending more into the coating are expected to be more sensitive. This is investigated in the paper by comparing the sensitivities of first and fifth radial order modes. As expected, fifth order radial mode exhibits ~ 6 % higher sensitivity, since optical intensity fractions of first and fifth radial order modes in the nanocoating region are calculated as 0.358% and 0.379%, respectively (~ 6 % difference). However, the trade-off is that, WGMs with higher order radial mode numbers tend to have lower Q-factors.

In another study [Wu et al., 2011], humidity is detected using microfiber knot resonators (MKRs). Two different materials are employed for MKR; silica MKR (SMKR) and polymer MKR (PMKR). Sensing is based on ΔN, which is different for SMKR and PMKR. Respective sensitivities for SMKR and PMKR are reported as $\sim 1.2\ pm/\%\ RH$ and $\sim 8.8\ pm/\%\ RH$, which indicates the PMKR experiences higher ΔN than silica MKR. The advantage of these sensors is that, they have a very broad linearity range (17% to 95% RH for PMKR) with a very fast response of < 0.5 s.

Adding Δa effect to ΔN effect produces higher sensitivity, therefore a hybrid humidity sensor is presented [Mehrabani et al., 2013]. In this work, a silica microtoroid resonator is coated with a polymer (poly(N-isopropylacrylamide)), which experiences a conformational change together with refractive index change in the presence of humidity. Two different coating thicknesses of 38.5 nm and 71.5 nm are employed,

and their sensitivities are $\sim 13.0\ pm/\%\ RH$ and $\sim 10.4\ pm/\%\ RH$, respectively. This is ~ 40 times improvement on the sensitivity of the uncoated microtoroid. Advantages provided by this work are high Q-factors of polymer-coated microtoroids reaching up to 2.5×10^5 and response times below 1 s. Response and recovery of microtoroids with the thinner coating are quicker than the thicker coating. This is attributed to easier access and removal of humidity in and out of the polymer coating.

There is another study employing microresonators for humidity sensing [Bhola et al., 2009]. In this work, sol-gel-coated SU-8 microring resonator is used. Similar to other ΔN-dominated studies, the refractive index of the sol-gel coating increases with humidity. As the sol-gel thickness is increased from 200 nm to 3 μm, the sensitivity increases, and the response time decreases. The advantage of the sol-gel coated SU-8 microring resonator is that, the reported sensitivity is higher than the previous studies (16 $pm/\%\ RH$), and the sensor shows almost no hysteresis.

A Δa-based humidity sensing is performed using Rhodamine-B-doped PEG-DA hydrogel microdisk resonator [Huang et al., 2017]. The hydrogel stretches in the presence of humidity. As a result, WGM resonances shift with a linear response of 43 $pm/\%\ RH$ in the range of 25% to 65% RH. Lasing is achieved due to the presence of Rhodamine, and WGMs are observed in the lasing spectra.

The most humidity-sensitive optical microresonator is roll-up polymer/oxide/polymer-based sensor [Zhang et al., 2014], reporting a sensitivity of 130 $pm/\%\ RH$. The microresonator involves several metal oxide layers sandwiched between polymers (specifically poly(acrylic acid) and poly(ethylenimine)). Unlike the other microresonator-based studies, the dominant effect for the humidity sensing is Δa caused by the expansion of the polymer layers, when humidity is introduced. Depending on the polarization of the WGM, humidity sensitivity changes by a factor of 2. This is attributed to different confinement factors of WGMs with different polarizations. Because of the same confinement reason, it is observed that WGMs having smaller azimuthal mode numbers tend to have higher sensitivity [Zhang et al., 2014].

As discussed above, polymers are frequently employed for humidity sensing ap-

plications, especially because of their porous structures and compatible nature with the air humidity. Among these polymers, SU-8 has excellent mechanical and optical properties, in which the most important one regarding optical microresonator sensors is having a higher refractive index than SiO_2 (around 1550 nm 1.573 and 1.443, respectively) [Eryürek, 2013]. Therefore, in this chapter, SU-8 microdisks on the SiO_2 substrate are employed as humidity sensors. In [Bhola et al., 2009], SU-8 microrings are employed for humidity sensing. However, a sol-gel coating is also required. Using SU-8 microdisks instead of microrings eliminates the requirement of additional coating because SU-8 itself is a polymer and responds to humidity quite well. Also, results with SU-8 microdisks provide much higher sensitivity as discussed below [Eryürek et al., 2017b]. Fabrication parameters, sensing mechanism, and experimental details, as well as the results, are also discussed.

3.2 Fabrication of SU-8 Microdisk Resonators

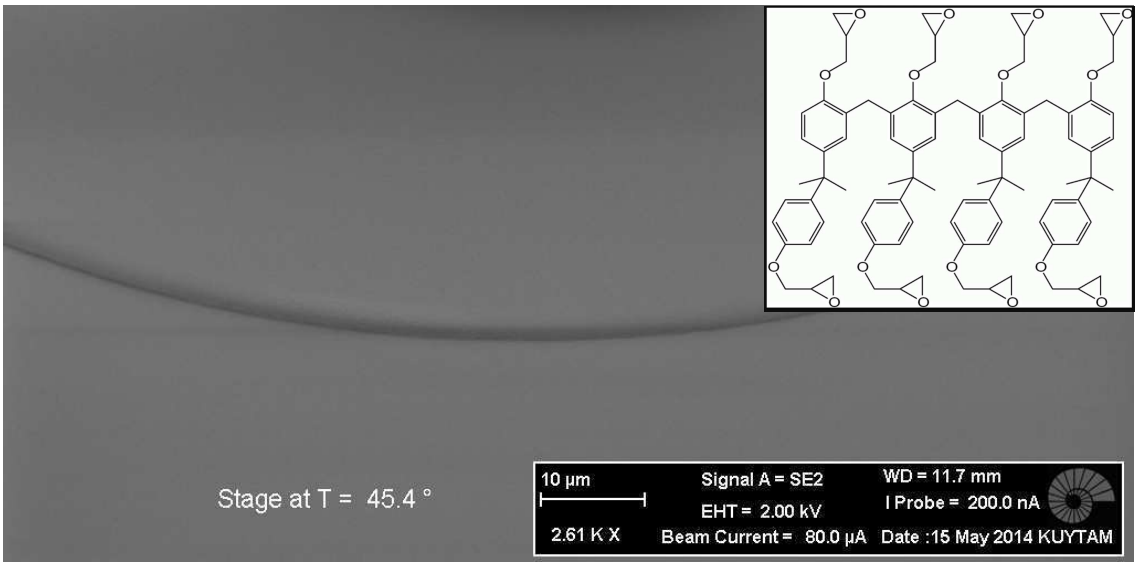

Figure 3.2: SEM image of an edge of an SU-8 microdisk resonator. The measurement reveals an SU-8 thickness of 1.86 μm. The monomer of the SU-8 is depicted in the inset.

SEM of the designed structure is given in the inset of Figure 3.1-a. SU-8 mi-

crodisks and waveguides are fabricated on thick-oxide Si wafers using standard UV photolithography. Standard Si wafers are not applicable, because of Si having a higher refractive index than SU-8. Therefore a 5 μm-thick thermally grown oxide layer is used as the substrate. Fabrication steps involve spin coating of commercially available SU-8 2002 dissolved in cyclopentanone solvent [MicroChem, 2018]. Monomer of SU-8 is depicted in the inset of Figure 3.2. Then soft bake, UV exposure, post exposure bake (PEB), and wet etching (development) are performed. Recipe for the spin coating has two steps; in the first step, spin speed is 500 rpm for 10 s, and in the second step, spin speed is 3000 rpm for 60 s. This recipe provides 1.5 to 2 μm thickness of SU-8 (see Figure 3.2). Then the wafers are soft-baked for 1 min at 95°C. The exposure dose is not measured because over-exposure of SU-8 is not a problem, since SU-8 is a negative-tone photoresist. After sufficient exposure, PEB is applied for 2 min at 95°C. PEB step is not present in the fabrication flow of every photoresist. However, it is a necessary step for SU-8 fabrication flow. Finally, after PEB, wafers are developed, rinsed with IPA and DI water and dried with N_2.

After the fabrication, all microdisks have outer diameters of 200 μm. The widths of the waveguides are either 2 or 3 μm. Since end-face coupling [Bellini et al., 2007, Lv et al., 2015] technique is used to couple light from an optical fiber to the SU-8 waveguide, wafers are cut along the brittle crystal planes determined by the crystal orientation of the wafer. Obtained smaller wafer portions (chips) are used in the gas chamber for sensing experiments (see Figure 3.1-a). Although end-face coupling is not the most efficient method to couple the light in and out of the fiber [Cai et al., 2000, Spillane et al., 2003], more than enough light is collected from the transmission spectra of the microdisks (see Figure 3.1-b). In the obtained transmission spectra, the free spectral range (FSR) of the microdisk is 2.36 nm, as compared to reported FSR of 2.28 nm belonging to a similar device from the literature [Cho and Jokerst, 2006] and theoretical value of 2.45 nm. The small deviation between these values may be because of different polarizations having different FSR values.

Another method to fabricate SU-8 microdisks is two-photon polymerization (TPP)

technique [Horváth et al., 2017]. For exposure of SU-8, instead of using UV light, two-photon absorption of red light can be employed. For two-photon absorption to be successful, red photons must be confined in both space and time. Space confinement can be achieved by focusing the photons with an oil-immersion objective, whereas time confinement is achieved using femtosecond pulses from a fiber laser with wavelength 785 nm (see Figure 3.3). This means photons of wavelength 392.5 nm are obtained. SU-8 is most sensitive to UV around 365 nm, but 392.5 nm is also acceptable. Since oil immersion objective and inverted microscope are used, Si wafers cannot be taken as substrate. Rather, thin microscope cover glasses are used as substrates.

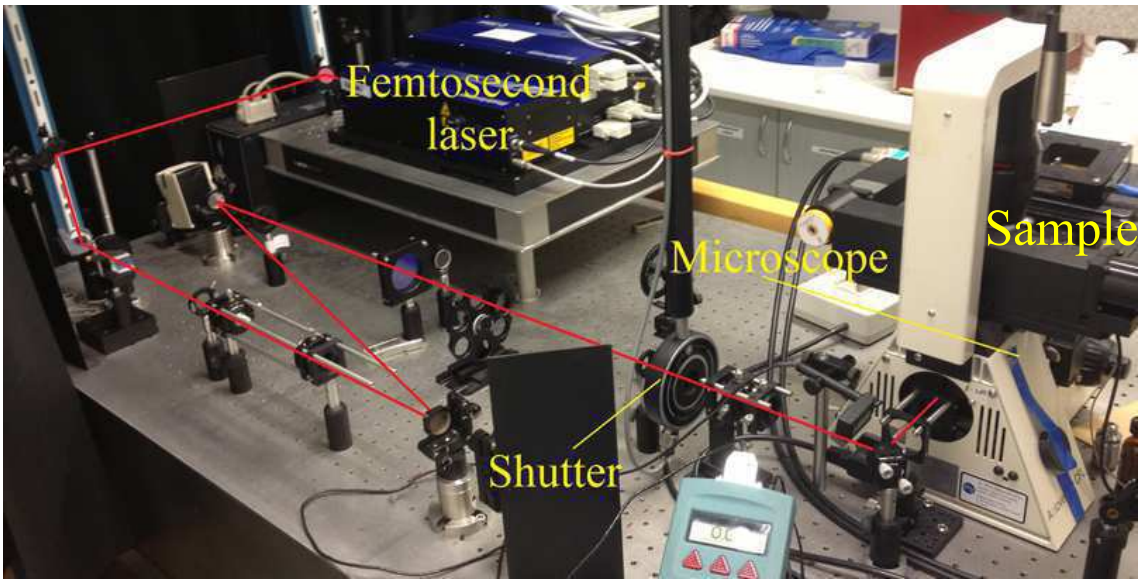

Figure 3.3: Photograph of the TPP setup. Femtosecond laser pulses, whose path is indicated as red are directed into an inverted microscope through a shutter. Then these pulses are focused by an oil-immersion objective. Using a piezo stage, the sample in 3 dimensions for the writing process. The sample is located on the objective during the writing.

With TPP technique, SU-8 exposure occurs only inside focal volume, also known as the voxel, where the intensity is high enough. Therefore, the voxel presents a very sharp boundary between exposed and unexposed regions of the SU-8, allowing fabrication of very smooth surfaces with small feature sizes (see Figure 3.4). Using

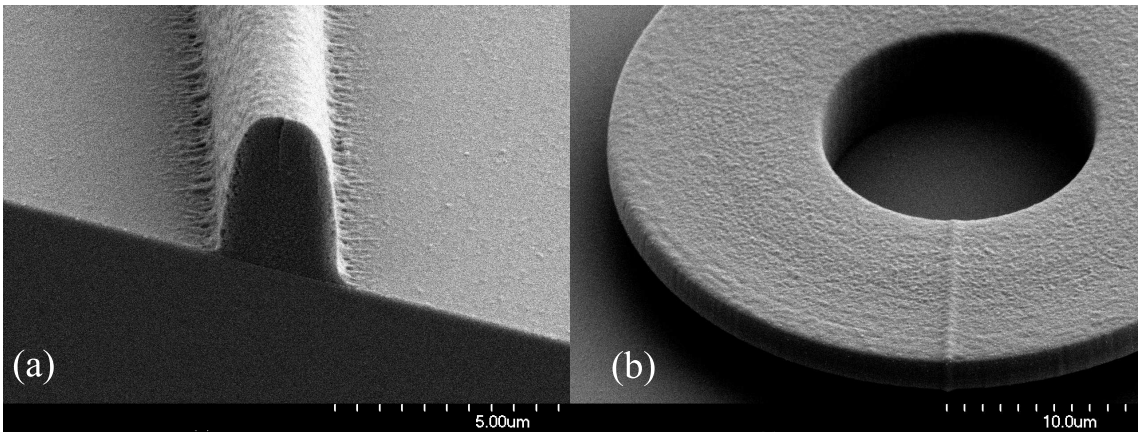

Figure 3.4: a) End-face cross section of a waveguide fabricated using UV laser writing. b) An SU-8 microring fabricated using TPP. A line along the radial direction is observed, because writing starts and ends at these points, resulting slightly higher exposure times along the line.

a piezo stage for sample translation does not allow to write structures larger than $80 \times 80\ \mu m^2$. Therefore the excitation waveguides are not fabricated with TPP, but with UV laser writing. The writing speeds and the powers of the red and UV lasers are optimized to have a robust polymerization without burning the SU-8 layer. For TPP, the best structures are obtained for writing speed 24 $\mu m/s$ and red laser average power 7 mW. For waveguide fabrication, writing speeds ranging from 0.2 to 5.0 mm/s, with UV laser powers ranging from 30 to 120 mW are found to be optimum parameters.

3.3 Sensing Mechanism

The sensing mechanism relies on the WGM resonance shifts of the SU-8 microdisks caused by the adsorption of air humidity on the SU-8 microdisk. Water makes hydrogen bonds with the oxygen in the SU-8, which results in an increase in the refractive index of the microdisk resonator. This increase is measured through the red-shift between the consecutive transmission spectra of the microdisk. To verify that the ΔN effect is dominant over the Δa effect, finite element method (FEM) simulations

have been performed [Eryürek et al., 2017b]. It is known that humidity expansion coefficient (HEC) of SU-8 is 25.3 $ppm/\%\ RH$ [Schmid et al., 2009]. This value is introduced into the FEM simulation, and unrestrained SU-8 microdisk is simulated (see Figure 3.5-a), and compared with the analytical formula of $\Delta a = a\ HEC$ to verify that, the simulation is running correctly. From both the simulation and the analytical formula, $\Delta a = 2.53\ nm$ is obtained. With the confirmation of simulation, another simulation is run, where the SU-8 microdisk is fixed on a rigid substrate (see Figure 3.5-b). This simulation is a good depiction of SU-8 microdisk fabricated on a thick-oxide Si wafer, since the wafer does not expand, when the humidity is changed. $\Delta\lambda/\lambda$ based only on the effect of Δa is calculated to be 6×10^{-7}. As compared to $\Delta\lambda/\lambda = 7 \times 10^{-5}$ measured experimentally, it is negligible. Therefore in SU-8 microdisk resonator humidity sensor, the dominant effect is $\Delta N/N$.

Average sensitivity obtained from the measurements is 108 $pm/\%\ RH$, which is better than previously reported microresonator-based humidity sensors except for [Zhang et al., 2014] (average sensitivity: 130 $pm/\%\ RH$). The advantage of SU-8 microdisk resonator sensor is, without losing from the sensitivity, single-step fabrication is sufficient rather than requiring multiple layers and fabrication steps. Also, the FEM simulation allows the distinction between ΔN and Δa effects.

3.4 Humidity Sensing Measurements

Humidity sensing is achieved through the red-shift in the transmission spectra of the SU-8 microdisk. Transmission spectra are obtained using tunable laser light (Santec TSL-510-C, tunability range: 1500 nm - 1630 nm, wavelength resolution: 1 pm) coupled from a single mode optical fiber to SU-8 waveguide via the end-face coupling. It is crucial to have a smooth and straight cross section for both the single mode fiber and the SU-8 waveguide, so that enough coupling is achieved. It is possible to obtain straight-cut optical fibers after the fiber is scratched by a diamond cutter, because of built-in internal stress in the fiber. To obtain straight cross sections for the SU-8 waveguides, they are fabricated along the perpendicular direction to the crystal

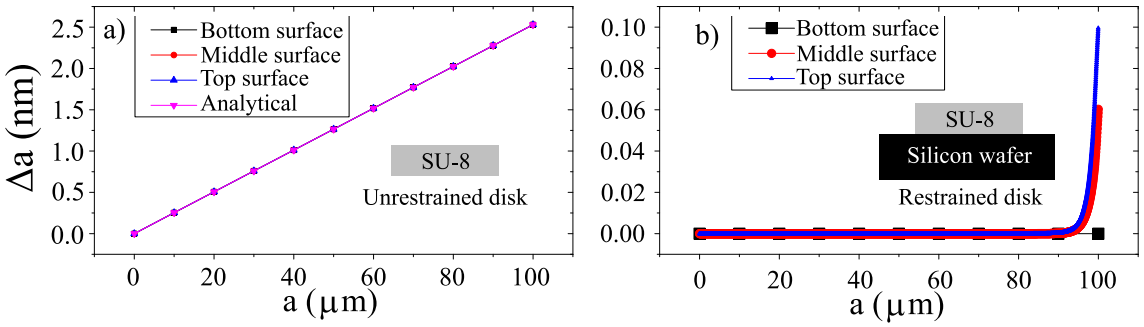

Figure 3.5: Humidity expansion simulations of a) unrestrained SU-8 microdisk and b) SU-8 microdisk fixed on a rigid substrate. Unrestrained case matches well with the analytical formula whereas the fixed case has expansion only around the edges of the microdisk. The bottom surface of the microdisk is not expanded, since it is fixed on the rigid substrate. However, the middle and the top parts of the microdisk expand by a smaller amount than the unrestrained case. Expansion at the middle part is taken to be the effective expansion "felt" by the WGM. Indicators of bottom, middle and top surfaces are chosen to be in different sizes for better visualization because they overlap over the region, where 0 $\mu m < a < 90$ μm

orientation (see Figure 3.6). This allows nice and straight waveguide cross sections, when the wafers are cut along their brittle crystal orientations.

The wavelength of operation is chosen to be in the telecom wavelength regime instead of visible wavelengths. This allows having 2-3 μm waveguides for successful coupling from the waveguide to the microdisk. Otherwise, if visible light is used, much thinner SU-8 waveguides would be required, since 2-3 μm waveguides would be too thick to couple the visible light out of the waveguide to the microdisk. Therefore, using visible light necessitates sub-micron-thick SU-8 waveguide, which is a fabrication challenge for standard UV photolithography.

The tunable laser light coupled into the SU-8 waveguide is collected from the other side of the waveguide. While recording the intensity, the wavelength of the laser is tuned in a certain range with a certain speed. For the humidity sensing experiments, 10-20 nm scanning range with a scanning speed of 1-2 nm/s is applied. Intensity is recorded in a synchronized manner with the wavelength sweep of the laser. Therefore the wavelength of the laser is known at each point in time. Then consecutive

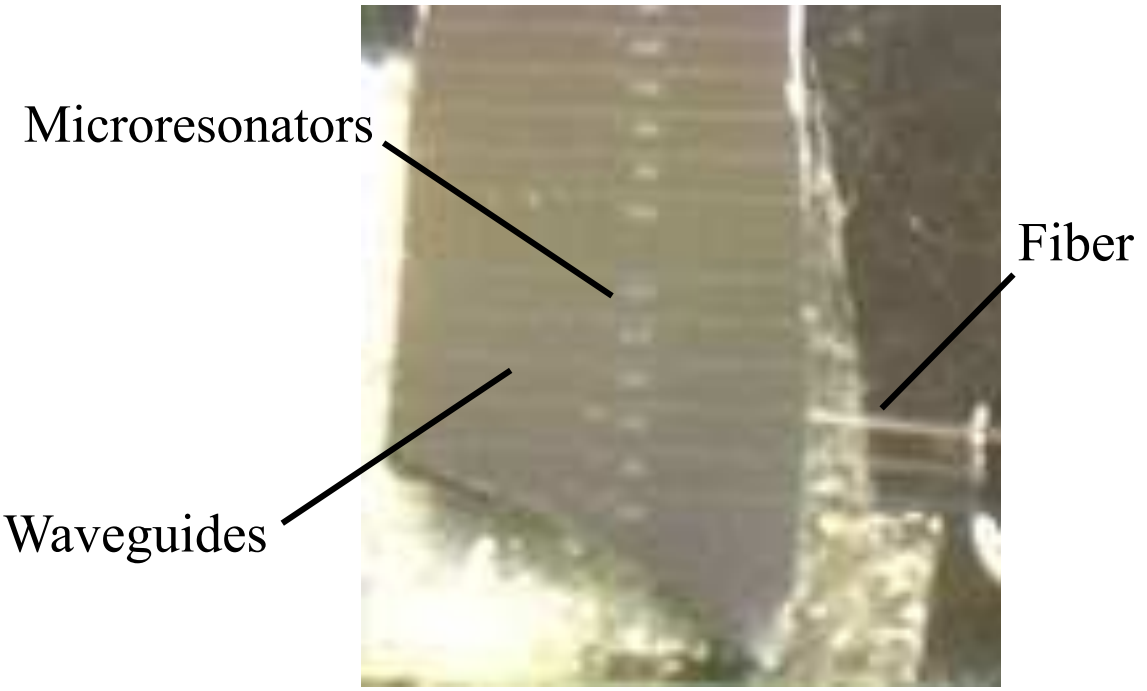

Figure 3.6: Photograph of a chip, on which microresonators and waveguides are seen, as well as the excitation fiber. The orientation of the fabrication of the waveguides is important, because the wafers must be cut perpendicularly to the waveguides to have smooth end faces for good coupling.

transmission spectra are collected as txt files as the raw data. Transmission dips in each transmission spectra correspond to WGMs. Using a mode tracking algorithm (see Appendix, Section 9.1), spectral positions of each WGM can be tracked. These modes are tracked and analyzed under different air humidity levels ranging from 0% to 50%.

Humidity levels are changed using a mixture of N_2 and fully humidified N_2. Dry N_2 is passed through a gas bubbler filled with water to fully humidify N_2. This arm of the gas tube is assumed to be 100% relative humidity (RH). Then it is mixed with the other arm containing dry N_2 (0% RH). Gas flow rates in two arms are adjusted with computer-controlled gas flow meters, to obtain any desired value of RH (see Figure 3.1-a). Then the mixture is pushed into the gas chamber, where the SU-8 microdisk resonator sensor resides together with the input and output fibers. As the humidity

level is changed in the gas chamber, spectral shifts are recorded and plotted against the RH.

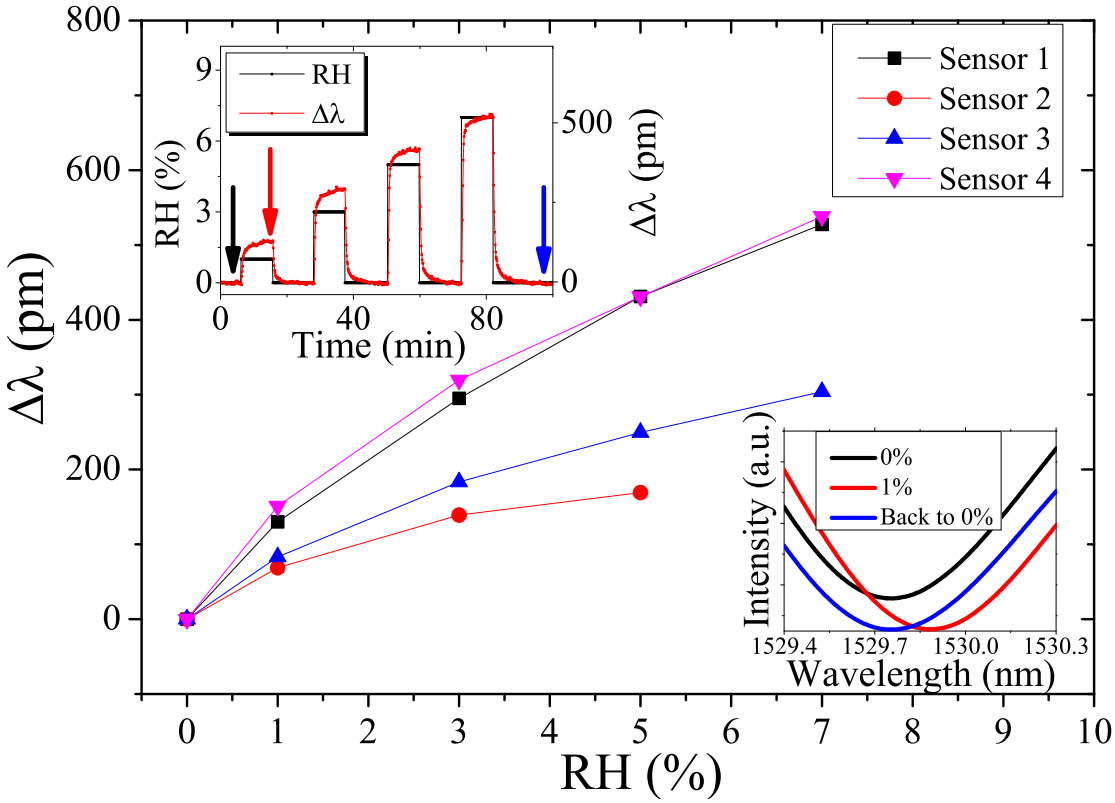

Figure 3.7: Sensing results from multiple sensors when humidity is changed in on-off manner. Inset at the upper left shows the time trace of the resonance shift as well as the RH change in the gas chamber as a function of time. The inset at the lower right shows the tracked WGM during the experiment. Black (0%), red (1%) and blue (back to 0%) curves correspond to points on the time trace inset indicated by the black, red and blue arrows, respectively. Both insets belong the results of Sensor 1. Between 0 and 1%, sensitivities are 130, 69, 83 and 151 pm, respectively for Sensors 1 to 4.

At the beginning of each experiment, the SU-8 microdisks are exposed to dry N_2 for at least 1.5-2 hours to remove the environmental humidity, that is present due to the conditions in the lab. Then RH is changed up to 7% in two different manners. First, RH is changed in an on-off manner. Specifically 0%, 1%, 0%, 3%, 0%, 5%, 0%, 7% and 0%. On-off manner introduction of humidity is used for a couple of

reasons. So-called zero level of the sensor (spectral position of the WGM under 0% RH) is checked after exposure to different levels of RH. Another reason is to be able to calculate response and recovery times for each level of RH. Figure 3.7 shows responses of four sensors to changing humidity in an on-off manner. Sensors 1 and 4 agree well with each other, whereas other two sensors seem to be less sensitive. Individual sensitivities of Sensors 1 to 4 are 130, 69, 83 and 151 $pm/\%\ RH$, respectively when RH is changed from 0% to 1%. The deviation between sensitivities of Sensors 1-4 can be explained by microdisk thickness variations from sensor to sensor [Mata et al., 2006], local differences appearing in SU-8 during cross-linking [Ong et al., 2006], and differences due to fabrication errors.

In the upper-left inset of Figure 3.7, an exemplary time trace is depicted for Sensor 1. The WGM tracked during the experiment featuring Sensor 1 is depicted on the lower-right inset of Figure 3.7. Each arrow in the upper-left inset corresponds to a spectrum of the same color in the lower-right inset. At the beginning of the experiment, when RH is 0% (black arrow and black spectrum), tracked WGM is at 1529.74 nm. When RH is increased to 1%, WGM red-shifts by 130 pm (red arrow and red spectrum). At the end of the experiment, WGM comes back to the initial value (blue arrow and blue spectrum). There is a change in the intensity of the WGM resonance which may be due to many reasons such as intensity fluctuations of the laser, slight misalignment between the fiber and the waveguide or environmental conditions. However, WGM resonance-based sensing is insensitive to fluctuations of the intensity, only the spectral position of the WGM is important.

From time traces of Sensors 1 to 4, their response and recovery times are calculated (see Figure 3.8). Response time for a specific RH value is defined as the time required for $\Delta\lambda$ to reach 90% of its final amount after the RH is changed from 0% to the specific value in question. If the change is minute such as from 0% to 1% RH, response time is high, i.e., $\sim 200\ s$ on average. This is attributed to the fact that there is a small amount of humidity in the environment. For $\Delta\lambda$ to occur, humidity must bind at the parts of the microresonator where WGMs propagate. This takes time, as there is not

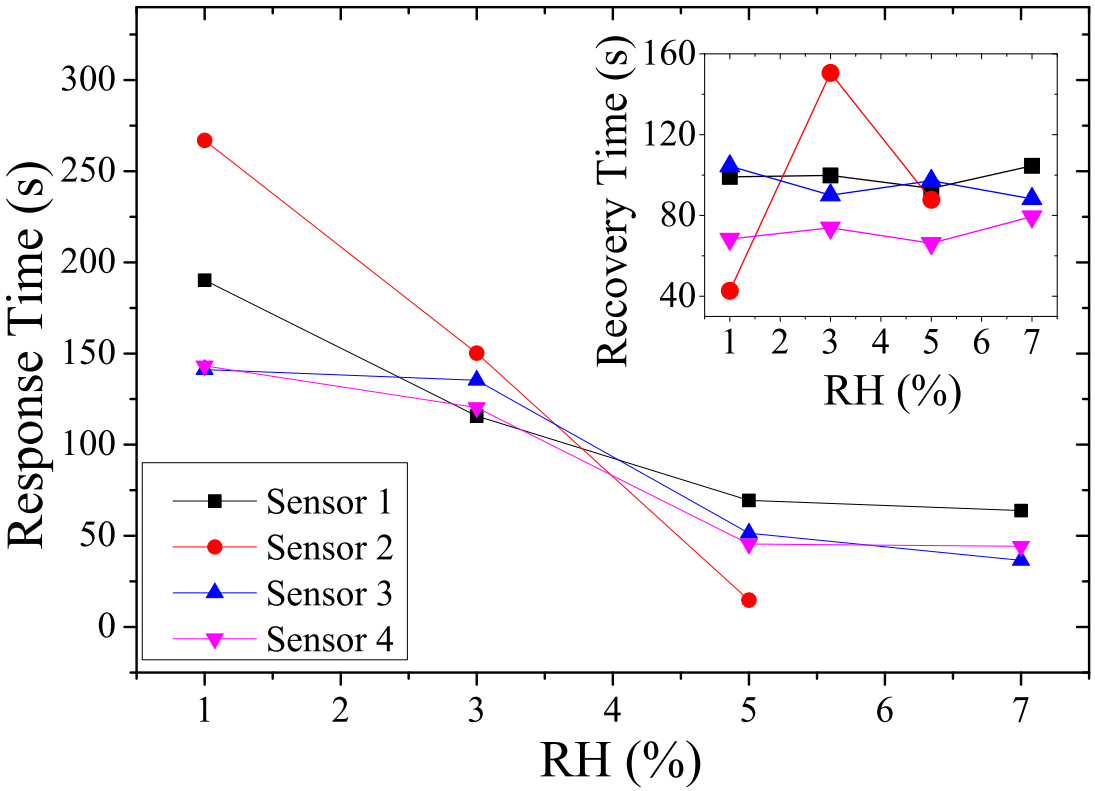

Figure 3.8: Response times of the sensors depicted in Figure 3.7. Response of the sensors become faster as the RH is increased from 1% to 5%, and stays constant afterwards. The inset shows the recovery times of the sensors. Recovery of the sensors stay more or less constant throughout the range of 1% to 7% RH.

enough humidity in the environment to saturate the binding. If RH changes more, then the response time decreases. Specifically, from 0% to 3%, average response time is $\sim 120\ s$, whereas it is $\sim 50\ s$ for RH change from 0% to 5%. After 5% RH, enough humidity is present in the chamber and the response time stays constant at $\sim 50\ s$ (see Figure 3.8).

Recovery time is depicted in the inset of Figure 3.8. Recovery time for a specific RH value is defined as the time required for $\Delta\lambda$ to reach 10% of its initial amount after the RH is changed from the specific value in question back to 0%. Recovery times stay constant $\sim 90\ s$ over the range of 1% to 7% RH. This is attributed to the constant flow rate of dry N_2 introduced into the environment to wash away the

humidity. Deviation of recovery times from sensor to sensor can be explained by differences in local structures between the sensors [Ong et al., 2006] and the SU-8 thickness between different parts of the wafer [Mata et al., 2006].

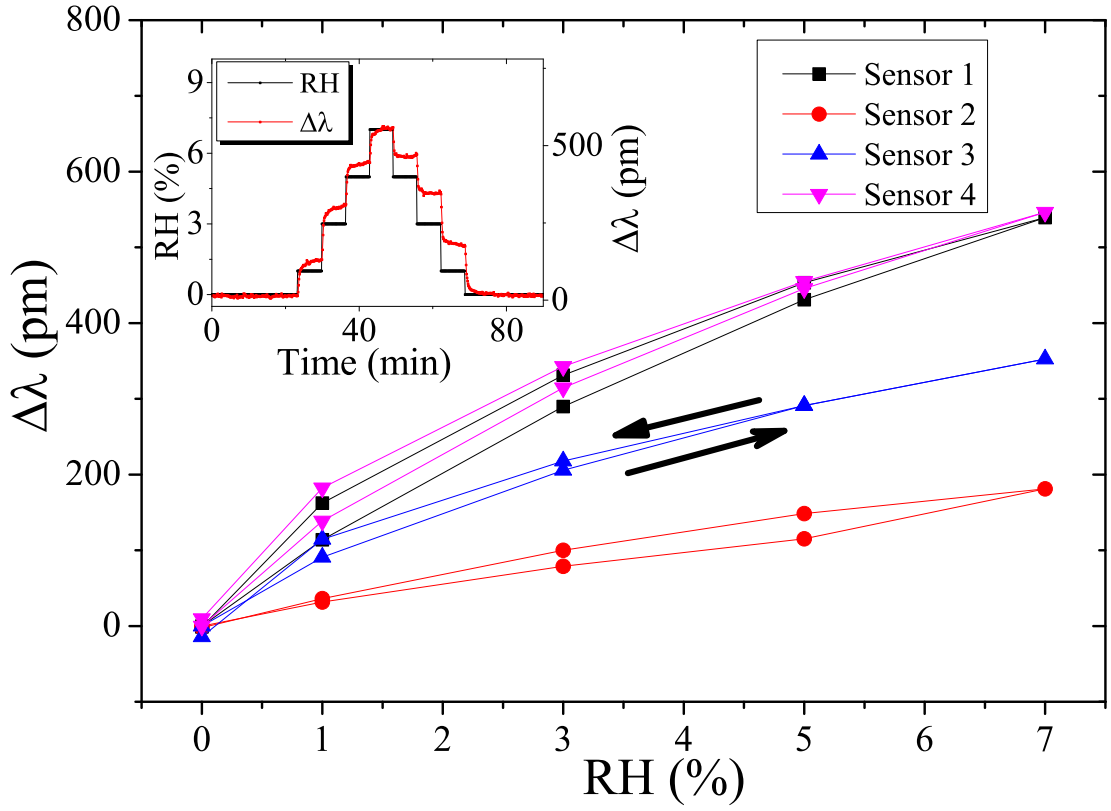

Figure 3.9: Sensing results from multiple sensors when humidity is changed in staircase manner. Sensors 1-4 are the same sensors depicted in Figure 3.7. For all the sensors, humidifying curves are below the dehumidifying curves. This is also indicated by the two black arrows pointing the humidifying and dehumidifying directions. Hysteresis (Hys) is calculated to be 17% from the average of 1%, 3% and 5% RH. The inset shows time trace of Sensor 1. Zero level is preserved.

Although response and recovery times are in the order of minutes, actual values are expected to be less. Firstly, there is a time delay between the setting of flow rates for the flow controller and the launch of the gas flow. Secondly, reaching of the gases after the setting of the flow rate takes time because of the volume of the gas tubes and the gas bubbler between the gas container cylinders and the gas chamber. Thirdly, each wavelength scan requires $\sim 8\ s$ of time, putting more delay to acquiring the shift

data. Finally, removing water from inside the SU-8 with dry N_2 flow may not be the fastest method since polymers and humidity interact very strongly. The last reason is only eligible for recovery time.

The second manner of introduction of humidity is staircase manner. Specifically 0%, 1%, 3%, 5%, 7%, 5%, 3%, 1%, 0%. It is chosen to investigate so-called hysteresis of the sensor at each level of RH. Hysteresis is defined as the difference between WGM resonance position for a given RH level when the humidity is being decreased (dehumidifying) and increased (humidifying) (see Figure 3.9). Mathematical definition is given as:

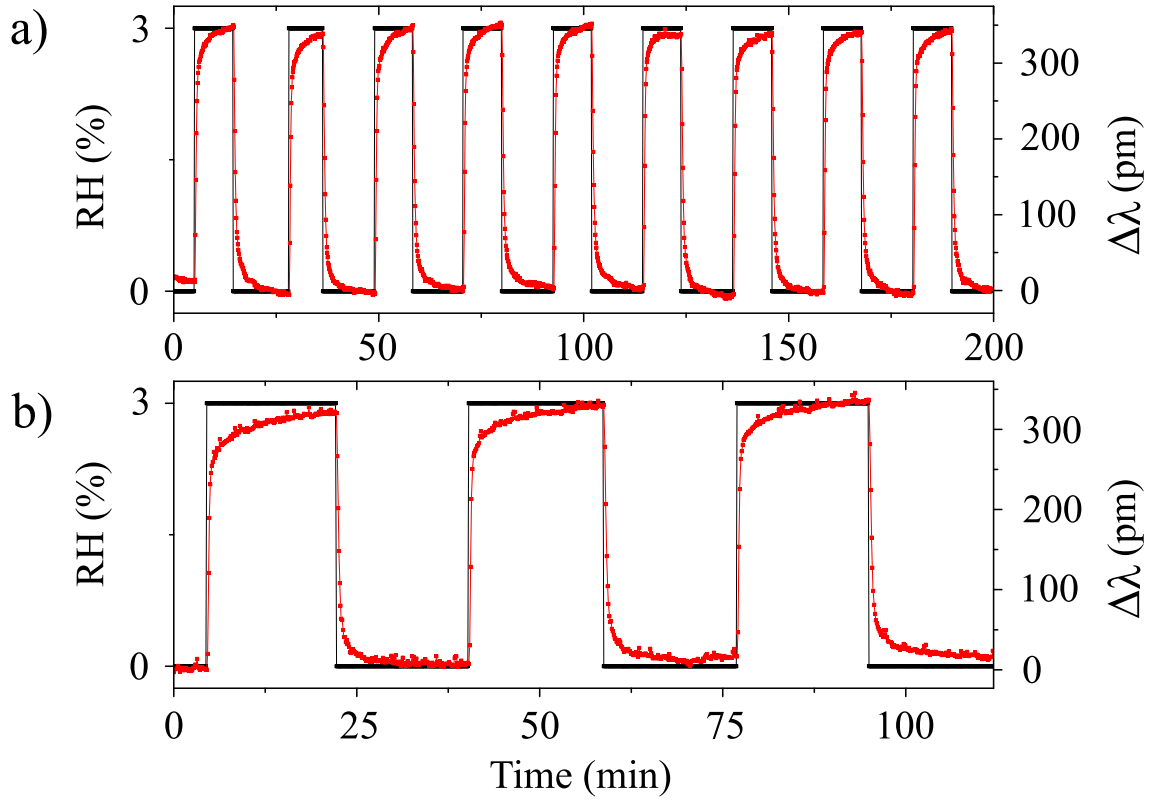

Figure 3.10: a) Multiple on-off cycles performed on a sensor. b) More on-off cycles 45 days after the experiment depicted in a). $\Delta\lambda$ is between 334 and 340 pm for a) and in b) it is between 317 and 322 pm.

$$Hys = \frac{\Delta\lambda_{dehum} - \Delta\lambda_{hum}}{\Delta\lambda_{hum}}$$

where Hys is the hysteresis, $\Delta\lambda_{dehum}$ and $\Delta\lambda_{hum}$ are WGM resonance shifts between 0%, and RH value in question during dehumidification and humidification, respectively. Using this formula, average hysteresis is calculated to be 17% for Sensors 1 to 4 in Figure 3.9. 0% and 7% are not taken into account in the calculation of Hys because $\Delta\lambda_{dehum}$ and $\Delta\lambda_{hum}$ are not properly defined for 0% and 7% RH. When Figures 3.7 and 3.9 are compared, their general behavior is the same, when individual sensors are considered.

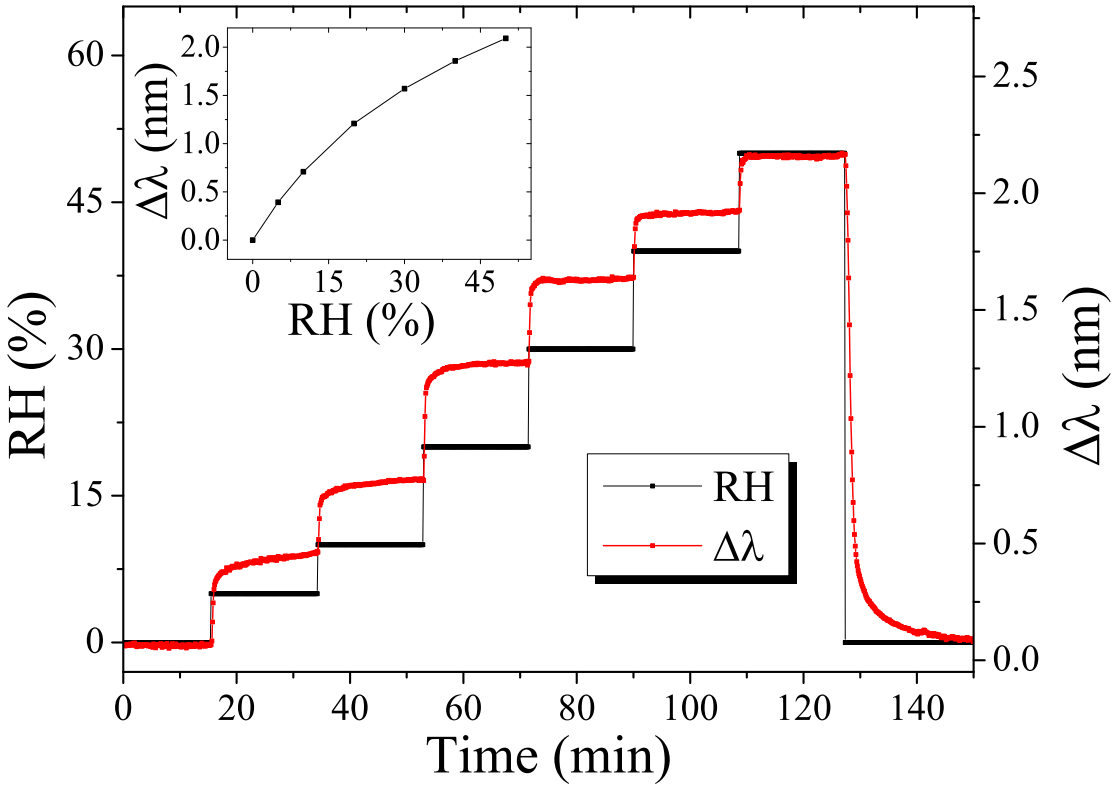

Figure 3.11: Time trace of the response of the sensor to high RH values up to 50%. Although nonlinearly, the spectral shift increases with the humidity. Also, the zero level is conserved. The inset shows the measured values from the time trace in the main figure.

Repeatability, long-term stability (see Figure 3.10) and exposure to high levels

of humidity (up to 50% RH, see Figure 3.11) of the SU-8 microdisk sensors are also investigated. These sensors show very good repeatability under multiple on-off cycles. In Figure 3.10-a, $\Delta\lambda$ is measured to be between 334 and 340 pm over nine on-off cycles, meaning a deviation less than 2%. Then the sensor is kept under ambient environment for 45 days, and another on-off measurement is performed (see Figure 3.10-b). This time, $\Delta\lambda$ is measured to be between 317 and 322 pm, drifted from the initial values by a small amount (~ 5 %).

SU-8 microdisk resonators are also operational at higher levels of RH up to 50% RH. A saturation trend is observed as seen in the inset of Figure 3.11. RH levels up to 70% are also investigated. Saturation trend continues up to 70% RH. However, the mode tracking algorithm does not function properly when RH is changed from 70% back to 0%. This is because when the change is sudden, the algorithm is fooled and jumps to different modes, resulting shifts in the unexpected direction. Therefore it is possible to detect smaller changes in RH, but when the change is huge such as from 70% to 0%, the algorithm does not function properly.

Chapter 4

HYDROGEN GAS SENSOR BASED ON PALLADIUM-COATED SU-8 MICRODISKS

4.1 Introduction

In this chapter, hydrogen gas detection using Pd-coated SU-8 microdisk resonators is presented. Hydrogen gas is a very clean fuel, producing less emission than other fossil fuels [Griffin et al., 2013]. Also, hydrogen is the most abundant element in the universe, which makes it a very decent candidate as the future fuel for energy applications [Dinçer, 2002]. On the other hand, hydrogen gas sow danger because it is odorless, colorless and difficult to store due to its small molecular volume and weight [Alam et al., 2013]. Moreover, lower flammable limit of hydrogen gas in the air at room temperature is 4% [Bévenot et al., 2000]. Hence hydrogen leakages are dangerous for public health and property, even for low concentrations at room temperature. This necessitates quick and sensitive detection of hydrogen gas at room temperature below the flammable limit [Griffin et al., 2012]. Therefore many studies towards hydrogen gas sensing have been presented using different approaches [Hübert et al., 2011]. Because of the reasons listed in Chapter 3 (compactness and insensitivity to electromagnetic interference and intensity fluctuations), WGM-based optical detection is an attractive method for hydrogen sensing [Eryürek et al., 2015, Tripathy et al., 2014].

In the literature, WGM-based hydrogen detection is only investigated once [Yebo et al., 2009]. This study takes advantage of the catalytic combustion of hydrogen gas in the air. The combustion is catalyzed by Pt-doped WO_3 coating residing on silicon-on-insulator (SOI) ring resonator. Due to thermo-optic effect, the resonances

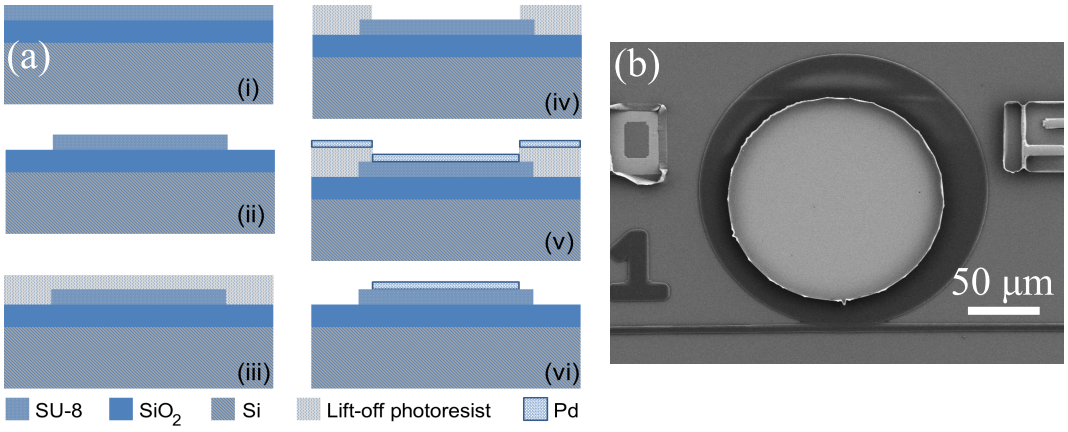

Figure 4.1: a) Fabrication flow of Pd-coated SU-8 microdisk resonators. i) Spin coating of SU-8 on a thick-oxide Si wafer. ii) Fabrication of SU-8 microdisks and waveguides. iii) Spin coating of sacrificial lift-off photoresist. iv) Patterning of the sacrificial photoresist. v) Sputtering Pd. vi) Removal of the sacrificial photoresist. b) SEM image of the fabricated sensor. Pd microdisk can be seen on top of the SU-8 microdisk.

red-shift with a sensitivity of 480 $pm/\%\ H_2$, corresponding to a detection limit of 0.7 % H_2 [Yebo et al., 2009]. In the context of this thesis, Pd-coated SU-8 microdisk resonators are employed for hydrogen gas sensing with successful detection down to 0.3% H_2 and a theoretical lower detection limit of 0.07 % H_2 [Eryürek et al., 2015].

4.2 Fabrication of Pd-Coated SU-8 Microdisk Resonators

Fabrication flow of the Pd-coated SU-8 microdisk resonators is depicted in Figure 4.1-a. First SU-8 microdisks and waveguides are fabricated using the same process flow described in Chapter 3 for humidity sensing (i, ii). Then a sacrificial photoresist (AZ 9260) is spin-coated (iii) and patterned (iv) with the help of mask aligner. Choice of the sacrificial photoresist lies in the fact that, removal chemical of the sacrificial photoresist must not etch the cured SU-8 layer. Finally, Pd is sputtered (thickness of Pd disk is $\sim$ 200 nm) (v), and the sacrificial photoresist is removed using acetone (vi), which does not harm the cured SU-8 structures. This is known as lift-off technique. Because they are not critical to the overall fabrication, the lift-off param-

eters are neither characterized nor optimized. Only noteworthy lift-off parameter is, thicker sacrificial layer allows less time required for the lift-off. It is necessary to have concentric SU-8 and Pd microdisks with Pd microdisks having smaller radii to avoid reflection and absorption of the WGM by the Pd. SEM image of the end product can be seen in Figure 4.1-b.

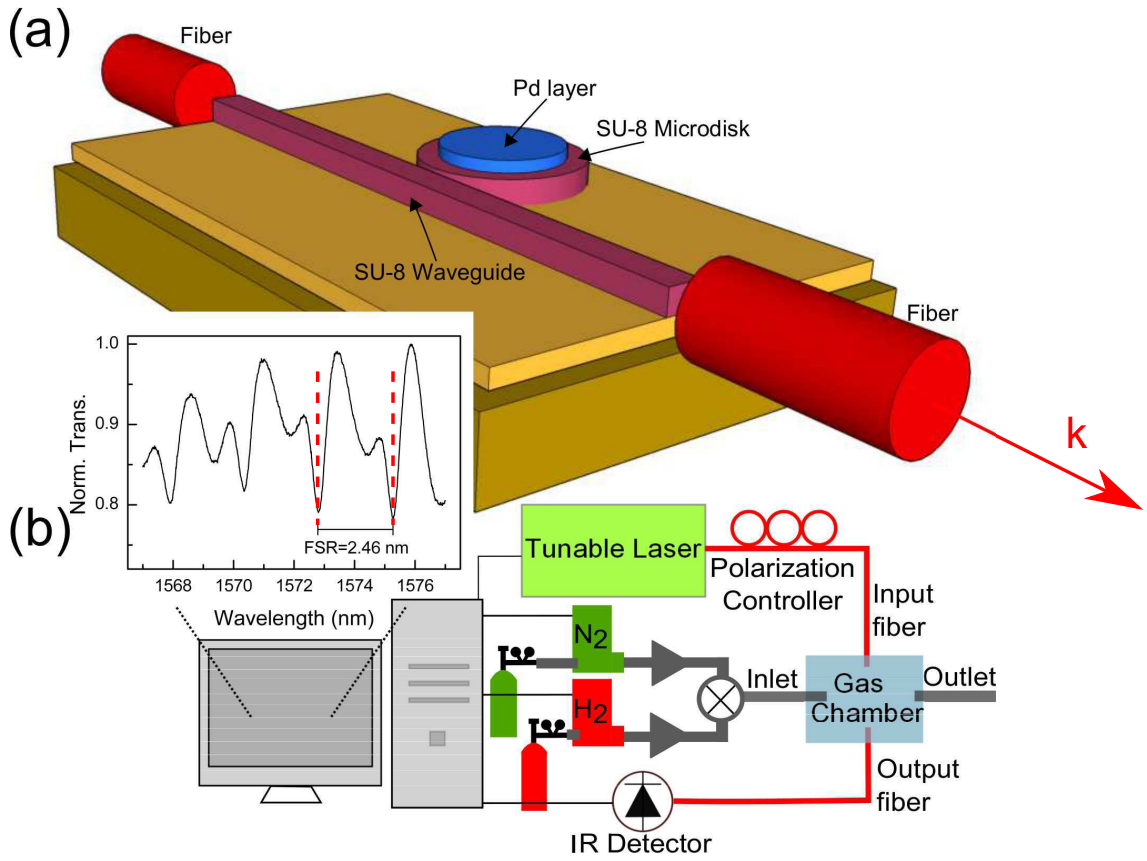

Figure 4.2: a) Schematic visualization of end-face coupling. b) Experimental setup for H_2 sensing experiments. H_2 and N_2 gases are mixed to obtain desired concentrations of H_2 using computer-controlled gas flow controllers, similar to the humidity sensing setup. The inset shows an exemplary transmission spectrum of the SU-8.

Pd is chosen because of its unique interaction with H_2. Even at room temperature, H_2 is adsorbed inside the Pd and PdH_w is formed. Here w represents the H_2 ratio in PdH_w. The lattice constant of PdH_w larger than that of Pd, therefore the volume of the Pd disk expands by 0.13% when H_2 concentration is increased from 0% to 1.5%

[Noh et al., 2011]. This is one of the reasons why Pd is a widely-used active material for hydrogen gas sensing applications [González-Sierra et al., 2017]

4.3 Sensing Mechanism

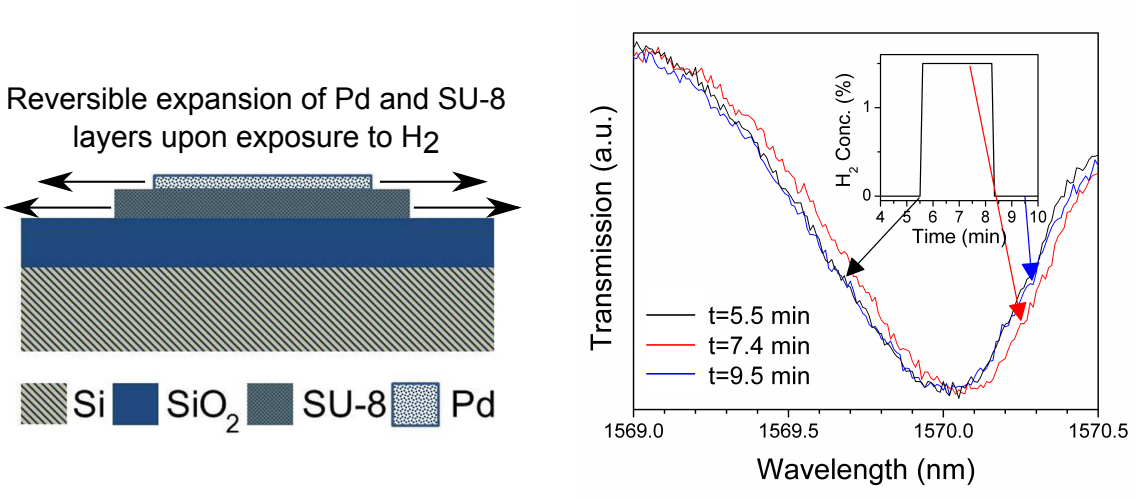

Figure 4.3: a) Schematic cross sectional view of the Pd-coated SU-8 microresonator. Expansion of the Pd induces an expansion for SU-8 microresonator. b) Change in the transmission spectrum while the c_{HYD} is changed from 0% to 1% and then back to 0%. The inset shows the points where the transmission spectra belong to.

Unlike the humidity sensing case, the sensing mechanism relies on Δa of SU-8 microresonators [Eryürek et al., 2015]. This expansion is due to a shear stress produced on the SU-8 microdisk because Pd expands in the presence of hydrogen gas [Noh et al., 2011]. Since the path length of the WGM propagating inside the resonator increases with the diameter, the WGM resonances experience a red-shift. This shift is monitored and analyzed as described in the humidity sensing case (see Chapter 3). To compare the effect of Δa with ΔN, uncoated SU-8 microdisk resonators are exposed to hydrogen gas, where only ΔN is present. Using the parameters presented, $\Delta\lambda$ due to Δa is $\sim$ 20-fold larger than the ΔN which means Δa effect is dominant effect in the H_2 gas sensing with Pd-coated SU-8 microresonators (see Section 4.4).

4.4 Hydrogen Gas Sensing Measurements

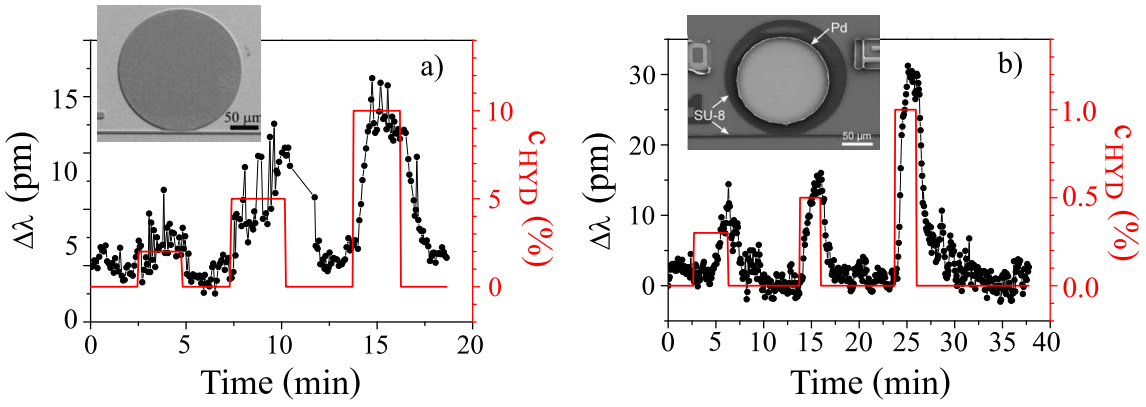

Figure 4.4: H_2 sensing results for a) uncoated SU-8 microdisk resonator and b) Pd-coated SU-8 microresonator. Red lines represent the H_2 concentration whereas black dots represent the $\Delta\lambda$. For uncoated devices, under $c_{HYD} = 10\%$, ~ 15 pm resonance shift occurs whereas under $c_{HYD} = 1\%$, ~ 30 pm is obtained when Pd-coated SU-8 microresonator is used. In the insets, SEM images of the corresponding sensors are depicted.

Measurement setup of hydrogen sensing experiments is very similar to the one used for humidity sensing. Tunable laser light (Santec TSL-510-C, tunability range: 1500 nm - 1630 nm, wavelength resolution: 1 pm) is coupled to SU-8 waveguide using end-face coupling method (see Figure 4.2-a). The transmission spectrum is recorded as the wavelength of the tunable laser is changed (see the inset in Figure 4.2). Computer controlled gas flow meters are used for mixing N_2 with H_2, so that desired concentrations of H_2, c_{HYD}, can be obtained in the gas chamber (see Figure 4.2-b). Since it is important to detect H_2 at the concentrations below the explosion limit (4% at room temperature), only small concentrations of H_2 have been investigated. Also, reversible operation is only available between 0 and 1.5% where PdH_w is in its reversible alpha-phase [Noh et al., 2011]. Schematic description of the expansion is depicted in Figure 4.3-a. In Figure 4.3-b, WGM spectra for 0% H_2 (black), 1% H_2 (red) and back to 0% H_2 (blue) are depicted. The WGM comes back to initial position after red-shifting by ~ 30 pm. If higher concentrations are introduced, then PdH_w

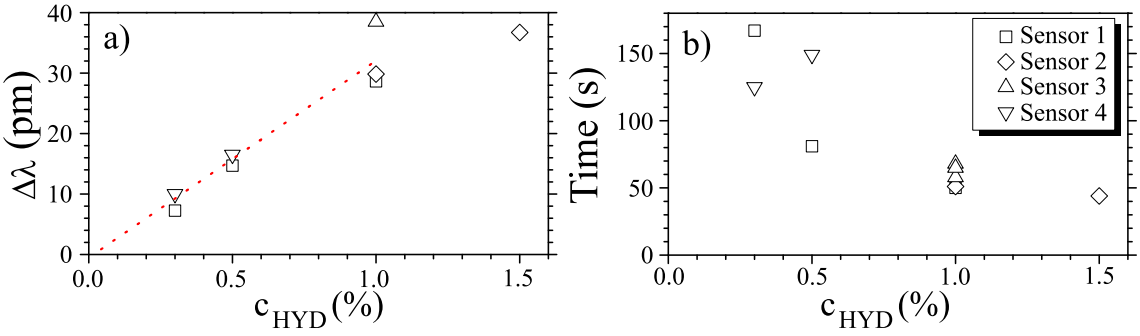

Figure 4.5: a) Sensitivity measured from multiple sensors. The dashed red line is the linear fit to the average of the sensor responses for H_2 concentrations between 0 and 1%. Slope is calculated to be 32 $pm/\%H_2$. b) Response times of these sensors. Response time decreases with the increasing concentration of H_2.

is in its beta-phase, where higher and irreversible deformations occur in PdH_w [Noh et al., 2011].

In Figure 4.4, uncoated and Pd-coated SU-8 microdisk resonators are compared to each other regarding H_2 sensing capability. Uncoated microdisks, although not very sensitively, detect H_2 based on ΔN [Sato et al., 2011] induced by the formation of PdH_w. H_2 concentration has to be increased well above the flammable limit of 4% to obtain a detectable $\Delta\lambda$. At $c_{HYD} = 10\%$, $\Delta\lambda$ is measured to be ~ 15 pm. However, when the Pd coating is employed, ~ 30 pm of $\Delta\lambda$ is measured for $c_{HYD} = 1\%$. This indicates $\sim$ 20-fold improvement in the sensitivity from uncoated microdisk to Pd-coated microdisk, under the presented geometrical parameters. Therefore ΔN effect is negligible as compared to the Δa effect. Sensitivity can be further increased, if the Pd coating is thicker or the substrate is chosen from a more flexible material such as polydimethylsiloxane (PDMS).

By analyzing the four sensors, the sensitivity of Pd-coated SU-8 microdisk sensors to c_{HYD} between 0 and 1% is calculated as 32 $pm/\%$ H_2 from Figure 4.5-a. Figure 4.5-b shows the response time of these sensors. Similar to humidity sensing case, response time decreases with increasing c_{HYD}, which is attributed to the fact that the lower the c_{HYD}, the longer it takes for H_2 to saturate the Pd to form PdH_w.

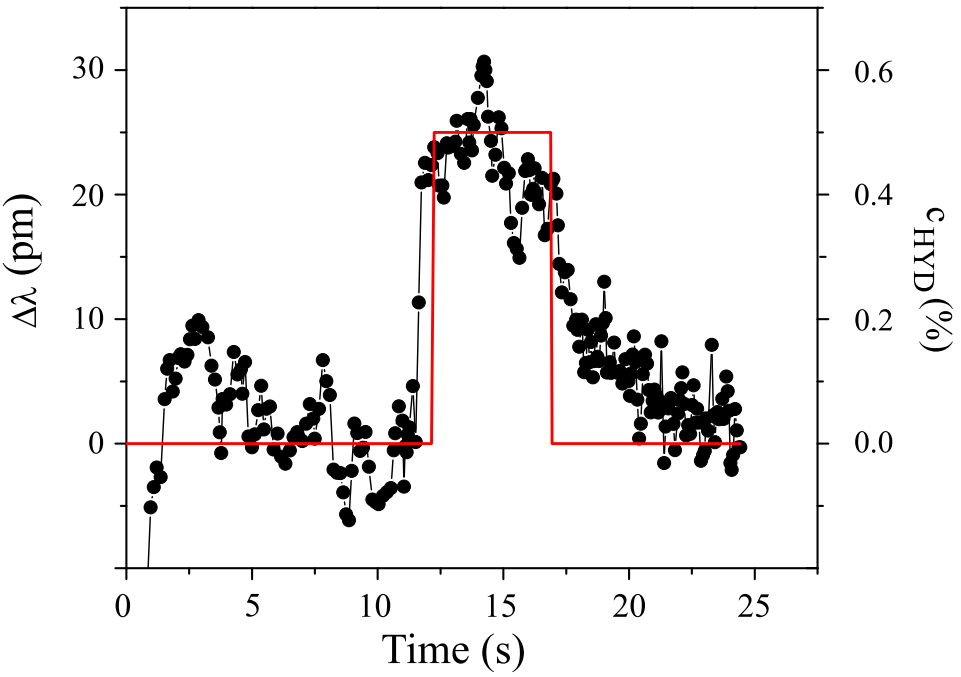

Figure 4.6: H_2 sensing results under humid N_2. Although the fluctuations are higher than dry N_2 environment, still $c_{HYD} = 0.5\%$ is detected under humid environment.

H_2 detection capability of Pd-coated SU-8 microdisk sensors is investigated under humid N_2 environment to test their suitability for practical applications. Only one sensor is investigated in the context of the work, and more experiments are required for the characterization of sensitivity and response time. It is shown that the sensor still responds to the H_2 in the presence of humidity down to $c_{HYD} = 0.5\%$ (see Figure 4.6). However, fluctuations in $\Delta\lambda$ is more than dry N_2 environment case.

Chapter 5

LIQUID REFRACTOMETRIC SENSORS BASED ON OPTICAL FIBER RESONATORS

5.1 Introduction

In this chapter, detection of refractive index changes of the surrounding liquid medium is presented. Very easy preparation of microcylindrical resonators from standard optical fibers presents a low-cost and robust sensing platform [Boleininger et al., 2010]. Instead of the conventional propagation of light along the fiber axis, the light propagates along the azimuthal direction of the fiber (see Figure 5.1) [Eryürek et al., 2017a]. Fibers employed in this kind of azimuthal excitation are known as optical fiber resonators (OFRs) [Eryürek et al., 2017a]. Sensing is performed via the interaction between the evanescent tail of the WGM in the azimuthal direction and the ambient environment. Evanescent tail-based sensing of ΔN_{out} (changes in N_{out}) is quite a powerful platform for liquid refractive index sensing [Ioppolo et al., 2010]. Up to date, other sensitive microresonators are employed in refractive index sensing [Fan et al., 2008, Hanumegowda et al., 2005, Sun and Fan, 2011, Wang et al., 2014, White et al., 2006]. Only one study investigates OFRs under changing ambient refractive index using evanescent field interaction [Boleininger et al., 2010]. In that work, characterization of N_{out} is not referred. Rather only the pure air-pure water and pure water-pure ethanol environments are investigated. Also, the polarization of the WGMs is not mentioned.

In this chapter, refractometric sensing of the ambient environment (N_{out}) is presented. An OFR and a tapered fiber are held in a perpendicular geometry (see Figure 5.1). TM and TE polarized excitations are analyzed separately and refractometric

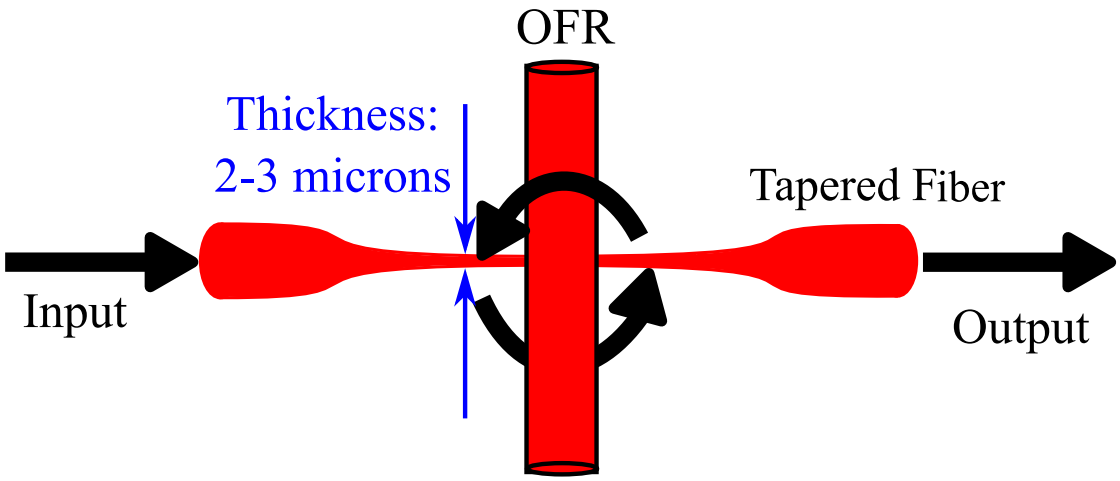

Figure 5.1: A sketch depicting the perpendicular geometry for exciting the WGMs using tapered fiber, as well as the azimuthally propagating WGMs inside the OFR. Black arrows represent the propagation direction of the excitation light.

detection limits of 2.7×10^{-5} and 3.0×10^{-5} RIU are reported, respectively. Moreover, analytical calculations of expected $\Delta\lambda$ are presented under certain ΔN_{out}, for both TM and TE polarizations (see Appendix, Section 9.2).

5.2 Excitation through Tapered Fiber

Instead of coupling to SU-8 microresonators through waveguides as presented in Chapters 3 and 4, azimuthal modes of OFRs are excited using tapered fibers [Boleininger et al., 2010]. Tapering the excitation fiber is required, because standard optical fibers are not thin enough for excitation. Fiber tapering is a technique to adiabatically thin the fiber, so that light propagating inside the excitation fiber can be coupled out. In the tapering technique, the excitation fiber is heated up to high temperatures using a hydrogen flame reaching up to $> 1000°C$ [Ding et al., 2010]. Simultaneously, the fiber is pulled from both ends during the heating (see Figure 5.2). Using this technique, sub-micron tapers are obtained [Jonáš et al., 2012]. For our purposes in which a wavelength of $\sim 1.5\ \mu m$ is used, tapers of diameter $\sim 3\ \mu m$ are sufficient to obtain coupling from the tapered fiber to the fiber resonator (see Figure

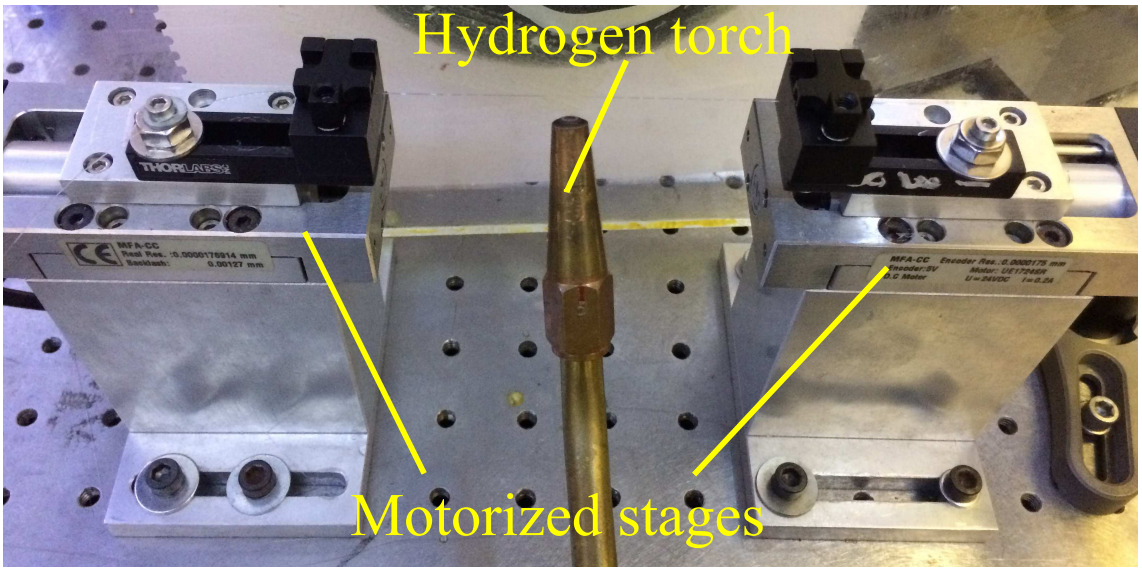

Figure 5.2: Photograph of the fiber tapering setup consisting of hydrogen flame torch, and motorized stages for pulling the fiber.

5.3-a).

To prepare tapered fibers, first the polymer coating on a standard optical fiber is mechanically removed, and the fiber is cleaned with isopropyl alcohol (IPA). Second, the fiber is placed and fixed between two fiber clamps, and it is heated up with a hydrogen flame. Each fiber clamp is pulled by a distance of $\sim 9\ mm$ with a velocity of 0.2 mm/s. After pulling, the tapered region is inspected with a magnifying glass. If the tapered region is not straight and sagged, then necessary amount of additional pulling (usually between 0.02-1.00 mm per clamp) is applied without the hydrogen flame. Additional pulling supplies more strength and robustness to the taper. After the tapering, the fiber is fixed using epoxy glue from two ends (see Figure 5.3-b). Tapered region expresses an exponential thickness profile [Kenny et al., 1991, Villatoro et al., 2003]. Although the middle point has the smallest thickness, there is a tolerance region in the axial direction, where the coupling is possible.

To serve as the OFR, another standard optical fiber is placed on the tapered region of the fiber in a perpendicular geometry [Boleininger et al., 2010]. The WGMs are excited using the same tunable laser as Chapters 3 and 4 (Santec TSL-510-C,

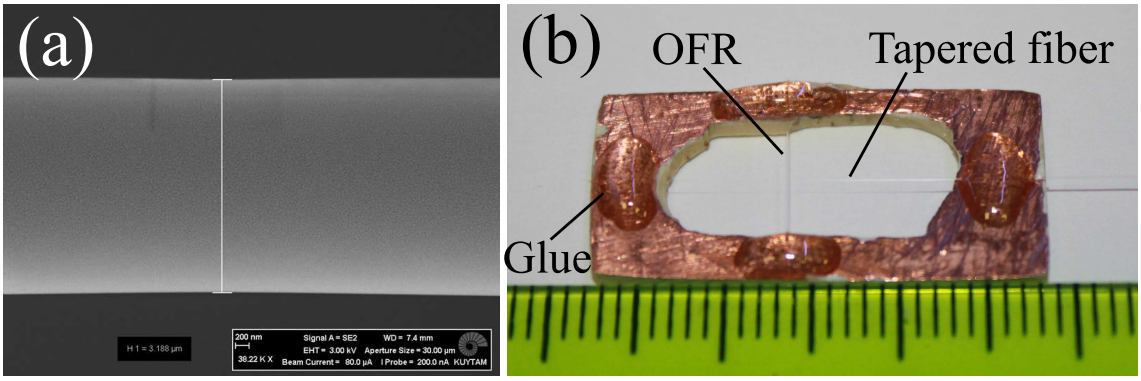

Figure 5.3: a) SEM image of the tapered fiber. The scale shows a thickness of $< 3.2\ \mu m$. b) Photograph of a tapered fiber and OFR pair perpendicularly placed and fixed using epoxy glue. Metric ruler is also provided for scaling.

tunability range: 1500 nm - 1630 nm, wavelength resolution: 1 pm) through tapered fibers. Sensing is characterized by analysis of the transmission spectrum using the same mode tracking algorithm as Chapters 3 and 4. WGMs of the OFRs are revealed in the transmission spectra as transmission dips depicted in Figure 5.4. Spectrum on the left belongs to an OFR in the air and the spectrum on the right belongs to an OFR in pure water. The Q-factors decrease from the air (63000) to the water (16000) due to the absorption of water. Q_{mat} is calculated to be ~ 2000 around $\lambda = 1550\ nm$ by using the absorption coefficient of water as $\alpha \sim 3 \times 10^3\ m^{-1}$. Overall Q-factor value does not decrease down to ~ 2000 because only the evanescent tail of the WGM is absorbed by water. Therefore the overall Q-factor decreases from 63000 only down to 16000 when the ambient environment is changed from air to water.

The FSRs of the transmission spectra are also calculated form Figure 5.4. In the air environment, FSR is $\sim 4.14\ nm$, whereas the FSR is $\sim 4.18\ nm$ in the water environment. FSR seems to be not changing dramatically when the environment is changed, which is justified by the analytical calculations. In both air and water environment, calculated FSR values are 4.16 and 4.15 nm for TM and TE modes, respectively. These values are also in agreement with 4.19 nm obtained from Eq. 1.2.

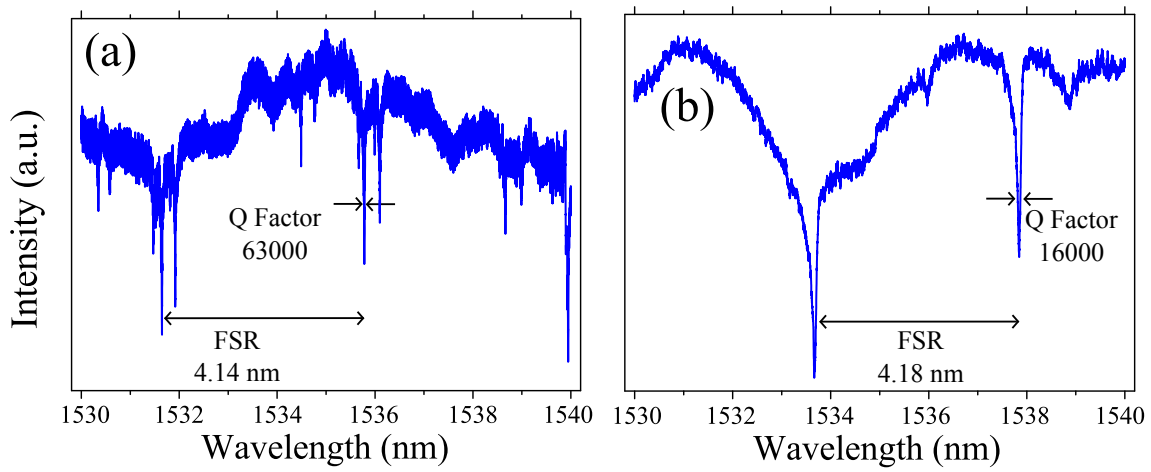

Figure 5.4: Transmission spectra of OFR excited in a) the air, and b) in pure water environment. Q-factor in the air is measured as 63000, but it decreases to 16000 in the water environment because of the absorption of water. FSR is not changed much from the air (4.14 nm) to the water (4.18 nm).

5.3 Sensing Mechanism

Liquid refractive index sensing of the environment using OFR relies on the evanescent tail of the WGM extending into the ambient environment. Although the evanescent tail is ~ 100 nm [Hunt et al., 2010], even minute ΔN_{out} values induce a change in the effective refractive index (N_{eff}) of the WGM. Since the OFRs are rigid resonators, there is no Δa, but there is only ΔN. To increase the sensitivity, however, active materials can be coated on the OFRs so that ΔN can be increased and Δa can also be introduced (see Chapter 7).

5.4 Liquid Refractive Index Sensing Measurements

Liquid refractometric detection setup consists of a tapered fiber-OFR pair in a perpendicular geometry, a liquid chamber, syringe pump and a tunable laser (see Figure 5.5). First, the WGMs are excited in the OFR using Santec laser in the air environment. Then the chamber is filled with DI water and tracking of one of the WGMs is initiated. Different concentrations of EG/water or ethanol/water solutions

are injected using the syringe pump to change the refractive index in a controlled manner. Meanwhile, the WGMs are tracked using the mode tracking algorithm used in Chapters 3 and 4. WGM shift, $\Delta\lambda$ is measured for ethanol or EG solutions for both TE and TM polarizations and the results are compared with the expected $\Delta\lambda$ obtained from the analytical calculations. In these calculations, the refractive indices of water, ethanol, and EG are taken to be $N_{Water}^{1535} = 1.3183$, $N_{Eth}^{1535} = 1.3506$ and $N_{EG}^{1535} = 1.4199$, respectively, at around $\lambda = 1535\ nm$ [Polyanskiy, 2008]. Although the refractive indices of different concentrations of EG/water and ethanol/water are available at around $\lambda = 589\ nm$ [Fogg et al., 1955, Lide, 2012], there is no reference found at around $\lambda = 1535\ nm$. Therefore, the following normalization coefficients (C_{EG} and C_{Eth}) are put to use for estimation of the refractive indices at around $\lambda = 1535\ nm$ via $N^{1535} = C \times N^{589}$.

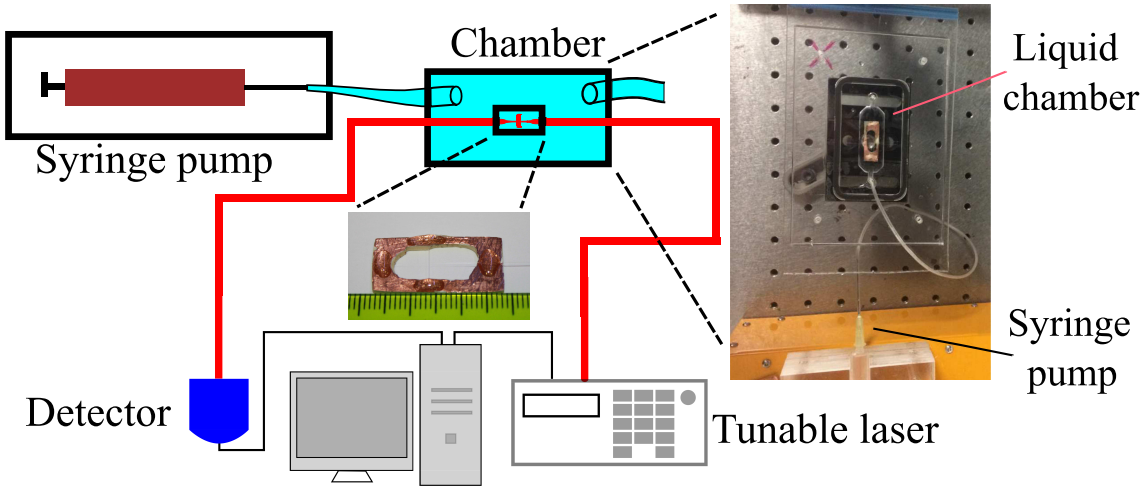

Figure 5.5: Experimental setup for liquid refractometric measurements using OFRs. Water solutions of ethanol or EG are introduced using a syringe pump into the liquid chamber where OFR and tapered fiber are held in perpendicular geometry (see the inset). Tunable laser light coming from the optical fiber is coupled to the OFR in the tapered region.

$$C_{EG} = \frac{N_{EG}^{1535} - N_{Water}^{1535}}{N_{EG}^{589} - N_{Water}^{589}}$$

$$C_{Eth} = \frac{N_{Eth}^{1535} - N_{Water}^{1535}}{N_{Eth}^{589} - N_{Water}^{589}}$$

where N represents the refractive index. At the upper-right of N, the number represents the wavelength of the light. Name of the liquid is written at the lower-right of N. Then expected $\Delta\lambda$ values are calculated using the formula for WGM spectral positions given in Chapter 2 [Bohren and Huffman, 1998, van de Hulst, 1981] and depicted in Figure 5.6. The highest concentration sensitivity is obtained for EG in TM polarization. EG shows more concentration sensitivity because, relative refractive index of EG, $M_{EG} = N_{EG}/N_{water}$ is higher than M_{Eth} (1.0771 and 1.0245, respectively). Calculations also indicate TM polarized-light shows slightly higher sensitivity. This is attributed to the mode volume of TM modes extending more into the ambient environment than the extension of TE modes. Therefore TM modes have more interaction with the ambient, resulting in higher sensitivity.

Figure 5.7-a shows a transmission spectrum at the beginning of an experiment where N_{out} is changed using different concentrations of ethanol (c_{ETH}). Modes associated with the same azimuthal mode number but having different polarizations are revealed as transmission dips near to one another. In Figure 5.7-a, one pair of such modes are indicated as TM_p and TE_p, where p indicates the azimuthal mode number. In the mode pair, the mode having slightly shorter wavelength is taken to be TM mode because of the analytical calculations predict so, and it has been reported that way in the literature [Ta et al., 2013]. Going slightly towards longer wavelengths by an FSR amount, another pair of modes are observed and indicated by TM_{p-1} and TE_{p-1}. If FSR amount of shorter wavelengths are considered, they are indicated as TM_{p+1} and TE_{p+1}. If resonance wavelength is larger, the azimuthal mode number must decrease to keep the resonance condition satisfied. In Figure 5.7-b, shifts of these resonances are depicted when c_{ETH} is increased from 0% to 30%. Measured

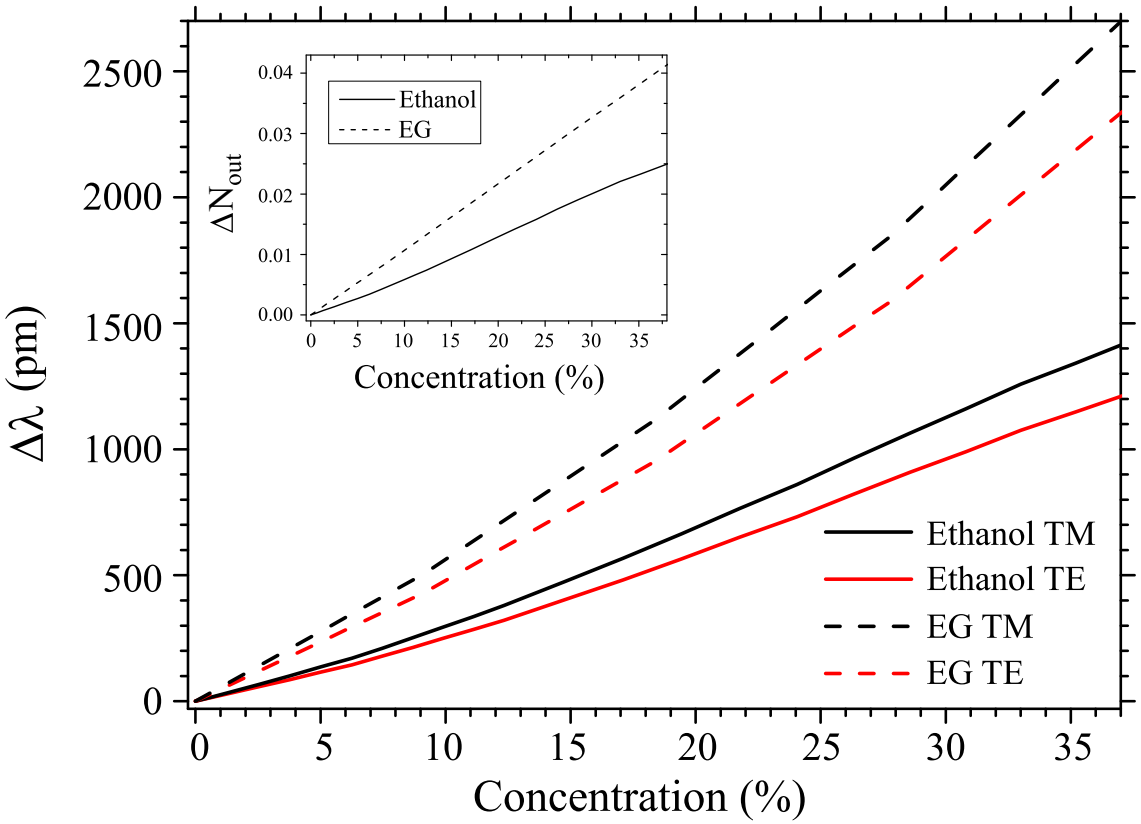

Figure 5.6: Spectral shifts expected from the analytical calculation with respect to ethanol/EG concentration for both TM and TE polarizations. Since EG has higher relative refractive index, slope belonging to EG is higher than the slope of ethanol. Also, TM slope is slightly higher than TE slope. The inset shows the change in the ambient refractive index (ΔN_{out}) with respect to the ethanol/EG concentration. These values are used in calculation of the main figure.

$\Delta\lambda$ values are in a very good agreement with the analytical calculations depicted as dashed lines. Sensitivity of the modes split into two branches as predicted by the analytical calculations.

Figure 5.7-c depicts a transmission spectrum in the beginning of an experiment where N_{out} is changed using c_{EG} between 0% to 25%. Again as predicted by the analytical calculations, sensitivity branches into two for TM and TE polarizations. Also, the sensitivity from the measurements follows the sensitivity predicted by the analytical calculations.

One issue requires addressing is the spectral positions of WGMs in Figure 5.7-a and Figure 5.7-c do not line up perfectly with one another. This is attributed to two reasons. The first reason is, the cladding diameter of the OFR used in the experiments has a variation of $\pm$ 0.7 μm around 125 μm [International Telecommunication Union, 2018, Thorlabs, 1999]. For instance, if the diameter is 125 μm, $N_{in} = 1.46$, $N_{out} = 1.3183$, and $m = 371$, the resonances occur at 1.499555 μm and 1.501005 μm for TM and TE polarizations, respectively. The value of n is chosen such that the resonances are around 1.5 μm. For the same parameters, these resonances become 1.507953 μm and 1.509411 μm when the diameter is increased to $125 + 0.7$ μm. While diameter is $125 + 0.7$ μm, changing m to 373 results resonances around 1.5 μm, specifically 1.500010 and 1.501453. This example suggests a possible resonance difference of $\sim \pm 450$ pm.

The second reason is, possible deviation of the angle between the OFR and the tapered fiber while the OFR is placed manually on top of the tapered fiber. Any deviation from 90° results in a longer effective radius than the radius for which the angle is 90° (see Figure 5.8). In the perpendicular geometry, the WGM plane is a circle with radius $a = 62.5$ μm. Supposing a deviation by an angle γ, WGM plane becomes an ellipse whose radius in the minor axis is $a = 62.5$ μm, but the major axis radius becomes $a/cos\gamma$. Ramanujan's following approximation for the perimeter of the ellipse, O:

$$O \approx \pi a \left[3\left(1 + \frac{1}{\cos\gamma}\right) - \sqrt{\left(3 + \frac{1}{\cos\gamma}\right)\left(1 + \frac{3}{\cos\gamma}\right)} \right]$$

is employed for finding the perimeter [Ramanujan, 1927]. From circle ($\gamma = 0°$) to ellipse ($\gamma = 1°$), the perimeter is increased from 392.699082 μm to 392.728992 μm. Supposing there is an effective radius a_{eff} such that $2\pi a_{eff}$ is equal to the perimeter of the ellipse, a_{eff} is calculated to be 62.504760 μm. Hence the corresponding resonance shift becomes $\Delta\lambda = 118$ pm.

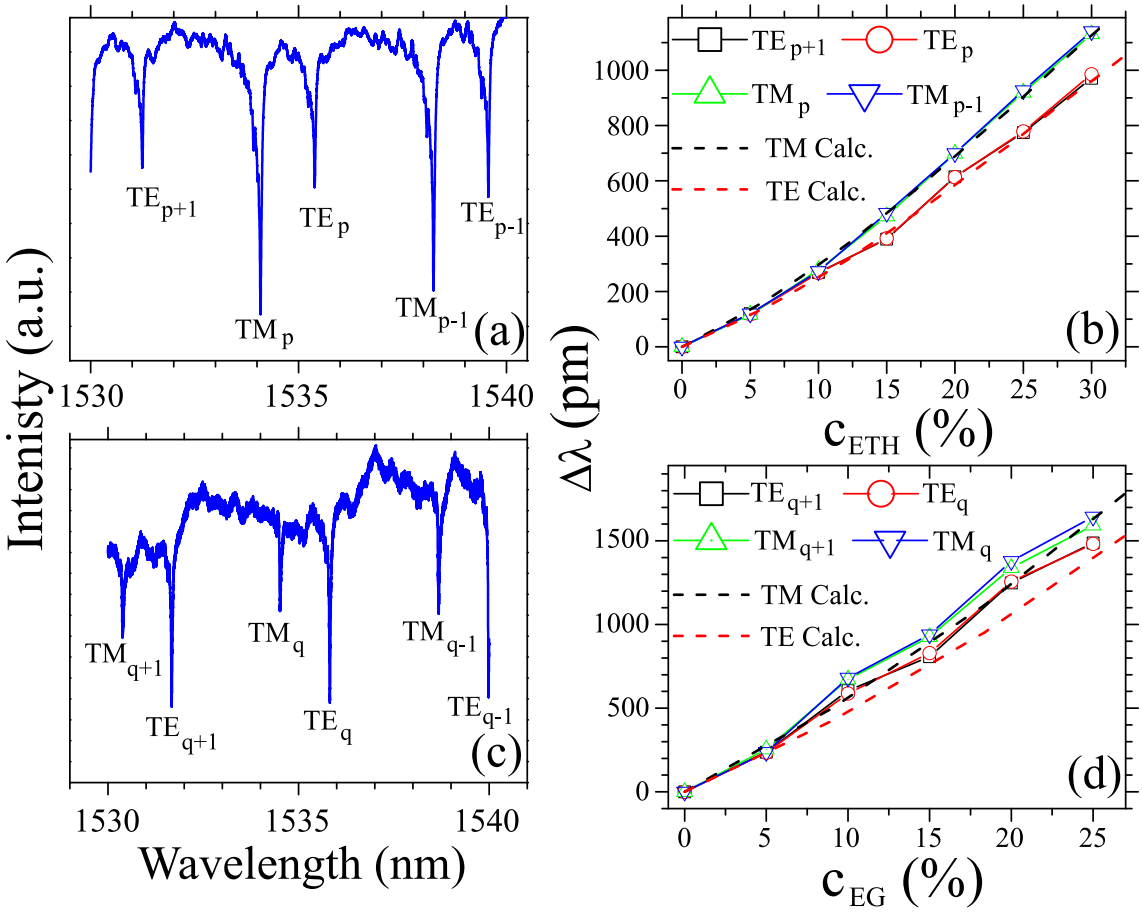

Figure 5.7: Transmission spectrum at the beginning of a) Ethanol sensing experiment and c) EG sensing experiment. p and q represent the azimuthal mode numbers of the corresponding WGMs. Sensing results are depicted in b) and d) for ethanol and EG, respectively. Dashed lines are analytical calculations presented in Figure 5.6

As can be seen from these estimations based on slight changes in the geometrical parameters, spectral positions of WGMs are very sensitive. Hence, it is not clear if the WGMs around $\lambda = 1535\ nm$ in 5.7-a have the same azimuthal mode number with the ones in 5.7-c. Therefore they are indicated by different letters, p and q. Fortunately, these issues are related to the WGM spectra before the refractometric sensing is initiated. Once the OFR and the tapered fiber are placed and fixed in a certain way, it is not disturbed until the end of the experiment. Therefore these issues are not a problem for the refractometric sensing experiments.

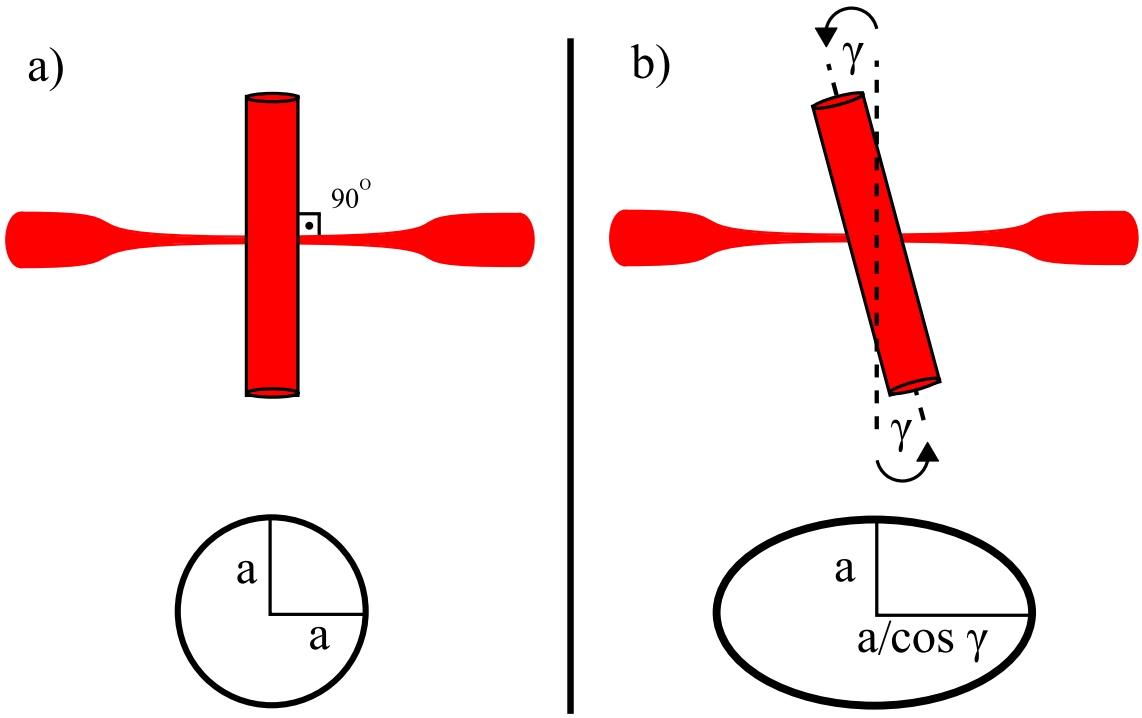

Figure 5.8: Schematic representation of a) perpendicular geometry and b) slightly deviated perpendicular geometry. The deviation is parametrized by the angle γ. WGM plane is circular when $\gamma = 0$. As γ increases, WGM plane becomes an ellipse. The radius of the ellipse in the perpendicular direction, a, is constant, whereas in the other axis radius is equal to $a/\cos\gamma$.

Another difference between Figure 5.7-a and Figure 5.7-c is, amount of decrease in the intensity of TEM or TE modes are different. For instance, in Figure 5.7-a, TE modes have less decrease than TM modes, whereas it is the opposite in Figure 5.7-c. Without the polarization control, it is not possible to eliminate any polarization from the excitation. Therefore both TM and TE modes are excited. The decrease in the intensity, however, is related to the coupling efficiency of the modes. Because of manual placement of the OFR on top of the fiber, TM or TE mode may be coupled to the OFR more efficiently than the other. Slight thickness variations from taper to taper may also cause such a difference in coupling efficiencies.

Time traces and $\Delta\lambda$ values ethanol and EG experiments are depicted in Figure 5.9. At the beginning of the experiments, pure water is injected from the syringe pump.

As the WGMs are tracked, the refractive index of the environment, N_{out} is changed using ethanol or EG concentrations up to 30%. For each concentration, 2 injections are performed for stabilizing N_{out}. This can be observed from Figures 5.9-a and 5.9-c where 2 different jumps occur for any given concentration. After these injections, N_{out} is stabilized since $\Delta\lambda$ values saturate before the injection of the next concentration. Measured $\Delta\lambda$ values are depicted in Figure 5.9-b and 5.9-d on top of the analytical calculations indicated as dashed curves for both TM and TE polarizations.

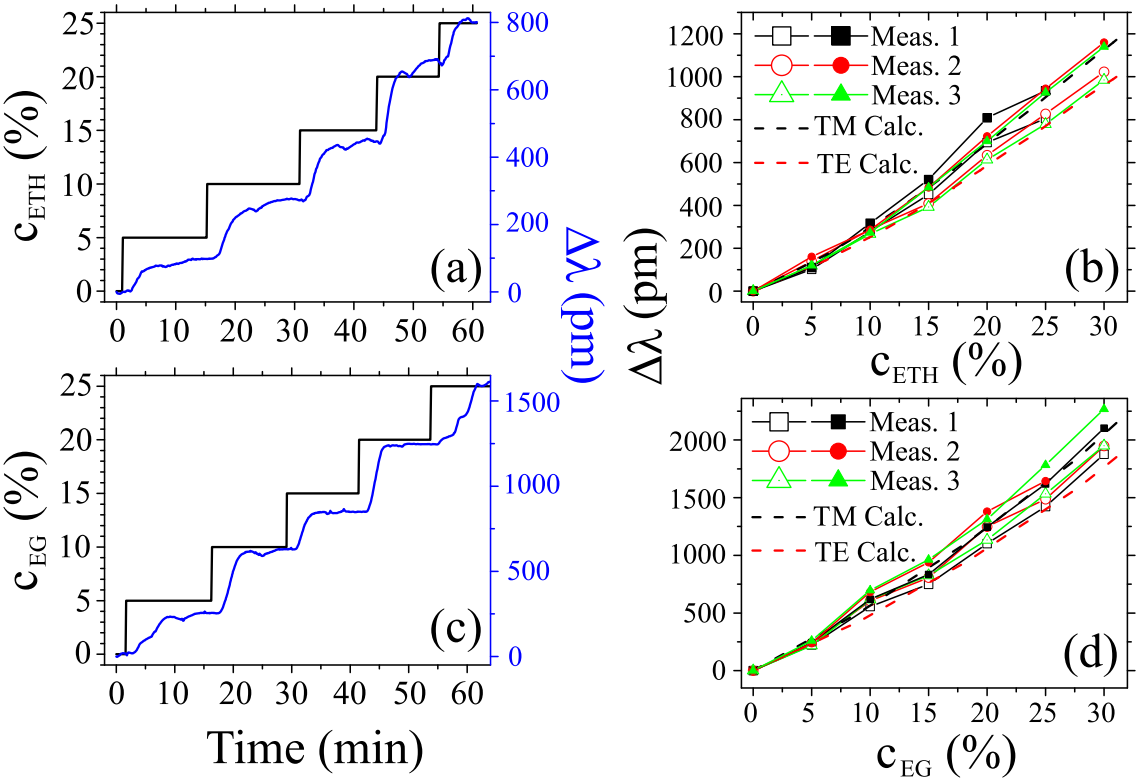

Figure 5.9: Time traces of a) Ethanol and c) EG sensing experiments. Respective results are depicted in b) and d), together with the analytical calculations.

Between 0% and 30%, an approximately linear response is obtained for both ethanol and EG experiments. From the linear fits of three measurements depicted in 5.9-b, ethanol concentration sensitivities are measured to be 39 $pm/\%$ and 34 $pm/\%$ for TM and TE polarizations. For EG concentration sensitivities, 71 $pm/\%$ and 63 $pm/\%$ are obtained from 5.9-d for TM and TE, respectively. As compared to

38.1 $pm/\%$ (ethanol TM), 32.6 $pm/\%$ (ethanol TE), 60.4 $pm/\%$ (EG TM), and 51.8 $pm/\%$ (EG TE) obtained from the linear fits to the dashed curves, experimental results are in a very good agreement with the analytical calculations. From Figure 5.7, similar concentration sensitivities are obtained (39 $pm/\%$, 33 $pm/\%$, 67 $pm/\%$, and 61 $pm/\%$ for ethanol TM, ethanol TE, EG TM, and EG TE experiments, respectively.)

Finally, hysteresis (Hys) of the OFR sensors is characterized and the results are depicted in Figure 5.10. In Figure 5.10-a and Figure 5.10-c, time traces suggest that the response time and recovery time of OFR sensor are $\sim 1\ min$. By defining Hys similar to the case in Chapter 3, it appears there is a small hysteresis for ethanol (TM average 17%, TE average 15%) and even less hysteresis for EG (TM average 1%, TE average 2%). Ethanol concentration sensitivities are 40 and 34 $pm/\%$, and EG concentration sensitivities are 63 and 56 $pm/\%$ for TM and TE polarizations, respectively. These values are in a good agreement with the analytical calculations obtained from the linear fits to dashed curves between 0% and 20% (34.1, 29.1, 56.3, and 48.0 $pm/\%$ for ethanol TM, ethanol TE, EG TM, and EG TE, respectively).

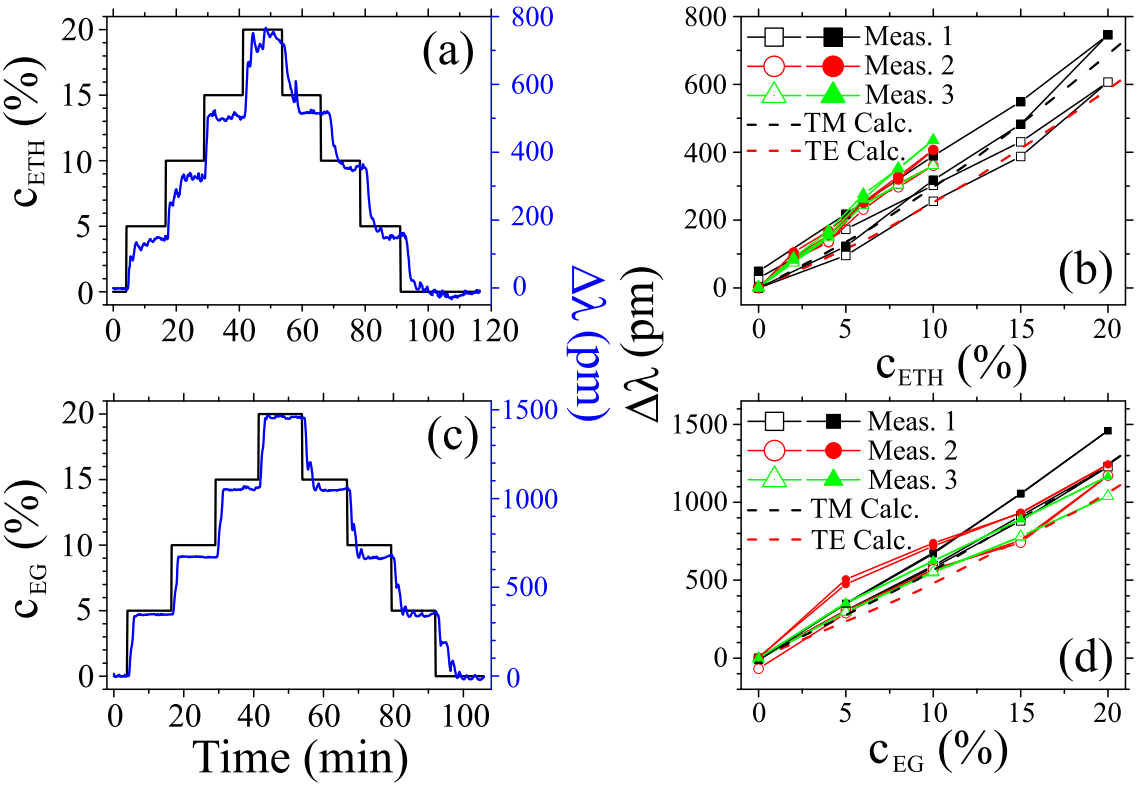

Figure 5.10: Time traces of a) Ethanol and c) EG hysteresis experiments. Respective results are depicted in b) and d), together with the analytical calculations.

Chapter 6

CONTAMINATION DETECTION IN OIL EMULSION MICROSPHERE DROPLETS IN WATER

6.1 Introduction

Up to this point in the thesis, microdisk or microcylinder resonators are investigated. Microdisks are used because of their convenience in UV photolithography fabrication, whereas microcylinders are preferred because they are easily obtained from commercial optical fibers. Microspheres, on the other hand, have other advantages such as high Q-factors [Vahala, 2003]. Also, due to the surface tension, liquids automatically tend to form smooth spherical shapes. Using this idea, there are many methods to produce microspheres for different applications. For instance, a superhydrophobic coating (contact angle $> 150°$) provides a substrate for formation of glycerol-water droplet microsphere resonators [Jonáš et al., 2012]. These microspheres are excited with a tapered fiber and Q-factors around 2×10^6 are observed. A similar idea is holding water droplet microspheres on silica microspheres and exciting their WGMs via a tapered fiber [Hossein-Zadeh and Vahala, 2006]. Another microsphere generation method is exposing the end facets of optical fibers to CO_2 laser [Gardner et al., 2017]. With the power of the laser, the end facet of the fiber melts and reforms into a spherical shape. Lasing is observed from the Rhodamine 610-doped coating on these spheres using the free-space coupling. In [Avino et al., 2014], a liquid sample is suspended from a needle tip to form a droplet resonator. This configuration provides almost spherical shape and supports droplets with diameters up to 1.5 mm.

In the previous chapters, experiments involving sensing based on $\Delta\lambda$ is presented. However, changes in Q-factors of microresonators can also be used as a sensing channel

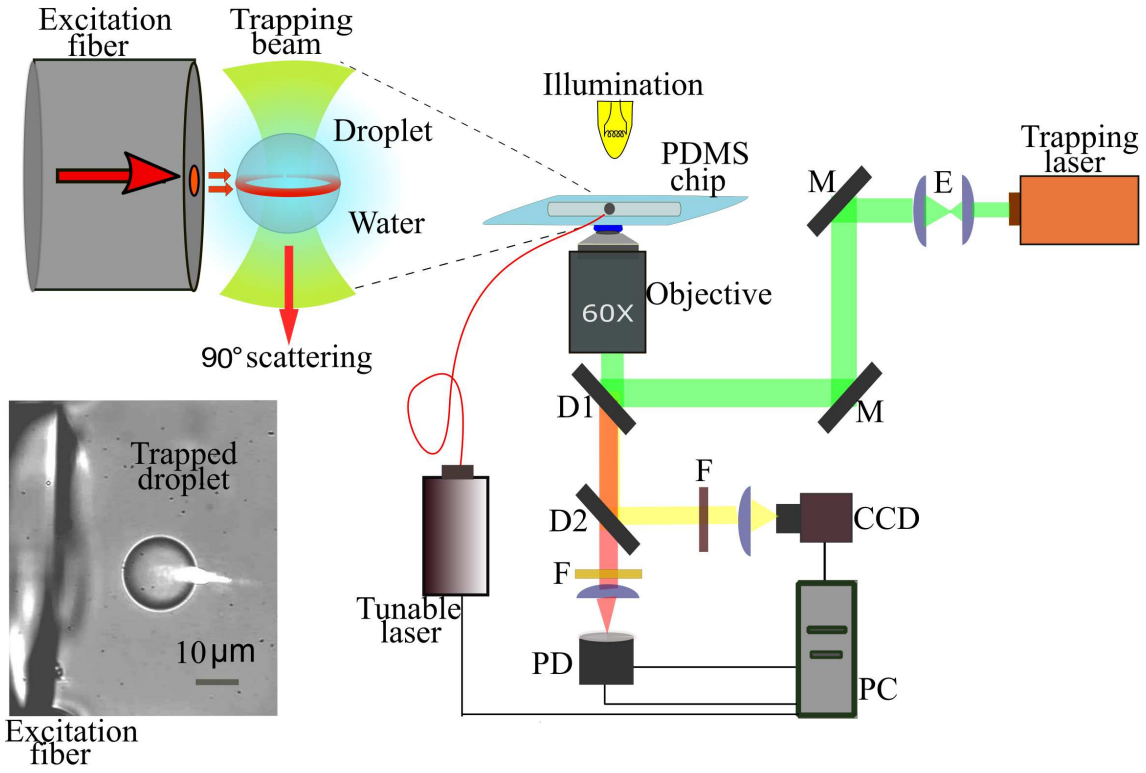

Figure 6.1: Experimental setup used for droplet experiments. PDMS chip involving the microchannel and excitation fiber is held on an inverted microscope. Using one dichroic mirror (D1), trapping laser is reflected and directed onto the droplet whereas the scattered light in the telecom wavelength and the optical image in the visible range are transmitted through. These two are separated using another dichroic mirror (D2). In the inset at the top, a schematic description of the trapped droplet and the excitation fiber is presented. The lower inset is an optical image of the trapped droplet and the scattered light. Red laser through the excitation fiber is used just for imaging purposes. During experiments, tunable telecom light is used through the excitation fiber.

since microspheres support very high Q-factors [Serpengüzel et al., 1995], and they are very sensitive to environmental disturbances [Serpengüzel et al., 1997]. For instance, ΔQ-based detection for heavy water [Armani and Vahala, 2006] or single nanoparticle detection [Shao et al., 2013] applications have been presented. Q-factors can be measured from the full width at half maximum of the WGM resonance via $Q = \frac{\lambda}{\delta\lambda}$ [Armani and Vahala, 2006], or the cavity lifetime of the photon [Armani et al., 2003]. The relation between the FWHM of the WGM ($\delta\nu$) and the cavity lifetime, τ, is given by:

$$\delta\nu = \frac{1}{2\pi\tau}$$

where ν is the resonance frequency of the WGM. This method is also known as the cavity ring-down spectroscopy (CRDS), where high Q-factor resonators are required, but precise measurement of Q is possible. For instance, CRDS has been presented for determining the olive oil-sunflower seed oil composition inside oil droplets [Avino et al., 2014]. Photon cavity lifetimes increase as the olive oil composition increases. Using these lifetimes, therefore, the Q-factors are precisely measured using CRDS and sunflower seed oil contamination inside olive oil microsphere droplets are detected. In addition, using the liquid sample itself as a resonator enhances the interaction between the WGM and the composition of the sample, as opposed to the solid microresonators where the interaction takes place via the evanescent field of the WGM. Although it is claimed that single nanoparticles can also be detected, this configuration requires liquids having a low rate of evaporation [Avino et al., 2014].

In this chapter, two different sets of sensing experiments are presented. The first set involves contamination inside benzyl benzoate (BB) microsphere droplets in water host environment based on $\Delta\lambda$ [Anand et al., 2016]. The second set, on the other hand, is based on ΔQ when sunflower seed oil is added inside olive oil droplets. Depending on the volume fraction of olive oil inside the mixture (η), the Q-factor of the droplet changes. For both sets of experiments, a PDMS microfluidic chip is fabricated for containing the emulsion, since the integration of microresonators and microfluidic channels provides a compact and isolated sensing platform [Levy et al.,

2006, Zhi et al., 2013]. Also, 1% SDS (sodium dodecyl sulfate) is added as a surfactant to reduce the surface tension of the droplets. This allows storage of the droplets free from coalescence. Then the droplets are stably immobilized using optical trapping technique [Benner et al., 1980, Arnold and Folan, 1986], whereas their WGMs are excited simultaneously via free-space coupling (see Figure 6.1).

6.2 Fabrication of PDMS Microfluidic Chips

For fabricating PDMS microfluidic chips, first, a mold is prepared by spin-coating of SU-8 2050 on a Si wafer. The obtained thickness of the mold is $\sim 40\ \mu m$, however, it can be tuned using different spin coating speeds. The SU-8 mold consists of a simple configuration featuring two SU-8 lines perpendicular to each other. One line is designed as the fluidic channel and the other as the channel for the excitation fiber. 1:10 PDMS is then drop-casted on the SU-8 mold and kept under $100°C$ for $\sim$ 2 hours. The thickness of the PDMS is 1 cm to produce stable microfluidic chips featuring leakage-free operation. PDMS is then removed from the Si wafer by manually peeling it off and two holes are punched at the two ends of the fluidic channel using a metal puncher. These holes are intended to provide inlet and outlet for the liquid. A microscope cover glass and the patterned PDMS are exposed to oxygen plasma (50 W, 30 s) for chemical activation of their surfaces, and then their plasma-exposed regions are put onto one another. After a while, PDMS and glass chemically bond together to form the microfluidic chips (see Figure 6.2-a). At this point, physical removal of PDMS from the cover glass is not possible, only they can be separated if the PDMS is torn apart or the cover glass is broken. Excitation fiber is then inserted manually into the fiber channel. Finally, the PDMS chip is put onto the microscope objective for trapping oil emulsion droplets inside water (see Figure 6.2-b).

Although the lengths of the fluidic channel and the fiber channel are in the order of cm, the PDMS layer can be cut such that shorter channels remain in the chip, as long as the connection point of the two channels remains intact. However, for easy

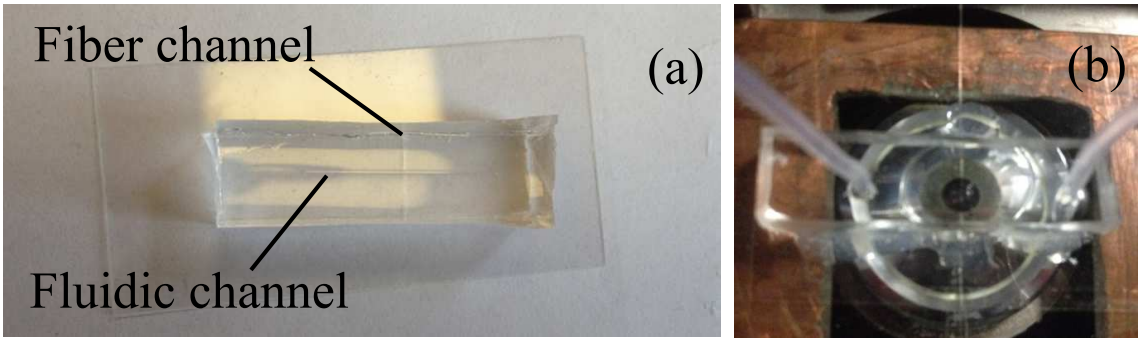

Figure 6.2: a) PDMS microfluidic chip featuring the fluidic and fiber channels used in the droplet experiments. b) Placement of the PDMS chip on the 60x microscope objective. This objective is used for three purposes: for focusing the trapping beam, collecting the scattering spectra from the droplet, and imaging the droplet.

handling and keeping a distance between the inlet and outlet, PDMS chip layer is usually prepared as depicted in Figure 6.2. Widths of the fluidic channel and the fiber channel ranges from 100 to 250 and 120 to 140 μm, respectively. Wider fluidic channels are preferred to avoid sticking of the droplets on the walls of the microfluidic chip. For fiber channels, usually, widths of 125 and 130 μm are more useful since the excitation fiber diameter is 125 μm. If the fiber channel is too narrow, it is not possible to insert the excitation fiber without breaking the fiber. On the other hand, if the fiber channel is too wide, then fluid flow towards the fiber channel is inevitable and positions of the droplets could not be stabilized.

6.3 Free-Space Excitation of Optically Trapped Oil Emulsion Droplets

For trapping the oil emulsion droplets inside water, a ytterbium fiber laser is used (YLM-10-LP-SC, IPG Photonics. Wavelength: 1070 nm, maximum power: 10 W, continuous wave operation). Trapping power in the range of $200 - 300$ mW is used, as described by [Ashkin and Dziedzic, 1981]. Trapping beam is focused by a 60x microscope objective on the oil droplet observed using a CCD camera. First, using a 3D translation stage, the droplet is coarsely brought in front of the core of the single mode excitation fiber. The position of the oil droplet is then fine-tuned using

a 3D piezo translation stage independent from the 3D stage used for coarse position arrangement. At this point, a red laser of wavelength 638 nm is used for excitation such that maximum scattering is observed through the 60x microscope objective from the CCD camera, as depicted in the lower-left inset of Figure 6.1. After optimizing the position of the droplet, excitation laser is changed from red laser to Santec laser (Santec TSL-510-C, tunability range: 1500 nm - 1630 nm, wavelength resolution: 1 pm) for tunable operation. Using the same 60x microscope objective, the scattering spectrum is collected. Different from the other chapters where transmission dips are featured, scattering peaks are analyzed to find the spectral positions, Q-factors, and FSR of the WGMs.

The idea of optical trapping relies on the change in the momentum of the photons inside the trapping beam. As the photons in the trapping beam propagate through the droplet, they change direction due to refraction. Collective change in the momentum reveals a net force acting on the droplet towards the focal point. Although the droplet is pushed away from the focal point because of the back-reflected photons, this effect is smaller as compared to the force pulling the droplet towards the focal point. Therefore, focusing a beam of light provides a stable trapping for the droplet and small fluctuations in the position of the droplet are counter-acted by the force acting on the droplet by the trapping beam. If the relative refractive index is high, and the density contrast is low between the host liquid and the droplet, then the trapping becomes more stable. Therefore it is quite a good choice to take water (density= 1.00 g/cm^3, $N = 1.334$ at $\lambda = 589\,nm$) as the host liquid and BB (density= 1.11 g/cm^3, $N = 1.568$ at $\lambda = 589\ nm$) as the droplet. After trapping and excitation of WGMs of oil droplets in water, fluctuations in the BB droplet WGM spectra are presented as a proof of concept for diffusion of small particles in and out of the droplet. Olive oil and sunflower seed oil are also good choices for water host medium, but with a smaller relative refractive index. (Sunflower seed oil density= 0.91 g/cm^3, $N = 1.476$ and olive oil density= 0.914 g/cm^3, $N = 1.467$ at $\lambda = 589\ nm$). The absorption coefficient of sunflower seed oil is higher than the absorption coefficient of olive oil

$\lambda = 1565 - 1590\ nm$. Specifically for instance, at $\lambda = 1570\ nm$, sunflower seed oil and olive oil have α values of 6.8 m^{-1} and 6.2 m^{-1}, respectively. Therefore sunflower seed oil droplets are expected to have lower Q-factors than olive oil droplets. η, volume fraction of olive oil, therefore, can be measured from the Q-factor of the mixture droplet.

6.4 Contamination Detection Results

For obtaining the WGMs of oil emulsion droplets in water, scattering spectra are analyzed [Chen et al., 1993]. Using BB droplets, the effect of randomly diffusing small particles are investigated from the $\Delta\lambda$ of the WGM spectrum. In Figure 6.3, 5 consecutive spectra of $a = 22\ \mu m$ BB droplet is depicted. There is $\sim 10\ s$ time interval between each consecutive spectra. To distinguish between spectra, a certain amount of offset is given to each spectrum, depending on how much later time they are recorded. Therefore time flows from bottom to top. Two WGMs are observed between $\lambda = 1560 - 1590\ nm$ with an FSR of $\sim 12\ nm$. Using the FSR formula for spherical resonator (Equation 1.2) with $\lambda = 1582\ nm$, $N_{in} = 1.568$, $N_{out} = 1.334$, and $a = 22\ \mu m$, calculated FSR becomes 12.158 nm. This is a very good agreement between the calculated and measured values. WGM around 1580 nm is more prominent than the one around 1570 nm. Therefore in the inset of Figure 6.3, a temporal change in the spectral position of the WGM around 1580 nm is given as a color plot consisting of 18 consecutive spectra. The WGM does not stay in a constant spectral position, rather it moves back and forth with the passage of time. This fluctuation is attributed to randomly diffusing small particles in and out of the microsphere resonator. This measurement provides a proof of concept for detection of small particles inside a liquid sample using oil emulsion droplets.

In addition to the WGM peaks, there are less intense ripples having smaller FSR. Using the FSR formula for a Fabry-Pérot resonator (Equation 1.1) with $FSR = 1\ nm$, $\lambda = 1570\ nm$, and $N = 1.46$, the thickness of the glass d is calculated to be 0.844 mm, which is in the order of optical components used in the experiments. Therefore these

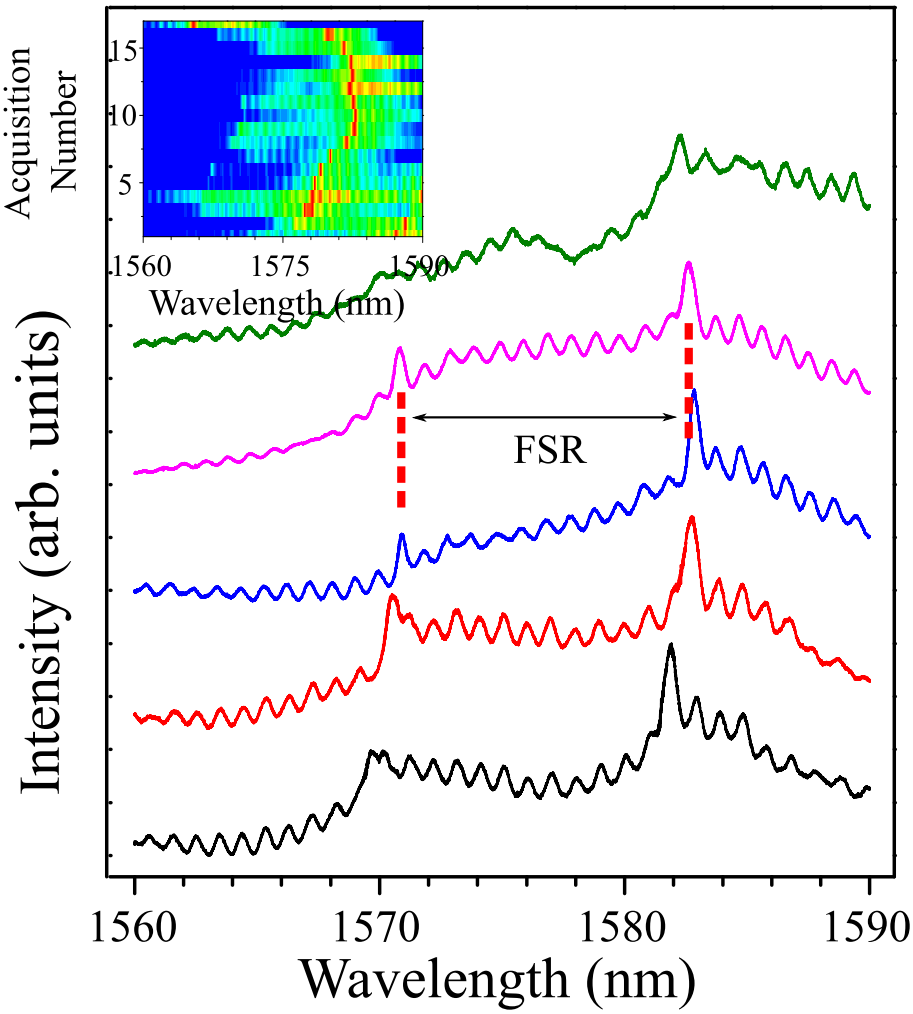

Figure 6.3: Consecutive WGM scattering spectra for a BB emulsion droplet inside water. Between each spectrum, there is a time delay of $\sim 10\ s$. FSR is $\sim 12\ nm$, in agreement with the calculation. Ripples with smaller intensity are due to Fabry-Pérot-like interference because of optical components in the experimental setup. The inset shows a color plot of the WGM around 1580 nm in a wider time window, where red (blue) means higher (lower) intensity. Clear back and forth fluctuation of the spectral position of the WGM is an indication of diffusion of small particles in and out of the BB droplet.

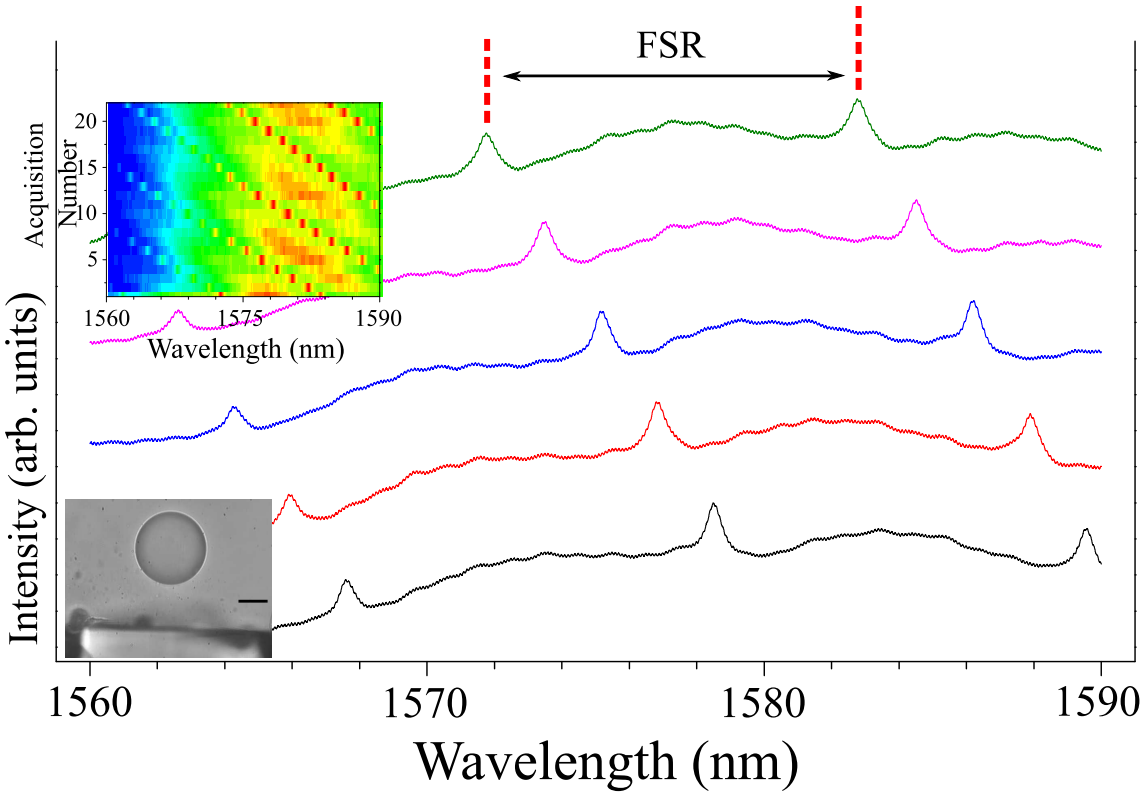

Figure 6.4: WGM spectra of a BB droplet in an unsaturated water host medium. The droplet dissolution results in a constant blue-shift in the WGM spectra, also slowly increasing the FSR. (FSR = 10.83 nm in the first spectrum, increases to 10.92 nm in the fifth spectrum). There is a ~ 10 s time delay between each consecutive spectra. In the color plot inset, the blue-shift is clearly visible. Again, red is higher intensity and blue is lower intensity. In a matter of < 25 scans, WGM positions shifts about three times the FSR. In the other inset, trapped BB droplet is depicted with a scale bar of 20 μm.

ripples are attributed to the Fabry-Pérot-like interferences originating from the optical components used in the experiment.

If the water host medium is not saturated with oil, then droplet dissolves in water and its size decreases. Therefore, WGM spectrum blue-shifts because of the Δa effect (see Figure 6.4) [Kiraz et al., 2006]. To eliminate any change in WGM spectrum because of Δa, water host medium is saturated with oil to achieve no dissolution of the droplets. On the other hand, blue-shifting can be considered a proof of sensing concept based on size change.

η-dependent Q-factor of the sunflower seed oil-olive oil mixture droplets are analyzed from ΔQ measured from the WGM spectrum (see Figure 6.5). Because of higher absorption of sunflower seed oil between $\lambda = 1560 - 1590\ nm$ (see the inset of Figure 6.5), sunflower seed oil droplets exhibit less Q_{mat} than olive oil droplets. This can be attributed to different levels of saturated fats in sunflower seed oil and olive oil. Sunflower seed oil used in the experiment has 14% saturated, 34% monounsaturated and 52% polyunsaturated fats, whereas for olive oil used in the experiments, these fractions are 16%, 73%, and 11% for saturated, monounsaturated and polyunsaturated fats, respectively. Q_{mat} is calculated at $\lambda = 1570\ nm$ for sunflower seed oil and olive oil droplets using the following parameters: Sunflower seed oil; $N = 1.476$, $\alpha = 6.8\ m^{-1}$ and olive oil; $N = 1.467$, $\alpha = 6.2\ m^{-1}$. Calculated Q_{mat} values are 8.69×10^5 and 9.47×10^5 for sunflower seed oil and olive oil, respectively.

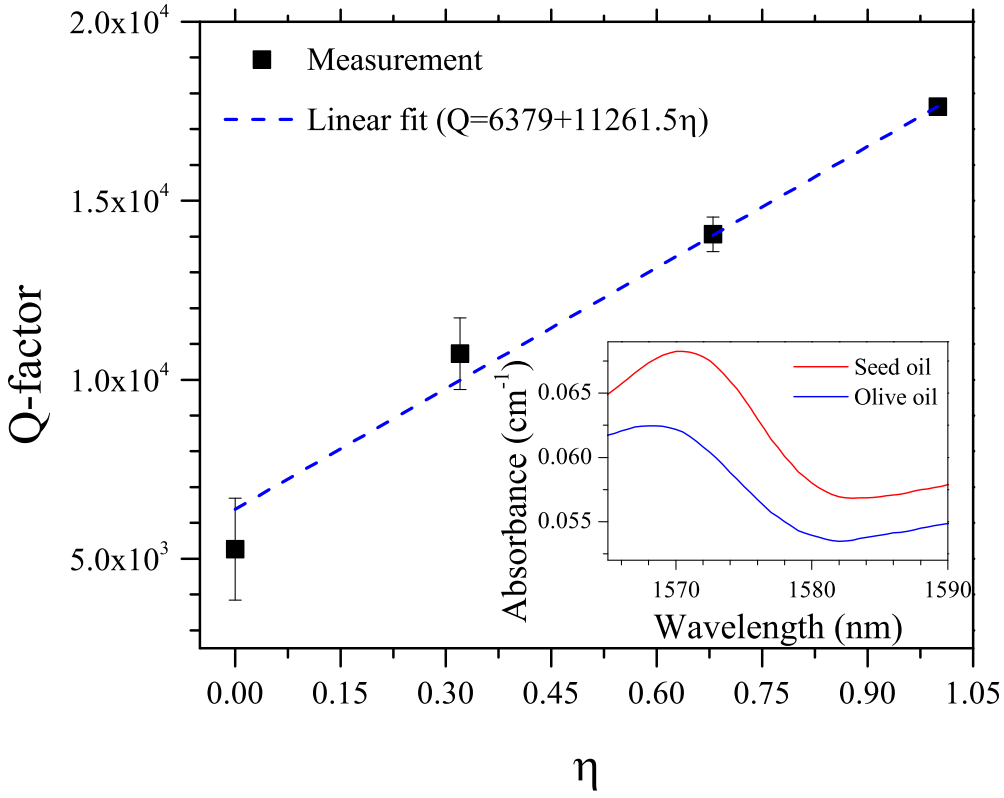

Figure 6.5: Measured Q-factor as a function of volume fraction of olive oil, η, inside the mixture droplet. The expected linear trend is observed and a linear fit is provided. Based on the fit, pure sunflower seed oil has a Q-factor of $\sim$ 6400 whereas, for pure olive oil, it is $\sim$ 17500. In the inset, absorption measurement from pure sunflower seed oil and pure olive oil are provided. Sunflower seed oil absorption is more, therefore the Q-factor for sunflower seed oil is less as compared to the olive oil.

Chapter 7

HYDROGEN GAS SENSING WITH PALLADIUM AND POLYMER-COATED OPTICAL FIBER RESONATORS

7.1 Introduction

Recently, there have been many developments in the optical fiber sensors resulting in the publication of optical fiber sensor reviews once in a couple of years [Udd, 1995, Leung et al., 2007, Lee et al., 2009, Annamdas, 2011, Bogue, 2011, Ramakrishnan et al., 2016, Jin and Granville, 2016, Schenato, 2017, Zhang et al., 2017]. Applications ranging from biosensing [Velasco-Garcia, 2009] to civil engineering [Leung et al., 2015], wall pressure sensing [Manzo and Ioppolo, 2015] to equipment characterization in LHC [Chiuchiolo et al., 2017] have been presented. Chemical and gas sensing occupy an important fraction among these diverge topics [Lee, 2003].

In Chapter 5, detection of liquid refractive index based on OFRs is presented [Eryürek et al., 2017a] and the applications are reviewed. Having a sensitive detection using a simple configuration featuring an uncoated OFR paves the way for much more sensitive detection applications if the OFR is coated with an active layer. In the literature, there have been several studies where an active coating is used together with optical fiber sensors. For instance, the end face of a fiber is coated with P4VP polymer for nitrobenzene detection [Bae et al., 2013]. Sensing mechanism relies on the expansion of P4VP polymer layer. The polymer coating has a certain thickness that reflects only the wavelengths that satisfy the constructive interference condition. These wavelengths shift when the thickness of the polymer layer is increased in the presence of nitrobenzene. With this method, nitrobenzene down to 10 ppm is successfully detected. For humidity sensing application, the end face of an SMF (single

mode fiber)-HCF (hollow-core fiber) structure is coated with polyimide film [Bian et al., 2018]. Due to the interference of the reflected beams, transmission dips are observed. These dips blue-shift as the RH increases. For instance, ~ 25 μm-thick polyimide film provides ~ 1 $nm/\%$ RH with a quick response of 4 s. There is a trade-off between the Q-factor and the sensitivity. As the thickness of the polyimide film increases, Q-factor decreases whereas humidity sensitivity increases. An SMF-NCF (no-core fiber)-SMF-ultra-abrupt taper region-SMF structure is employed for temperature sensing [Bhardwaj et al., 2016]. When the SMF in the middle is coated with temperature-sensitive silicone rubber, sensitivity increases up to ~ 255 $pm/^{\circ}C$ as compared to ~ 120 $pm/^{\circ}C$, the sensitivity of the uncoated device. The mechanism takes advantage of the thermo-optic effect and thermal expansion effect. Contribution to sensitivity coming from thermo-optic effect is obtained by taking a measurement from the uncoated device. Extra contribution to the sensitivity in the case of the coated device comes from the thermal expansion effect due to the existence of the coating. Finally, a hydrogen sensor based on an SMF-NCF-SMF structure in which a Pd/WO_3 coating is employed on the NCF region is presented [Shao et al., 2017]. NCF region forces the light to propagate more in the outer edges of the fiber to ensure the maximum interaction with the Pd/WO_3 coating. Due to the refractive index change of the coating, blue-shift is observed with a sensitivity of 1.27 $nm/\%$ H_2.

In order to take advantage of the expansion-based hydrogen sensing, Pd can be employed, as described in Chapter 4. Combining these ideas presented in Chapters 4 and 5, coating OFRs with Pd provides a hydrogen gas detection platform with a high sensitivity. Due to the fact that light cannot propagate in the Pd layer, a second layer is required as a propagation medium. Therefore a hydrogen-permeable and elastic PDMS-urea polymer layer is coated on top of the Pd. PDMS-urea polymers have a high permeability to gases and they can provide strong hydrogen bonding [Sami et al., 2014]. With the help of both Pd and polymer layers, it is intended to take advantage of both Δa and $\Delta\lambda$ effects. Therefore, in this chapter, PDMS-urea polymer and Pd-coated OFR sensor is employed as a hydrogen gas sensor.

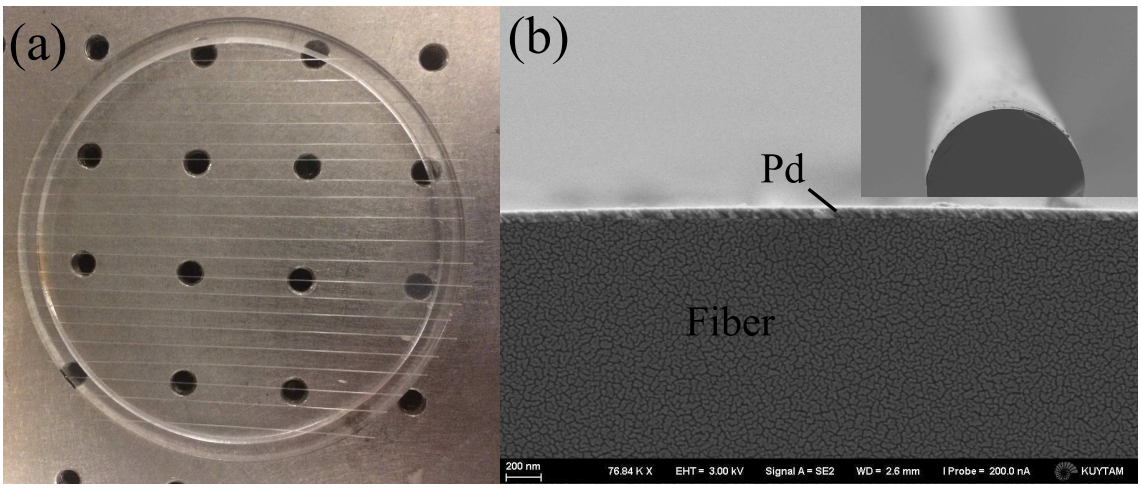

Figure 7.1: a) OFRs prepared for sputtering in a grill configuration for two-sided coating of Pd. b) SEM image of the OFR after Pd coating. OFRs are cut in the perpendicular direction to the fiber axis and SEM image is taken from the cut cross section, as depicted in the inset.

7.2 Preparation of the Sensors

Polymer and Pd-coated OFRs are obtained as follows. Firstly, optical fibers are mechanically stripped from their polymer coatings and cleaned with IPA. Secondly, these OFRs are placed in between two ring-shaped holders. Both the rings and the OFRs are fixed with epoxy glue. This configuration allows sputtering of Pd on both sides of the OFRs, as in the case of a grill (see Figure 7.1-a). Once one side is coated, the samples are turned upside down so that the other side of the OFRs can also be coated. Obtained Pd thicknesses vary between 50-100 nm (see Figure 7.1-b). Uniformity of the Pd thickness is not a big issue since the variations are $\sim 10\ nm$, insignificant next to $\sim 10\ \mu m$, the designed thickness of PDMS-urea. The thickness is chosen to be around $\sim 10\ \mu m$ because if the thickness is small, such as $\sim 1\ \mu m$, then underlying Pd layer becomes too close to the propagation medium. This results in very low Q-factors and WGMs cannot be observed. On the other hand, if the PDMS-urea thickness is too much, the effect of the expansion of Pd cannot be perceived because the polymer layer would be huge as compared to the Pd. Therefore, it is best

to employ PDMS-urea such that it is thick enough for the WGM to avoid Pd, but thin enough for the expansion to reveal a measurable effect.

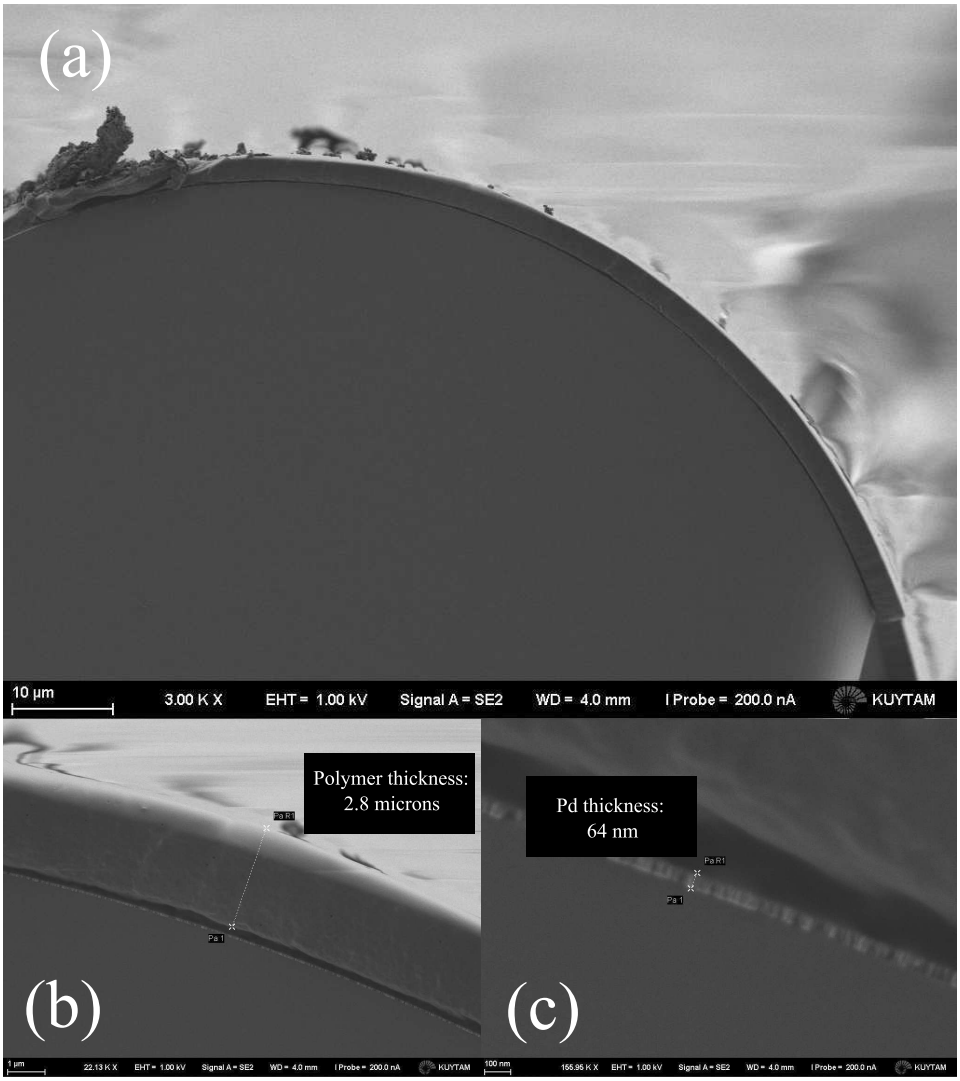

Figure 7.2: SEM images of the cross-section of the sensor. a) A wide view. b) A zoom to the wide view on the PDMS-urea coating. The coating thickness for this particular sample is measured as $\sim 2.8\ \mu m$. c) Even a deeper zoom that focuses on the Pd coating. Pd thickness is measured as $\sim 64\ nm$.

In the third step of sensor preparation, Pd-coated OFRs are dip-coated with PDMS-urea polymer (see Figure 7.2). The preparation of PDMS-urea polymer is as follows [Yilgor et al., 1984]: 1 mmol PDMS with average molecular weight 3200 g/mol

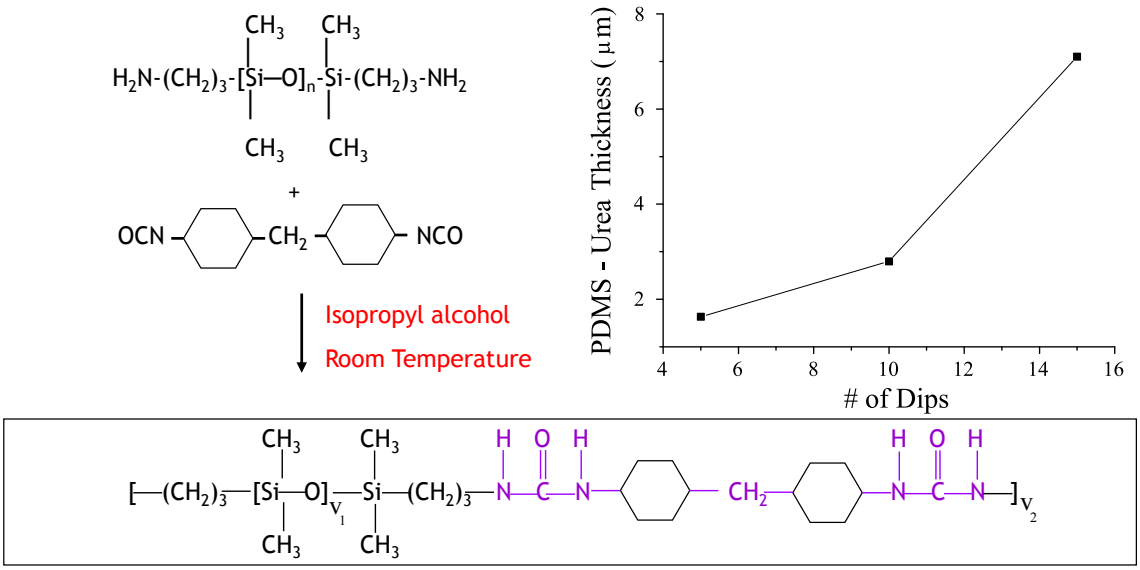

Figure 7.3: Schematic representation of PDMS-urea preparation. As the inset shows, PDMS-urea thickness increases with increasing number of dips.

is prepared with amine groups. Then 25% PDMS+IPA solution is produced. In another container, 1 mmol of isocyanate with molecular weight 262.35 g/mol is dissolved in IPA such that 25% solution is obtained. Using a liquid dropper burette, PDMS solution is dropped slowly inside the isocyanate solution and mixed at room temperature. Ultimately, when PDMS-urea structure is obtained (see Figure 7.3), values of v_1 and v_2 are 40 and 10, respectively. These values provide an average molecular weight of 35000 g/mol.

After these steps, 15:85 PDMS-urea:THF (mass ratio) solution is prepared for dip coating. The dip coating process is carried out using an automated dip coater machine with a dipping velocity of 100 mm/s. The thickness of the PDMS-urea coating is measured from the cross-section of the OFR under the SEM, as seen in Figure 7.2. Depending on the number of dips, the thickness of the PDMS-urea increases (see the inset of Figure 7.3) Finally, PDMS-urea and Pd-coated OFRs are baked under 80°C temperature for at least 2 hours. The final baking step allows a reflow over the PDMS-urea surface to minimize the surface scattering losses, i.e., Q_{ss} increases (see Figure 7.4). This is a crucial step since WGMs could not be observed unless the

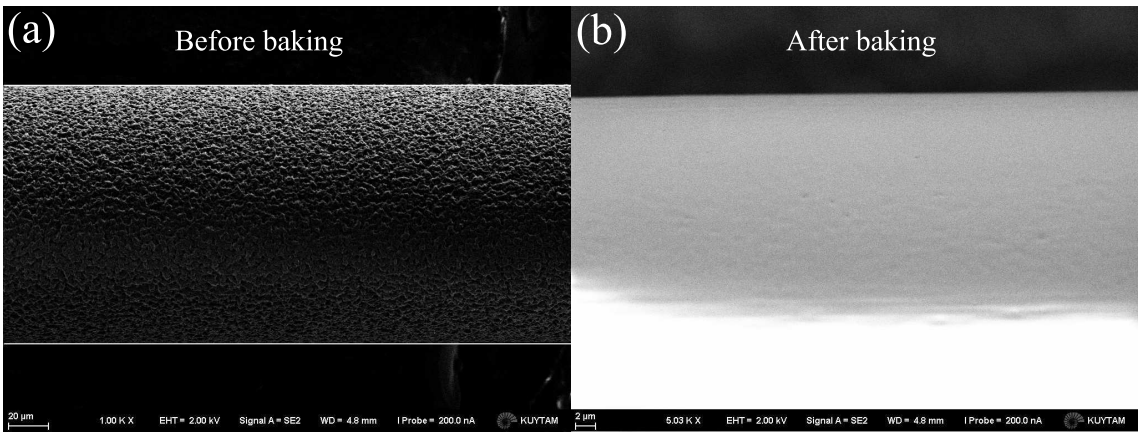

Figure 7.4: SEM images of dip coated OFR a) before and b) after baking. Improvement towards achieving smooth surfaces with baking is clearly visible.

samples are baked.

7.3 Hydrogen Gas Sensing Measurements

Hydrogen gas sensing measurements are performed using the experimental setup presented in Chapter 4 (see Figure 7.5). Pure nitrogen and pure hydrogen gases are mixed at certain flow rates to control the hydrogen concentration in the gas chamber. At first, with the equipment at hand, hydrogen concentrations as low as 0.3% (3000 *ppm*) could be achieved. Measurements down to 0.3% (3000 *ppm*) are carried out using pure nitrogen and hydrogen gases. Since PDMS-urea and Pd-coated OFR sensors provide a high sensitivity, lower hydrogen concentrations can be tested. For this reason, pure hydrogen gas is replaced with a 1% hydrogen-nitrogen mixture gas to obtain lower hydrogen concentrations.

Hydrogen gas measurements are performed in the staircase manner and the on-off. In some cases, there is a collective constant drift to the blue side of the spectrum, which can be attributed to the insufficient removal of the humidity from the PDMS-urea. If that is the case, an overall linear correction is applied to the time trace (see Figure 7.6). To determine the correction, a linear fit is applied to the data points where c_{HYD} is expected to be 0 [Eryürek et al., 2015]. In the case of Figure 7.6-a

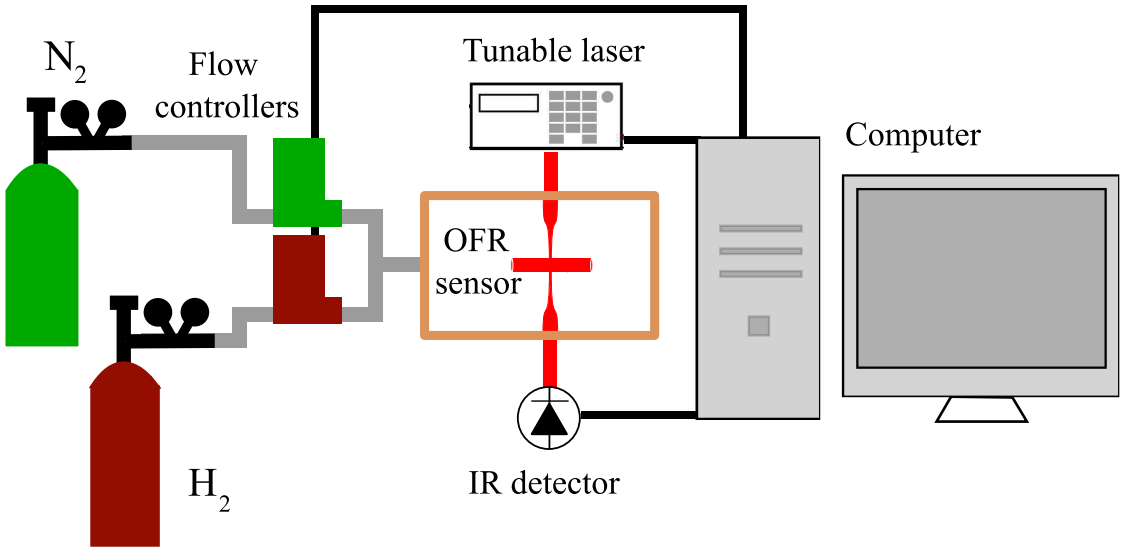

Figure 7.5: Experimental setup for hydrogen gas detection using Pd and polymer-coated OFR. The sensor is exposed to dilute hydrogen gas concentrations. In the meanwhile, tunable laser light is coupled to the OFR through the tapered fiber. Collected transmission spectra are analyzed using a computer. Hydrogen concentrations are adjusted using computer-controlled flow controllers. In the figure, green gas cylinder and the flow controller are associated with the nitrogen gas, whereas the brown ones are with the hydrogen gas.

for instance, a linear fit is applied to the first and last parts of $\Delta\lambda$ where $c_{HYD} = 0$. The linear fit comes out to have a slope of -1.51526 and an intercept of 8.98045. This correction results in a more reasonable time trace as depicted in Figure 7.6-b. In very rare occasions, fourth order polynomial fit gives a better correction than the linear fit. This is probably due to the fact that the measurement is started so early without the removal of humidity that it resulted in a large blue shift in the beginning of the measurement as compared to the middle or end of the measurement.

Response and recovery time of the sensor is also investigated using the time trace of an on-off measurement (see Figure 7.7). For response time, the convention of calculation involves the time difference between two events. The first event is the time that c_{HYD} is changed from 0% to the desired value. And the second event is the point when resonance shift reaches 90% of the $\Delta\lambda$ value associated with the given

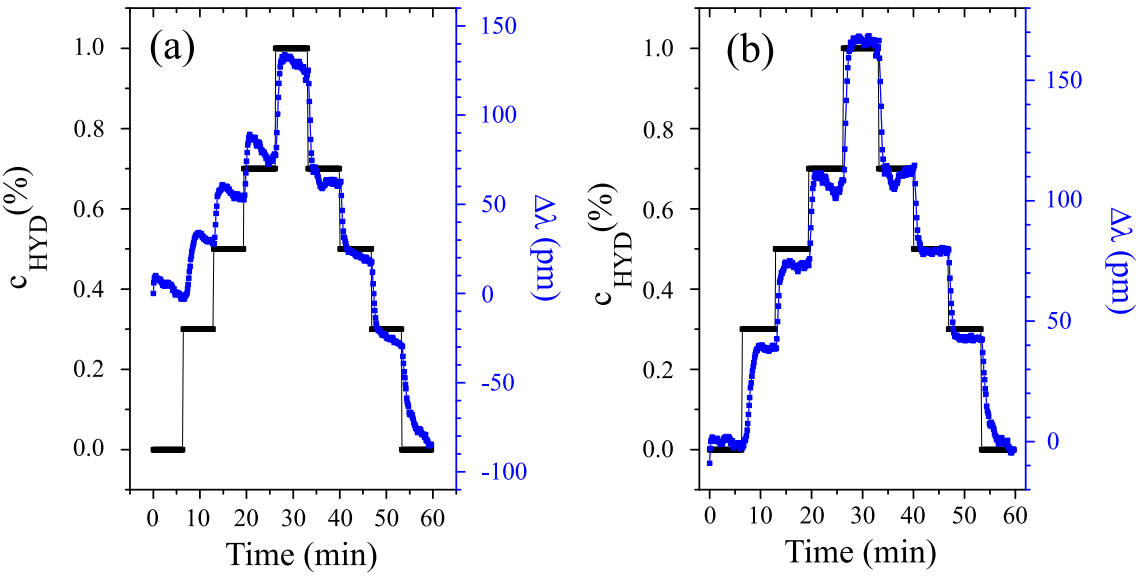

Figure 7.6: a) An exemplary hydrogen gas measurement featuring a constant drift to blue side of the spectrum. b) Measurement becomes better after a correction calculated from a linear fit to the $\Delta\lambda$ values where $c_{HYD} = 0$. Equation of the subtracted fit is $-1.51526 \times$ (Time in minutes) + 8.98045

c_{HYD}. Calculation convention for the recovery time also similarly has two events. The first event is the point when c_{HYD} is changed to 0%, and the second event is when the resonance shift decreases down to 10% of the initial $\Delta\lambda$ associated with the c_{HYD}. Response time decreases as c_{HYD} increases up to 1% and then seems to be constant around 70-80 s. This behavior can be attributed to the fact that hydrogen gas can slowly present an effect when c_{HYD} is small, whereas as c_{HYD} increases, the response time reaches a saturation. Recovery time, on the other hand, is more or less constant at around 80 s over all the investigated c_{HYD} region. Since the removal of the hydrogen gas is achieved using a constant flow of nitrogen gas, recovery time remains more or less constant.

In Figure 7.8, 10 measurements of hydrogen gas are summarized. In parts Figure 7.8-a and b, on-off manner and staircase manner experiments are presented, respectively. Most of the results agree with each other and have $170 - 200\ pm/\%\ H_2$. There are two exceptions (Measurements 6 and 10) where the sensitivity decreases down to

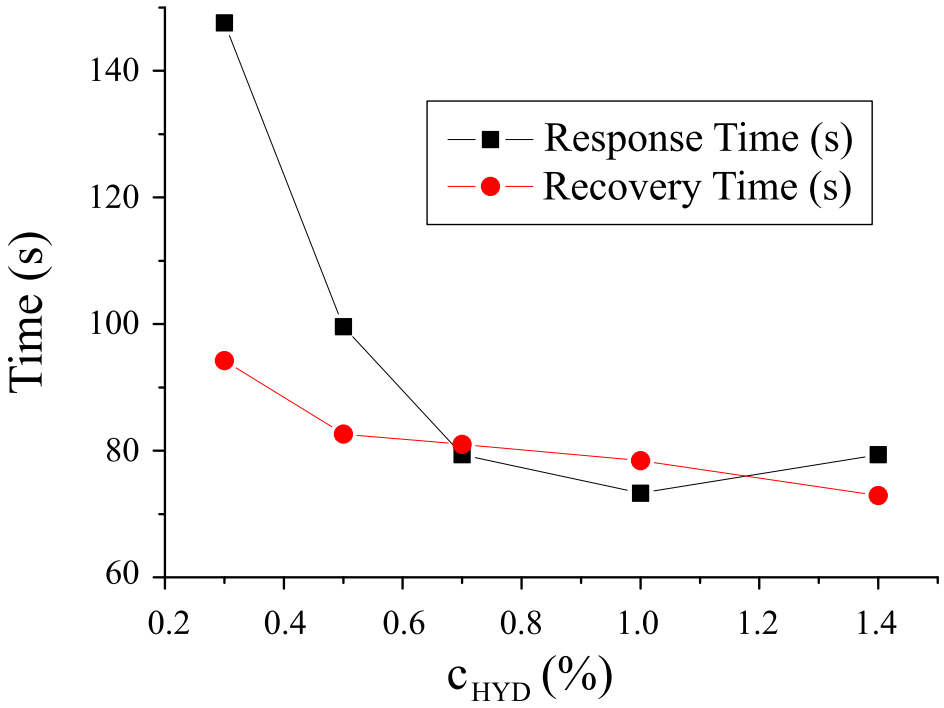

Figure 7.7: Response and recovery times of the sensor. The response of the sensor becomes quicker as c_{HYD} increases up to 1%. Then remains constant around 80 s. Recovery time is constant around 80 s over a larger c_{HYD} region.

$\sim 80\ pm/\%\ H_2$. This may be caused by tapered fiber coinciding with a thicker portion of PDMS-urea. Although the expansion of Pd may be the same, with a thicker PDMS-urea layer, Δa would be smaller. Ultimately, this results in a less sensitive sensor. On the other hand, the Pd layer may be thin at the point of excitation where the tapered fiber is touching to the sensor. Again, sensitivity decreases as a result of smaller Δa.

In Figure 7.8-a, the average sensitivity is 170 $pm/\%\ H_2$, and it becomes 186 $pm/\%\ H_2$ when Measurement 6 is excluded. The highest sensitivity slope is 202 $pm/\%\ H_2$ which is obtained from Measurement 3. From Figure 7.8-b, hysteresis (Hys) is calculated by using the following formula (similar to Hys defined in Chapter 3).

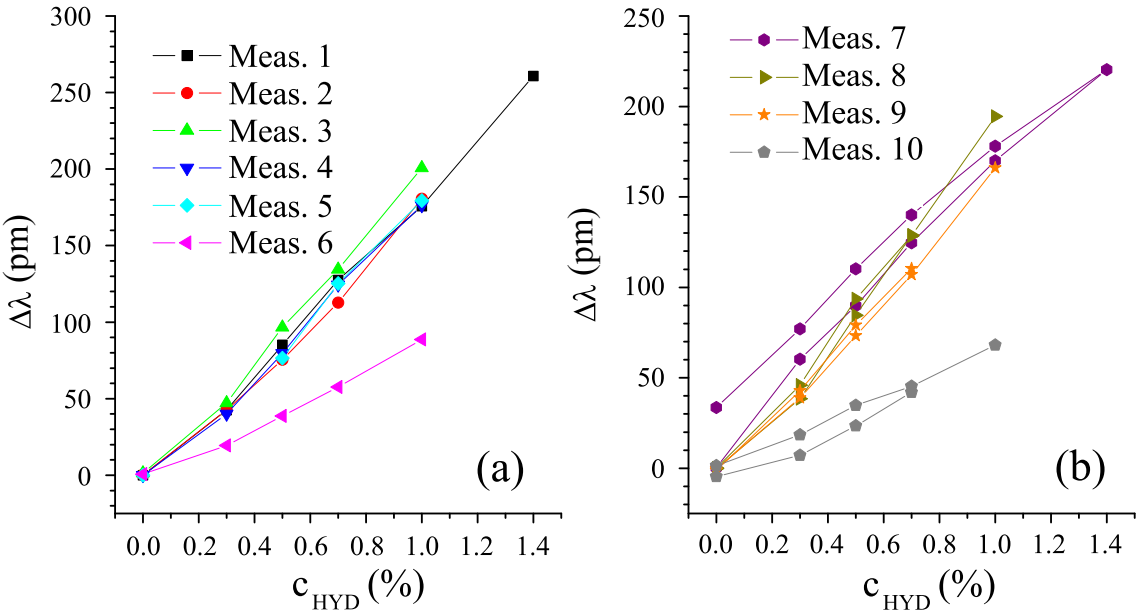

Figure 7.8: Summary of the hydrogen sensing measurements for a) On-off manner measurements and b) Staircase manner measurements.

$$Hys = |\frac{\Delta\lambda_{dehyd} - \Delta\lambda_{hyd}}{\Delta\lambda_{hyd}}|$$

where $\Delta\lambda_{hyd}$ and $\Delta\lambda_{dehyd}$ are resonance shifts during hydrogenation and dehydrogenation. Absolute value is put because the sign of $\Delta\lambda_{dehyd} - \Delta\lambda_{hyd}$ changes from measurement to measurement. From four staircase measurements, average Hys is calculated as 14.5%. Hys in Measurement 9 is calculated as 7%, which is the smallest among all.

PDMS-urea and Pd-coated OFR sensor is also exposed to a low concentration of hydrogen gas (Measurement 11). Measurement result from such an experiment is given in Figure 7.9. Although it is ideally possible to detect ~ 75 *ppm* H_2 (see the sensitivity slope in Figure 7.8), demonstrated lower detection limit is 1000 ppm. This can be attributed to different thicknesses of PDMS-urea and Pd layers. As the Pd thickness increases or PDMS-urea thickness decreases (polymer thickness should not be too small for the WGMs not to propagate due to Pd), the sensitivity is expected

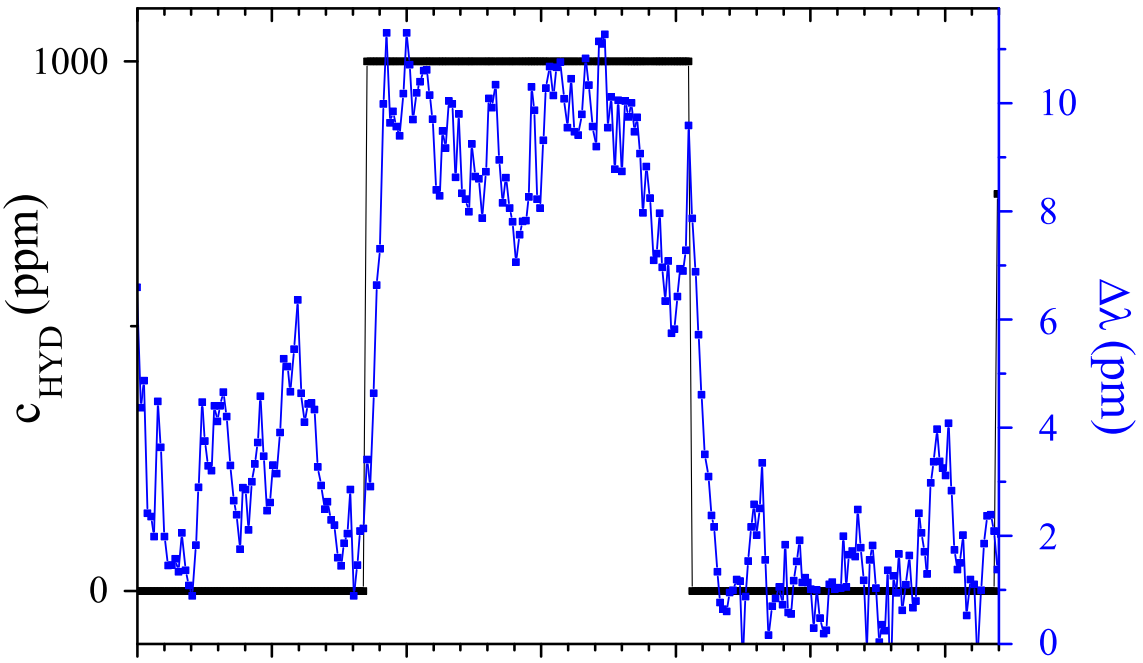

Figure 7.9: An exemplary measurement when $c_{HYD} = 1000\ ppm = 0.1\%$

to increase. Therefore, it is possible that Measurements 1-5 and 7-9 are taken from sensitive samples whereas Measurement 11 is taken from a rather less sensitive sample. It is crucial to investigate optimum sensor parameters to obtain the most sensitive operation. Therefore, it is safe to state that detection of 75 *ppm* H_2 is quite possible provided that optimum sensor parameters are employed. After characterization and optimization of the parameters, it will be possible to detect when $c_{HYD} < 100\ ppm$.

Sensing mechanism of the Pd and polymer-coated OFR sensor is not fully explained yet. With the help of Pd, Δa effect is intended. Since OFRs are coated with Pd rings (instead of Pd disks as in Chapter 4), amount of expansion is proportional to the Pd thickness, h, which is $\sim 100\ nm$. It is known that for 1% H_2, $\Delta a/h = 0.087\%$ [Noh et al., 2011]. Assuming a 7 μm-thick polymer coating on the OFR, $\Delta a/a = 1.25 \times 10^{-6}$. However, maximum $\Delta\lambda/\lambda$ is achieved to be 1.3×10^{-4}, which means the ΔN is the dominant effect. However, as depicted in Figures 7.10, and 7.11, presence of Pd makes a huge difference, indicating an effect coming from Pd. Since it cannot be the expansion of Pd, there must be another reason giving rise

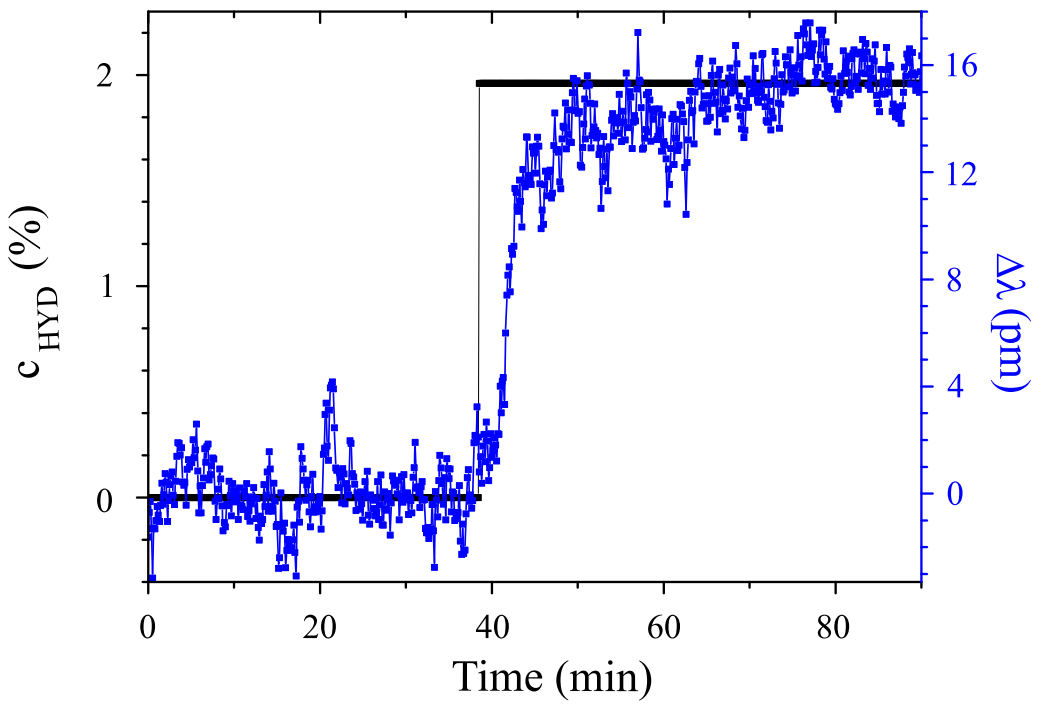

Figure 7.10: Response of only PDMS-urea coated OFR to hydrogen gas. ΔN effect is present, which is significantly less than Δa effect obtained with the PDMS-urea and Pd-coated OFR.

to sensitive detection. It is probable that, when there is Pd, it acts as a catalyst for hydrogen, transforming it to a more detectable form. Then this form of hydrogen may be having a strong interaction with the polymer, providing higher $\Delta N/N$ or $\Delta a/a$, which is not possible in the absence of Pd. In order to resolve this issue, different control experiments could be performed. For instance, instead of Pd, another metal which has little interaction with hydrogen could be used, such as aluminum. Moreover, while the Pd thickness is constant, polymer thickness could be changed to investigate the effect of expansion, since thicker polymers are expected to be more insensitive. Finally, another polymer (such as PMMA) can be employed to observe the effect of the polymer. For all these experiments, SEM imaging and IR analysis can be helpful towards explaining the interactions.

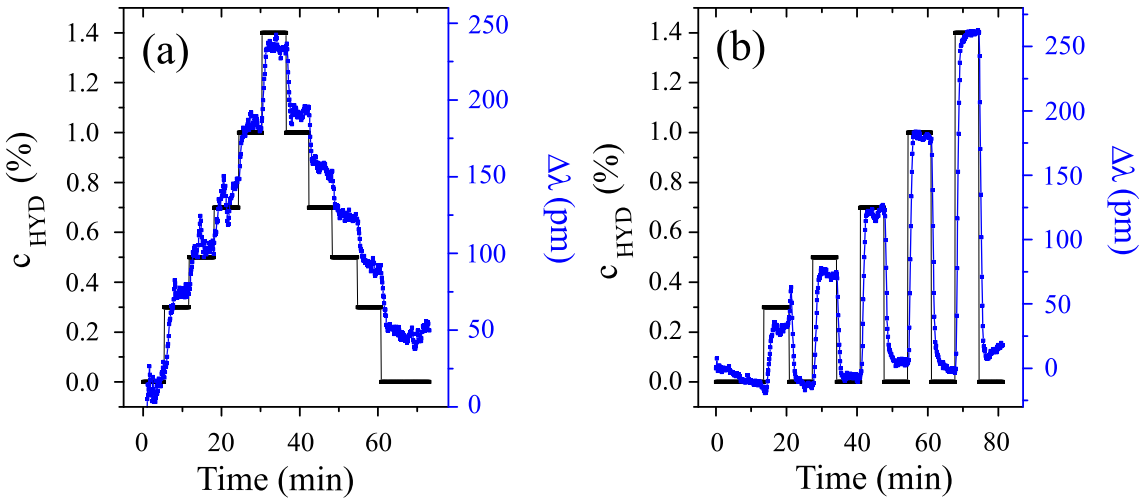

Figure 7.11: a) Staircase manner and b) On-off manner hydrogen detection results using Pd and polymer-coated OFR.

Chapter 8

CONCLUSIONS AND OUTLOOK

In this thesis, optical detection using several fluids is presented, and the underlying sensing mechanisms are described. In Chapter 1, a general introduction is given and optical microresonator-based sensing is reviewed. In Chapter 2, WGMs are discussed for spherical and cylindrical geometries, and resonance conditions for these WGMs are analytically described. As repeatable and stable humidity sensors, SU-8 microdisk resonators are employed and presented in Chapter 3. Even at 1% relative humidity (RH), the signal to noise ratio is around 50, meaning the sensor has a high potential for sensitive operation. Using only one-step photolithography, SU-8 microdisks are fabricated along with the SU-8 waveguides, that are used for excitation of WGMs. The sensing mechanism relies on the refractive index change of the SU-8 microdisk resonator. Coating of these SU-8 microdisk resonators with Pd allows detection of hydrogen gas. In Chapter 4, Pd-coated SU-8 microdisk resonators are described. Minimum hydrogen concentration measured is 0.3%, which is more than an order of magnitude smaller than 4%, the flammability limit of hydrogen gas. In this case, the sensing relies on the expansion of the SU-8 microdisk layer as a result of the expansion of Pd in the presence of hydrogen gas. In Chapter 5, change in the refractive index of a liquid environment is discussed. The sensing mechanism is based on the change in the refractive index of the environment. Although only a small portion of the WGM (evanescent tail) propagates in the environment, the lower detection limit is obtained to be 2.7×10^{-5} RIU, which is comparable with the reported values in the literature. In addition, analytical calculations of spectral positions of WGMs, their expected shifts under certain refractive index differences, and FSR values are analytically calculated and matched with the experimental results very well. Detec-

tion of small particles inside BB oil emulsion droplets and composition of oil emulsion droplets are described in Chapter 6. These oil droplets are prepared easily using oil or oil mixture with manual agitation, and held in place in a microfluidic chip using optical trapping. Different from other studies, Q-factor-based detection is employed in the oil droplet experiments. The Q-factors of WGMs depend on the absorption of the material inside the droplet. Since the absorption of sunflower seed oil is more than olive oil, Q-factors increase linearly as the volume fraction of olive oil increases. In Chapter 7, hydrogen gas sensing is presented using PDMS-urea and Pd-coated OFR. Experimentally, detection of $0.1\% = 1000\ ppm$ hydrogen gas is achieved, with a potential detection capability lower than $0.01\% = 100\ ppm$.

Inspired by these results, certain improvements can be implemented such as employing reference WGM sensors [Kim et al., 2015] or adding temperature stabilization to WGMs [Teraoka, 2014], which will provide better sensitivities and more robustness to the WGM sensors. In addition, different sensing mechanisms can be taken advantage of at the same time to increase the overall sensitivity. For instance, employing coatings that swell under humidity or ethanol will provide such an improvement. For hydrogen sensing, first PDMS-urea and Pd thicknesses can be optimized. Proposed experiments can be completed to understand the underlying sensing mechanism. Then, plasmonic enhancements can also be used in hydrogen sensing applications [Cicek et al., 2017], if feature sizes $\sim 100\ nm$ can be fabricated. Even higher sensitivity can be achieved, if both the effect of hydrogen and the readout signal can be obtained from one single active layer. This method avoids the requirement of additional SU-8 or PDMS-urea layers so that the full effect of the presence of hydrogen gas can be obtained.

Chapter 9

APPENDIX

9.1 Mode Tracking Algorithm Code in Matlab

```
clear all
clc
close all
first_part=sprintf('%s','test01_');
extension=sprintf('%s','_santec.txt');
extension2=sprintf('%s','_notes.txt');
%During the sensing experiments, two txt files are saved in
certain time intervals.  Their names are test01_i_santec.txt
and test01_i_notes.txt
i ranges from 1 to a desired upper limit (here it is 1800)
i_st=1;
i_fin=1800;
width=100;
center=4655;
final_matrix=[];
notes_matrix=[];
hyd_perc=zeros(i_fin+1,1);
%For every measurement, hyd_perc has to be updated properly
hyd_perc(1:10) = 0*ones(length(1:10),1);
hyd_perc(10:800) = 0*ones(length(10:800),1);
hyd_perc(800:900) = 0.003*ones(length(100:200),1);
hyd_perc(900:1000) = 0.005*ones(length(100:200),1);
```

```
hyd_perc(1000:1100) = 0.007*ones(length(100:200),1);
hyd_perc(1100:1200) = 0.01*ones(length(100:200),1);
hyd_perc(1200:1300) = 0.014*ones(length(100:200),1);
hyd_perc(1300:1800) = 0*ones(length(1300:1800),1);
for i=i_st:i_fin;
    a_st=load(sprintf('%s%i%s',first_part,i,extension));
    b_st=load(sprintf('%s%i%s',first_part,i,extension2));
    a=a_st((center-width/2):(center+width/2));
    a=a/max(a);
    x=1:length(a);
    DataInv = 1.01*max(a) - a;
    plot(a_st);
    plot(DataInv,'-o')
    xv=1:length(DataInv);
    xv=xv';
    mu=sum(DataInv.*xv)/sum(DataInv);
    final_indices(i+1)=mu+center-width/2;
    final_matrix=[final_matrix a];
    notes_matrix=[notes_matrix; b_st];
    center=floor(mu)+center-width/2;
    i;
end

final_matrix=final_matrix';
figure(1);
pcolor(final_matrix);
shading flat;
figure(2);
subplot(311)
```

```
plot(linspace(notes_matrix(i_st+1,1),notes_matrix(i_st+1,2),
notes_matrix(i_st+1,3)),a_st);
xlabel('Wavelength (nm)')
ylabel('Intensity (a.u.)')
grid on;
subplot(312)
final_wavelengths=1000*(notes_matrix(i_st+1,2)-
notes_matrix(i_st+1,1))*final_indices((i_st+1):(i_fin+1))
/notes_matrix(i_st+1,3);
final_wavelengths=final_wavelengths-final_wavelengths(1);
initial_v=sum(final_wavelengths(1:5))/5;
final_v=sum(final_wavelengths((length(final_wavelengths)-4):
length(final_wavelengths)))/5;
index_v=linspace(0,length(final_wavelengths)-1,
length(final_wavelengths));
final_wavelengths2=final_wavelengths-(final_v-initial_v)
*index_v /length(final_wavelengths);
x_vector=(notes_matrix(:,5)-notes_matrix(1,5))/60000;
[haxes,hline1,hline2]=plotyy(x_vector,final_wavelengths
,x_vector, hyd_perc(i_st+1:i_fin+1));
ylabel(haxes(2),'H_2 Concentration (%)')
ylabel(haxes(1),'Wavelength Shift (pm)')
xlabel(haxes(2),'Time (mn)')
set(hline1,'Marker','o');
set(hline2,'Color','r','LineWidth',2);
set(haxes,'ycolor','k');
set(haxes(1),'YLim',[-20 75]);
set(haxes(1),'ytick',[-20:10:75]);
set(haxes(2),'YLim',[-2 7.5]);
```

```
set(haxes(2),'ytick',[-2:1:7.5]);
grid(haxes(1),'on');
plot(x_vector,final_wavelengths,'-o')
subplot(313)
plot(x_vector,hyd_perc(i_st+1:i_fin+1));
```

9.2 Analytical Calculation Code for WGMs of OFR in Matlab

```
clc
clear all
close all
format long
nin = 1.46;
nout=1.3183;
%deltan = 0;
%deltan = 0.051498564;
%nout = 1.3183 + deltan;
m = nin/nout; %Relative refractive index
n = 371; %Azimuthal mode number
radius=(125)/2*10^-6
x = linspace (340,420,100000);
% Since x = ka, y = mka, we have
y = m * x;
dalgaboyu = 2*radius*pi*nout./x;
hk=1;
caseI_TE=abs(m.*besselh(n,hk,x).*(besselj(n-1,y)-
besselj(n+1,y))-besselj(n,y).*(besselh(n-1,hk,x)-
besselh(n+1,hk,x)));
semilogy(dalgaboyu,caseI_TE)
```

```
caseII_TM=abs(besselh(n,hk,x).*(besselj(n-1,y)-
besselj(n+1,y))-m.*besselj(n,y).*(besselh(n-1,hk,x)-
besselh(n+1,hk,x)));
hold on;
semilogy(dalgaboyu,caseII_TM, 'r')
hold off;
min_iI=find(caseI_TE==min(caseI_TE));
TE_wl=dalgaboyu(min_iI)
min_iII=find(caseII_TM==min(caseII_TM));
TM_wl=dalgaboyu(min_iII)
```

BIBLIOGRAPHY

[Alam et al., 2013] Alam, M. Z., Carriere, N., Bahrami, F., Mojahedi, M., and Aitchison, J. S. (2013). Pd-based integrated optical hydrogen sensor on a silicon-on-insulator platform. *Optics Letters*, 38:1428–1430.

[Anand et al., 2016] Anand, S., Eryürek, M., Karadag, Y., Erten, A., Serpengüzel, A., Jonáš, A., and Kiraz, A. (2016). Observation of whispering gallery modes in elastic light scattering from microdroplets optically trapped in a microfluidic channel. *Journal of Optical Society of America B*, 33:1349–1354.

[Annamdas, 2011] Annamdas, V. G. M. (2011). Review on developments in fiber optical sensors and applications. *International Journal of Materials Engineering*, 1:1–16.

[Arfken and Weber, 2005] Arfken, G. B. and Weber, H. J. (2005). *Mathematical Methods for Physicists*. Elsevier Academic Press.

[Armani et al., 2007] Armani, A. M., Kulkarni, R. P., Fraser, S. E., Flagan, R. C., and Vahala, K. J. (2007). Label-free, single-molecule detection with optical microcavities. *Science*, 317:783–787.

[Armani and Vahala, 2006] Armani, A. M. and Vahala, K. (2006). Heavy water detection using ultra-high-Q microcavities. *Optics Letters*, 31:1896–1898.

[Armani et al., 2003] Armani, D. K., Kippenberg, T. J., Spillane, S. M., and Vahala, K. J. (2003). Ultra-high-Q toroid microcavity on a chip. *Nature*, 421:925–928.

[Arnold and Folan, 1986] Arnold, S. and Folan, L. M. (1986). Fluorescence spectrom-

eter for a single electrodynamically levitated microparticle. *Review of Scientific Instruments*, 57:2250.

[Arnold and Folan, 1989] Arnold, S. and Folan, L. M. (1989). Energy transfer and the photon lifetime within an aerosol particle. *Optics Letters*, 14:387–389.

[Ashkin and Dziedzic, 1981] Ashkin, A. and Dziedzic, J. M. (1981). Observation of optical resonances of dielectric spheres by light scattering. *Applied Optics*, 20:1803–1814.

[Avino et al., 2014] Avino, S., Krause, A., Zullo, R., Giorgini, A., Malara, P., Natale, P. D., Loock, H. P., and Gagliardi, G. (2014). Direct sensing in liquids using whispering-gallery-mode droplet resonators. *Advanced Optical Materials*, 2:1155–1159.

[Baaske et al., 2014] Baaske, M. D., Foreman, M. R., and Vollmer, F. (2014). Single-molecule nucleic acid interactions monitored on a label-free microcavity biosensor platform. *Nature Nanotechnology*, 9:933–939.

[Bae et al., 2013] Bae, M.-K., Lim, J. A., Kim, S., and Song, Y.-W. (2013). Ultra-highly sensitive optical gas sensors based on chemomechanical polymer-incorporated fiber interferometer. *Optics Express*, 21:181022.

[Bellini et al., 2007] Bellini, B., d'Alessandro, A., and Beccherelli, R. (2007). A method for butt-coupling optical fibres to liquid crystal planar waveguides. *Optical Materials*, 29:1019–1022.

[Benner et al., 1980] Benner, R. E., Barber, P. W., Owen, J. F., and Chang, R. K. (1980). Observation of structure resonances in the fluorescence spectra from microspheres. *Physical Review Letters*, 44:475–478.

[Bévenot et al., 2000] Bévenot, X., Trouillet, A., Veillas, C., Gagnaire, H., and Clément, M. (2000). Hydrogen leak detection using an optical fiber sensor for aerospace applications. *Sensors and Actuators B*, 67:57–67.

[Bhardwaj et al., 2016] Bhardwaj, V., Gangwar, R. K., and Singh, V. K. (2016). Silicone rubber-coated highly sensitive optical fiber sensor for temperature measurement. *Optical Engineering*, 55:126107.

[Bhola et al., 2009] Bhola, B., Nosovitskiy, P., Mahalingam, H., and Steier, W. H. (2009). Sol-gel-based integrated optical microring resonator humidity sensor. *IEEE Sensors*, 9:740–747.

[Bhola et al., 2005] Bhola, B., Song, H.-C., Tazawa, H., and Steier, W. H. (2005). Polymer microresonator strain sensors. *IEEE Photonics Technology Letters*, 17(4):867–869.

[Bian et al., 2018] Bian, C., Hu, M., nad T. Gang, R. W., Tong, R., Zhang, L., Guo, T., Liu, X., and Qiao, X. (2018). Optical fiber humidity sensor based on the direct response of the polyimide film. *Applied Optics*, 57:356–361.

[Bogue, 2011] Bogue, R. (2011). Fibre optic sensors: a review of today's applications. *Sensors Review*, 31:304–309.

[Bohren and Huffman, 1998] Bohren, C. F. and Huffman, D. R. (1998). *Absorption and Scattering of Light by Small Particles*. Wiley-VCH.

[Boleininger et al., 2010] Boleininger, A., Lake, T., Hami, S., and Vallance, C. (2010). Whispering gallery modes in standard optical fibres for fibre profiling measurements and sensing of unlabelled chemical species. *Sensors*, 10(3):1765.

[Cai et al., 2000] Cai, M., Painter, O., and Vahala, K. J. (2000). Observation of critical coupling in a fiber taper to a silica-microsphere whispering-gallery mode system. *Physical Review Letters*, 85:74–77.

[Chen et al., 1993] Chen, G., Chowdhury, D. Q., and Chang, R. K. (1993). Laser-induced radiation leakage from microdroplets. *Journal of Optical Society of America B*, 10:620–632.

[Chen and Lu, 2005] Chen, Z. and Lu, C. (2005). Humidity sensors: A review of materials and mechanisms. *Sensors Letters*, 23:274–295.

[Chiuchiolo et al., 2017] Chiuchiolo, A., Bajas, H., Bajko, M., Castaldo, B., Consales, M., Cusano, A., Giordano, M., Giloux, C., Perez, J. C., Sansone, L., and Viret, P. (2017). Cryogenic test facility instrumentation with fiber optic and fiber optic sensors for testing superconducting accelerator magnets. *IOP Conference Series: Materials Science and Engineering*, 278:012082.

[Cho and Jokerst, 2006] Cho, S.-Y. and Jokerst, N. M. (2006). A polymer microdisk photonic sensor integrated onto silicon. *IEEE Photonics Technology Letters*, 18:2096–2098.

[Chýlek et al., 1978] Chýlek, P., Kiehl, J. T., and Ko, M. K. W. (1978). Optical levitation and partial-wave resonances. *Physical Review A*, 18:2229–2233.

[Cicek et al., 2017] Cicek, K., Eryürek, M., and Kiraz, A. (2017). Single-slot hybrid microring resonator hydrogen sensor. *Journal of Optical Society of America B*, 34:1465–1470.

[Dantham et al., 2012] Dantham, V. R., Holler, S., Kolchenko, V., Wan, Z., and Arnold, S. (2012). Taking whispering gallery-mode single virus detection and sizing to the limit. *Applied Physics Letters*, 101:043704.

[Dinçer, 2002] Dinçer, I. (2002). Technical, environmental and exergetic aspects of hydrogen systems. *International Journal of Hydrogen Energy*, 27:265–285.

[Ding et al., 2010] Ding, L., Belacel, C., Ducci, S., Leo, G., and Favero, I. (2010). Ultralow loss single-mode silica tapers manufactured by a microheater. *Applied Optics*, 49:2441–2445.

[Dong et al., 2009] Dong, C.-H., He, L., Xiao, Y.-F., Gaddam, V. R., Ozdemir, S. K., Han, Z. F., Guo, G.-C., and Yang, L. (2009). Fabrication of high-Q polydimethylsiloxane optical microspheres for thermal sensing. *Applied Physics Letters*, 94:231119.

[Eryürek, 2013] Eryürek, M. (2013). Hydrogen gas sensor based on a polymer optical microdisk resonator. Master's thesis, Koç University.

[Eryürek et al., 2017a] Eryürek, M., Karadag, Y., Ghafoor, M., Bavili, N., Cicek, K., and Kiraz, A. (2017a). Liquid refractometric sensors based on optical fiber resonators. *Sensors and Actuators A: Physical*, 265:161–167.

[Eryürek et al., 2015] Eryürek, M., Karadag, Y., Taşaltın, N., Kılınç, N., and Kiraz, A. (2015). Optical sensor for hydrogen gas based on a palladium-coated polymer microresonator. *Sensors and Actuators B: Chemical*, 212:78–83.

[Eryürek et al., 2017b] Eryürek, M., Tasdemir, Z., Karadag, Y., Anand, S., Kılınç, N., Alaca, B., and Kiraz, A. (2017b). Integrated humidity sensor based on SU-8 polymer microdisk microresonator. *Sensors and Actuators B: Chemical*, 242:1115–1120.

[Fan et al., 2008] Fan, X., White, I. M., Shopova, S. I., Zhu, H., Suter, J. D., and Sun, Y. (2008). Sensitive optical biosensors for unlabeled targets: A review. *Analytica Chimica Acta*, 620:8–26.

[Farahani et al., 2014] Farahani, H., Wagiran, R., and Hamidon, M. N. (2014). Humidity sensors principle, mechanism, and fabrication technologies: A comprehensive review. *Sensors*, 14:7881–7939.

[Fogg et al., 1955] Fogg, E., Hixson, A., and Thompson, A. (1955). Densities and refractive indexes for ethylene glycol–water solutions. *Anal. Chem.*, 27:1609–1611.

[Foreman et al., 2015] Foreman, M. R., Swaim, J. D., and Vollmer, F. (2015). Whispering gallery mode sensors. *Advances in Optics and Photonics*, 7:168–240.

[Gardner et al., 2017] Gardner, K., Zhi, Y., Tan, L., Lane, S., Xiao, Y.-F., and Meldrum, A. (2017). Whispering gallery mode structure in polymer-coated lasing microspheres. *Journal of Optical Society of America B*, 34:2140–2146.

[Gilardi et al., 2009] Gilardi, G., Donisi, D., Serpengüzel, A., and Becherelli, R. (2009). Liquid-crystal tunable filter based on sapphire microspheres. *Optics Letters*, 34:3253–3255.

[González-Sierra et al., 2017] González-Sierra, N. E., del Carmen Gómez-Pavón, L., Pérez-Sánchez, G. F., Luis-Ramos, A., Zaca-Morán, P., and Chávez-Ramírez, J. M. M.-P. F. (2017). Tapered optical fiber functionalized with palladium nanoparticles by drop casting and laser radiation for H_2 and volatile organic compounds sensing purposes. *Sensors*, 17:2039.

[Griffin et al., 2013] Griffin, B. G., Arbabi, A., and Goddard, L. L. (2013). Engineering the sensitivity and response time of edge-emitting laser hydrogen sensors. *IEEE Sensors Journal*, 13(8):3098–3105.

[Griffin et al., 2012] Griffin, B. G., Arbabi, A., Kasten, A. M., Choquette, K. D., and Goddard, L. L. (2012). Hydrogen detection using a functionalized photonic crystal vertical cavity laser. *IEEE Journal of Quantum Electronics*, 48(2):160–168.

[Hanumegowda et al., 2005] Hanumegowda, N. M., Stica, C. J., Patel, B. C., White, I., and Fan, X. (2005). Refractometric sensors based on microsphere resonators. *Applied Physics Letters*, 87(20):201107.

[Harker et al., 2013] Harker, A., Mehrabani, S., and Armani, A. M. (2013). Ultraviolet light detection using an optical microcavity. *Optics Letters*, 38:3422–3425.

[Hübert et al., 2011] Hübert, T., Boon-Brett, L., Black, G., and Banach, U. (2011). Hydrogen sensors – a review. *Sensors and Actuators B*, 157:329–352.

[He et al., 2013] He, L., Özdemir Ş. K., and Yang, L. (2013). Whispering gallery microcavity lasers. *Laser Photonics Reviews*, 7:60–82.

[He et al., 2011] He, L., Özdemir Ş. K., Zhu, J., Kim, W., and Yang, L. (2011). Detecting single viruses and nanoparticles using whispering gallery microlasers. *Nature Nanotechnology*, 6:428–432.

[Horváth et al., 2017] Horváth, B., Ormos, P., and Kelemen, L. (2017). Nearly aberration-free multiphoton polymerization into thick photoresist layers. *Micromachines*, 8:1–9.

[Hossein-Zadeh and Vahala, 2006] Hossein-Zadeh, M. and Vahala, K. J. (2006). Fiber-taper coupling to whispering-gallery modes of fluidic resonators embedded in a liquid medium. *Opt. Express*, 14:10800–10810.

[Huang et al., 2017] Huang, Q.-L., Xu, H.-L., Li, M.-T., Hou, Z.-S., Lv, C., Z., X.-P., Li, H.-L., Xia, H., Wang, H.-Y., and Sun, H.-B. (2017). Stretchable PEG-DA hydrogel-based whispering-gallery-mode microlaser with humidity responsiveness. *Journal of Lightwave Technology*, 36:819 – 824.

[Hunt et al., 2010] Hunt, H. K., Soteropulos, C., and Armani, A. M. (2010). Bioconjugation strategies for microtoroidal optical resonators. *Sensors*, 10:9317–9336.

[Ilchenko and Matsko, 2006] Ilchenko, V. S. and Matsko, A. B. (2006). Optical resonators with whispering-gallery modes-part ii: Applications. *IEEE Journal of Selected Topics in Quantum Electronics*, 12:15.

[International Telecommunication Union, 2018] International Telecommunication Union, I. (2018). Itu telecommunication standardization sector <https://www.itu.int/en/itu-t/pages/default.aspx>.

[Ioppolo et al., 2010] Ioppolo, T., Das, N., and Ötügen, M. V. (2010). Whispering gallery modes of microspheres in the presence of a changing surrounding medium: A new ray-tracing analysis and sensor experiment. *Journal of Applied Physics*, 107(10):103105.

[Ioppolo et al., 2008] Ioppolo, T., Kozhevnikov, M., Stepaniuk, V., Ötügen, M. V., and Sheverev, V. (2008). Micro-optical force sensor concept based on whispering gallery mode resonators. *Applied Optics*, 47:3009–3014.

[Jiang et al., 2016] Jiang, X.-F., Zou, C.-L., Wang, L., Gong, Q., and Xiao, Y.-F. (2016). Whispering-gallery microcavities with unidirectional laser emission. *Laser Photonics Reviews*, 10:40–61.

[Jin and Granville, 2016] Jin, Y. and Granville, A. M. (2016). Polymer fiber optic sensors – a mini review of their synthesis and applications. *Journal of Biosensors & Bioelectronics*, 7:1000194.

[Jonáš et al., 2012] Jonáš, A., Karadag, Y., Mestre, M., and Kiraz, A. (2012). Probing of ultrahigh optical Q-factors of individual liquid microdroplets on superhydrophobic surfaces using tapered optical fiber waveguides. *Journal of Optical Society of America B*, 29(12):3240–3247.

[Kavungal et al., 2018] Kavungal, V., Farrell, G., Wu, Q., Mallik, A. K., and Semenova, Y. (2018). Studies of geometrical profiling in fabricated tapered optical fibers using whispering gallery modes spectroscopy. *Optical Fiber Technology*, 41:82–88.

[Kenny et al., 1991] Kenny, R. P., Birks, T. A., and Oakley, K. P. (1991). Control of optical fibre shape. *Electronics Letters*, 27:1654–1656.

[Kim et al., 2015] Kim, D., Popescu, P., Harfouche, M., Sendowski, J., Maria-Eleni, Dimotsantou, Flagan, R. C., and Yariv, A. (2015). On-chip integrated differential optical microring refractive index sensing platform based on a laminar flow scheme. *Optics Letters*, 40:4106–4109.

[Kim et al., 2017] Kim, H.-G., Park, J.-M., Ryu, J.-H., Kim, S.-B., Kim, C.-M., Choi, Y.-W., and Oh, K.-R. (2017). Optical biochemical sensor based on half-circled microdisk laser diode. *Optics Express*, 25:24939.

[Kiraz et al., 2006] Kiraz, A., Kurt, A., Dündar, M. A., and Demirel, A. L. (2006). Simple largely tunable optical microcavity. *Applied Physics Letters*, 89:081118.

[Kolpakov et al., 2014] Kolpakov, T. A., Gordon, N. T., Mou, C., and Zhou, K. (2014). Toward a new generation of photonic humidity sensors. *Sensors*, 14:3986–4013.

[Ksendzov et al., 2004] Ksendzov, A., Homer, M., and Manfreda, A. (2004). Integrated optics ring- resonator chemical sensor with polymer transduction layer. *Electronics Letters*, 40:63–65.

[Lambert et al., 2011] Lambert, E., Fiers, M., Nizamov, S., Tassaert, M., Johnson, S. G., Bientsman, P., and Bogaerts, W. (2011). Python bindings for the open source electromagnetic simulator meep. *Computing in Science & Engineering*, 13:53–63.

[Lee, 2003] Lee, B. (2003). Review of the present status of optical fiber sensors. *Optical Fiber Technology*, 9:57–79.

[Lee et al., 2009] Lee, B., Roh, S., and Park, J. (2009). Current status of micro- and nano-structured optical fiber sensors. *Optical Fiber Technology*, 15:209–221.

[Lee and Lee, 2005] Lee, C.-Y. and Lee, G.-B. (2005). Humidity sensors: A review. *Sensors Letters*, 3:1–14.

[Leung et al., 2007] Leung, A., Shankar, P. M., and Mutharasan, R. (2007). A review of fiber-optic biosensors. *Sensors and Actuators B: Chemical*, 125:688–703.

[Leung et al., 2015] Leung, C. K. Y., Wan, K. T., Inaudi, D., Bao, X., Habel, W., Zhou, Z., Ou, J., Ghandehari, M., Wu, H. C., and Imai, M. (2015). Review: optical fiber sensors for civil engineering applications. *Materials and Structures*, 48:871–906.

[Levy et al., 2006] Levy, U., Campbell, K., Groisman, A., Mookherjea, S., and Fainman, Y. (2006). On-chip microfluidic tuning of an optical microring resonator. *Applied Physics Letters*, 88:111107.

[Li et al., 2014] Li, B.-B., Clements, W. R., Yu, X.-C., Shia, K., Gonga, Q., and Xiao, Y.-F. (2014). Single nanoparticle detection using split-mode microcavity raman lasers. *Proceedings of the National Academy of Sciences*, 111:14657–14662.

[Li et al., 2010] Li, B.-B., Wang, Q.-Y., Xiao, Y.-F., Jiang, X.-F., Li, Y., Xiao, L., and Gong, Q. (2010). On chip, high-sensitivity thermal sensor based on high-Q polydimethylsiloxane-coated microresonator. *Applied Physics Letters*, 96:251109.

[Li and Fan, 2010] Li, H. and Fan, X. (2010). Characterization of sensing capability of optofluidic ring resonator biosensors. *Applied Physics Letters*, 97:011105.

[Lide, 2012] Lide, D. R. (2012). *CRC Handbook of Chemistry and Physics, Internet Version 2012, <http://www.hbcpnetbase.com>*. CRC Press.

[Liou and Tseng, 2009] Liou, J.-C. and Tseng, F.-G. (2009). Tunable coupled-ring-resonator of thermally actuated optical switch array. *Journal of Modern Optics*, 56(16):1747–1760.

[Lv et al., 2015] Lv, J., Cheng, Y., Yuan, W., Hao, X., and Chen, F. (2015). Three-dimensional femtosecond laser fabrication of waveguide beam splitters in $LiNbO_3$ crystal. *Optical Materials Express*, 5:1274–1280.

[Ma et al., 2010] Ma, Q., Huang, L., Guo, Z., and Rossmann, T. (2010). Spectral shift response of optical whispering-gallery modes due to water vapor adsorption and desorption. *Measurement Science and Technology*, 21:115206.

[Manzo and Ioppolo, 2015] Manzo, M. and Ioppolo, T. (2015). Untethered photonic sensor for wall pressure measurement. *Optics Letters*, 40(10):2257–2260.

[Manzo et al., 2007] Manzo, M., Ioppolo, T., Ayaz, U. K., LaPenna, V., and Ötügen, M. V. (2007). A photonic wall pressure sensor for fluid mechanics applications. *Journal of Optical Society of America B*, 24(10):2721–2726.

[Mata et al., 2006] Mata, A., Fleischman, A. J., and Roy, S. (2006). Fabrication of multi-layer SU-8 microstructures. *Journal of Micromechanics and Microengineering*, 16(2):276.

[Matsko et al., 2015] Matsko, A. B., Savchenkov, A. A., Strekalov, D., Ilchenko, V. S., and Maleki, L. (2015). Review of applications of whispering-gallery mode resonators in photonics and nonlinear optics. *Advances in Optics and Photonics*, 7:168–240.

[MEEP, 2017] MEEP (2017). Meep <https://meep.readthedocs.io/en/latest/>.

[Mehrabani et al., 2013] Mehrabani, S., Kwong, P., Gupta, M., and Armani, A. M. (2013). Hybrid microcavity humidity sensor. *Applied Physics Letters*, 102:241101.

[Michler et al., 2001] Michler, P., Kiraz, A., Becher, C., Zhang, L., Hu, E., Imamoglu, A., Schoenfeld, W. V., and Petroff, P. M. (2001). Quantum dot lasers using high-Q microdisk cavities. *Physica Status Solidi (b)*, 224:797–801.

[MicroChem, 2018] MicroChem (2018). Su-8 2000 permanent epoxy resists <http://www.microchem.com/prod-su82000.htm>.

[Noh et al., 2011] Noh, J.-S., Lee, J. M., and Lee, W. (2011). Low-dimensional palladium nanostructures for fast and reliable hydrogen gas detection. *Sensors*, 11:825–851.

[Ong et al., 2006] Ong, B. H., Yuan, X., Tao, S., and Tjin, S. C. (2006). Photothermally enabled lithography for refractive-index modulation in SU-8 photoresist. *Optics Letters*, 31(10):1367–1369.

[Orghici et al., 2010] Orghici, R., Lützow, P., Burgmeier, J., Koch, J., Heidrich, H., Schade, W., Welchsoff, N., and Waldvogel, S. (2010). A microring resonator sensor for sensitive detection of 1,3,5-trinitrotoluene (*tnt*). *Sensors*, 10:6788–6795.

[Polyanskiy, 2008] Polyanskiy, M. (2008). Refractive index database <https://refractiveindex.info>.

[Ramakrishnan et al., 2016] Ramakrishnan, M., Rajan, G., Semenova, Y., and Farrell, G. (2016). Overview of fiber optic sensor technologies for strain/temperature sensing applications in composite materials. *Sensors*, 16:99.

[Ramanujan, 1927] Ramanujan, S. (1927). *Collected papers of Srinivasa Ramanujan.* Cambridge University Press.

[Righini et al., 2011] Righini, G. C., Dumeige, Y., Feron, P., Ferrari, M., Conti, G. N., Ristic, D., and Soria, S. (2011). Whispering gallery mode microresonators: Fundamentals and applications. *Rivista Del Nuovo Cimento*, 34:435–488.

[Rittersma, 2002] Rittersma, Z. M. (2002). Recent achievements in miniaturised humidity sensors - a review of transduction techniques. *Sensors and Actuators A: Physical*, 96:196–210.

[Sami et al., 2014] Sami, S., Yildirim, E., Yurtsever, M., Yurtsever, E., Yilgor, E., Yilgor, I., and Wilkes, G. L. (2014). Understanding the influence of hydrogen bonding and diisocyanate symmetry on the morphology and properties of segmented

polyurethanes and polyureas: Computational and experimental study. *Polymer*, 55:4563–4576.

[Sato et al., 2011] Sato, S., Ose, T., Miyata, S., Kanehashi, S., Ito, H., Matsumoto, S., Iwai, Y., Matsumoto, H., and Nagai, K. (2011). Relationship between the gas transport properties and the refractive index in high-free-volume fluorine-containing polyimide membranes. *Journal of Applied Polymer Science*, 121:2794–2803.

[Schenato, 2017] Schenato, L. (2017). A review of distributed fibre optic sensors for geo-hydrological applications. *Applied Sciences*, 7:896.

[Schmid et al., 2009] Schmid, S., Kühne, S., and Hierold, C. (2009). Influence of air humidity on polymeric microresonators. *Journal of Micromechanics and Microengineering*, 19:1–9.

[Serpengüzel et al., 1995] Serpengüzel, A., Arnold, S., and Griffel, G. (1995). Excitation of resonances of microspheres on an optical fiber. *Optics Letters*, 20:654–656.

[Serpengüzel et al., 1997] Serpengüzel, A., Arnold, S., Griffel, G., and Lock, J. A. (1997). Enhanced coupling to microsphere resonances with optical fibers. *Journal of Optical Society of America B*, 14:790–795.

[Serpengüzel et al., 1992] Serpengüzel, A., Chen, G., and Chang, R. K. (1992). Heuristic model for the growth and coupling of nonlinear processes in droplets. *Journal of Optical Society of America B*, 9:871–883.

[Shao et al., 2017] Shao, J.-X., Xie, W.-G., Song, X., and Zhang, Y.-N. (2017). A new hydrogen sensor based on sns fiber interferometer with Pd/WO_3 coating. *Sensors*, 17:2144.

[Shao et al., 2013] Shao, L., Jiang, X.-F., Yu, X.-C., Li, B.-B., Clements, W. R., Vollmer, F., Wang, W., Xiao, Y.-F., and Gong, Q. (2013). Detection of single

nanoparticles and lentiviruses using microcavity resonance broadening. *Advanced Materials*, 25:5616.

[Socorro et al., 2015] Socorro, A. B., Soltani, S., Villar, I. D., Corres, J. M., and Armani, A. M. (2015). Temperature sensor based on a hybrid ITO silica resonant cavity. *Optics Express*, 23:1930–1937.

[Spillane et al., 2003] Spillane, S. M., Kippenberg, T. J., Painter, O. J., and Vahala, K. J. (2003). Ideality in a fiber-taper-coupled microresonator system for application to cavity quantum electrodynamics. *Physical Review Letters*, 91:043902.

[Strutt, 1910] Strutt, J. W. (1910). The problem of the whispering gallery. *Philosophical Magazine*, 20(120):1001–1004.

[Sun and Fan, 2011] Sun, Y. and Fan, X. (2011). Optical ring resonators for biochemical and chemical sensing. *Analytical and Bioanalytical Chemistry*, 399:205–211.

[Ta et al., 2013] Ta, V. D., Chen, R., Nguyen, D. M., and Sun, H. D. (2013). Application of self- assembled hemispherical microlasers as gas sensors. *Applied Physics Letters*, 102:031107.

[Teraoka, 2014] Teraoka, I. (2014). Analysis of thermal stabilization of whispering gallery mode resonance. *Optics Communications*, 310:212–216.

[Thorlabs, 1999] Thorlabs (1999). Spec sheet for smf-28-100 fiber <https://www.thorlabs.com/thorproduct.cfm?partnumber=smf-28-100>.

[Tripathy et al., 2014] Tripathy, A., Pramanik, S., Cho, J., Santosh, J., and Osman, N. A. A. (2014). Role of morphological structure, doping, and coating of different materials in the sensing characteristics of humidity sensors. *Sensors*, 14:16343–16422.

[Udd, 1995] Udd, E. (1995). An overview of fiber-optic sensors. *Review of Scientific Instruments*, 66:4015–4030.

[Vahala, 2003] Vahala, K. J. (2003). Optical microcavities. *Nature*, 424:839.

[van de Hulst, 1981] van de Hulst, H. C. (1981). *Light Scattering by Small Particles*. Dover Publications Inc., 2nd edition.

[Velasco-Garcia, 2009] Velasco-Garcia, M. N. (2009). Optical biosensors for probing at the cellular level: A review of recent progress and future prospects. *Seminars in Cell & Developmental Biology*, 20:27–33.

[Villatoro et al., 2003] Villatoro, J., Monzon-Hernandez, D., and Mejia, E. (2003). Fabrication and modeling of uniform-waist single-mode tapered optical fiber sensors. *Applied Optics*, 42:2278–2283.

[Vollmer et al., 2002] Vollmer, F., Braun, D., Libchaber, A., Khoshsima, M., Teraoka, I., and Arnold, S. (2002). Protein detection by optical shift of resonant microcavity. *Applied Physics Letters*, 80:4057.

[Wang et al., 2014] Wang, J., Zhan, T., Huang, G., Chu, P. K., and Mei, Y. (2014). Optical microcavities with tubular geometry: properties and applications. *Laser Photonics Reviews*, 8:521–547.

[White et al., 2006] White, I. M., Oveys, H., and Fan, X. (2006). Liquid-core optical ring-resonator sensors. *Optics Letters*, 31:1319–1321.

[Wu et al., 2009] Wu, Y., Zeng, X., Rao, Y.-J., Gong, Y., Hou, C.-L., and Yang, G.-G. (2009). MOEMS accelerometer based on microfiber knot resonator. *IEEE Photonics Technology Letters*, 21:1547–1549.

[Wu et al., 2011] Wu, Y., Zhang, T., Rao, Y., and Gong, Y. (2011). Miniature interferometric humidity sensors based on silica/polymer microfiber knot resonators. *Sensors and Actuators B: Chemcial*, 155:258–263.

[Yebo et al., 2010] Yebo, N. A., Lommens, P., Hens, Z., and Baets, R. (2010). An integrated optic ethanol vapor sensor based on a silicon-on-insulator microring resonator coated with a porous ZnO film. *Optics Express*, 18:11859–11866.

[Yebo et al., 2012] Yebo, N. A., Sree, S. P., Levrau, E., Detavernier, C., Hens, Z., Martens, J. A., and Baets, R. (2012). Selective and reversible ammonia gas detection with nanoporous film functionalized silicon photonic micro-ring resonator. *Optics Express*, 20:11855–11862.

[Yebo et al., 2009] Yebo, N. A., Taillaert, D., Roels, J., Lahem, D., Debliquy, M., Thourhout, D. V., and Baets, R. (2009). Silicon-on-insulator (SOI) ring resonator-based integrated optical hydrogen sensor. *IEEE Photonics Technology Letters*, 21(14):960–962.

[Yilgor et al., 1984] Yilgor, I., Sha'aban, A. K., Jr., W. P. S., Tyagi, D., Wilkes, G. L., and McGrath, J. E. (1984). Segmented organosiloxane copolymers. i. synthesis of siloxane-urea copolymers. *Polymer*, 25:1800–1806.

[Yoshue et al., 2011] Yoshue, T., Tang, L., and Su, S.-Y. (2011). Optical microcavity: sensing down to single molecules and atoms. *Sensors*, 11:1972–1991.

[Zhang et al., 2014] Zhang, J., Zhong, J., Fang, Y. F., Wang, J., Huang, G. S., Cui, X. G., and Mei, Y. F. (2014). Roll up polymer/oxide/polymer nanomembranes as a hybrid optical microcavity for humidity sensing. *Nanoscale*, 6:13646–13650.

[Zhang et al., 2017] Zhang, Y., Peng, H., Qian, X., Zhang, Y.-N., An, G., and Zhao, Y. (2017). Recent advancements in optical fiber hydrogen sensors. *Sensors and Actuators B: Chemical*, 244:393–416.

[Zhi et al., 2013] Zhi, Y., Thiessen, T., and Meldrum, A. (2013). Silicon quantum dot coated microspheres for microfluidic refractive index sensing. *Journal of Optical Society of America B*, 30:51–56.

[Zhi et al., 2017] Zhi, Y., Yu, X.-C., Gong, Q., Yang, L., and Xiao, Y.-F. (2017). Single nanoparticle detection using optical microcavities. *Advanced Materials*, 29:1604920–1604938.

Chapter 10

VITA

Mustafa Eryürek was born in Razgrad, Bulgaria in 1987. He graduated from Bilkent University, Department of Physics in 2010. Then he joined to Koç University, Optoelectronics and Photonics Engineering for his MS degree. In 2013, he defended his MS thesis titled as *Hydrogen Gas Sensor Based on a Polymer Optical Microdisk Resonator*. He continued his studies in his PhD in Koç University, Department of Physics, and finished in 2018. The title of his thesis is *Optofluidic Sensing with Optical Microresonators*.

10.1 List of Publications

1. M. Eryürek, Y. Karadag, N. Taşaltın, N. Kılınç, and A. Kiraz. *Optical Sensor for Hydrogen Gas Based on a Palladium-Coated Polymer Microresonator*. Sensors and Actuators B: Chemical, 212: 78-83 (2015).

2. S. Anand, M. Eryürek, Y. Karadağ, A. Erten, A. Serpengüzel, A. Jonáš, and A. Kiraz. *Observation of Whispering Gallery Modes in Elastic Light Scattering from Microdroplets Optically Trapped in a Microfluidic Channel*. Journal of Optical Society of America B, 33 (7): 1349-1354 (2016).

3. A. Mustafa, A. Erten, R. A. Ayaz, O. Kayıllığlu, A. Eser, M. Eryürek, M. Irfan, M. Muradoglu, M. Tanyeri, and A. Kiraz. *Enhanced Dissolution of Liquid Microdroplets in the Extensional Creeping Flow of a Hydrodynamic Trap*. Langmuir, 32 (37): 9460–9467 (2016).

4. M. Eryürek, Z. Tasdemir, Y. Karadag, S. Anand. N. Kılınç, B. E. Alaca, and A. Kiraz. *Integrated Humidity Sensor Based on SU-8 Polymer Microdisk Microresonator*. Sensors and Actuators B: Chemical, 242: 1115-1120 (2017).

5. K. Cicek, M. Eryürek, and A. Kiraz. *Single-Slot Hybrid Microring Resonator Hydrogen Sensor.* Journal of Optical Society of America B, 34 (7): 1465-1470 (2017).

6. M. Eryürek, Y. Karadag, M. Ghafoor, N. Bavili, K. Cicek, and A. Kiraz. *Liquid Refractometric Sensors Based on Optical Fiber Resonators.* Sensors and Actuators A: Physical, 265: 161-167 (2017).